Nanoscale experimental and numerical investigations of novel photonic devices

Mark Schiller

A dissertation

submitted to the Faculty of

the Department of Physics

in partial fulfillment

of the requirements

for the degree of

Doctor of Philosophy

Boston College

Morrissey College of Arts and Sciences

Graduate School

May 2024

Nanoscale experimental and numerical investigations of novel photonic devices

Mark Schiller

Advisor: Michael J. Naughton, Ph.D.

Abstract

For many centuries, physicists and engineers have explored the creation, manipulation and detection of light. Only within the past century, however, have fabrication techniques advanced to the point where individual photons can be generated, manipulated, and measured. These advances have brought us to the point we are at today, where photonic devices are set to revolutionize the fields of computing, sensing and quantum information, to name a few. Despite the promise of these devices, scientists are still working to fully understand the light-matter interactions that govern their behavior. In this thesis, we uniquely characterize the behavior of certain photonic devices in an effort to understand the underlying physical principles that define them. Of particular interest to us is imaging via near-field scanning optical microscopy (NSOM) of photonic integrated circuit (PIC) elements with high quality factors (Q), such as microring resonators and photonic crystal cavities (PhCs). While these elements are becoming ubiquitous in emerging PIC designs, they have remained difficult to accurately image due to their high sensitivity to small perturbations (i.e. the NSOM probe). We solve this problem by controllably modulating the NSOM tip-sample distance and reducing the size of the probe. Finite element model computer simulations demonstrate that both of these adjustments decrease the

tip sample interaction. We then apply this knowledge to generate first of their kind 50 nm resolution NSOM images of high Q resonant PIC devices. Importantly, aside from being accurate, the proposed NSOM technique is also facile and non-destructive. In addition to local field exploration of PIC elements, we explore non-classical optical transmission through sub-wavelength apertures in metallic films. We demonstrate that these interesting features arise from photonic wave interference.

TABLE OF CONTENTS

LIST OF FIGURES

LIST OF TABLES

<u>Table</u>

LIST OF ABBREVIATIONS

1D One-dimensional

2D Two-dimensional

3D Three-dimensional

AFM Atomic force microscopy

BOE Buffered oxide etch

BOX Buried oxide

C-Band Conventional-band

CMOS Complementary metal-oxide-semiconductor

cNSOM Collection-based near-field scanning optical microscopy

dB Decibel

dBm Decibel-milliwatts

DWDM Dense wavelength-division multiplexing

EBL Electron beam lithography

EOT Extraordinary optical transmission

FDFD Finite-difference frequency-domain

FDTD Finite-difference time-domain

FEM Finite element method

FIB Focused ion beam

FSR Free spectral range

fwhm Full width at half maximum

GC Grating coupler

I/O Input/output

NA Numerical aperture

NIR Near-infrared

NM Normal mode

NSOM Near-field scanning optical microscopy

O-Band Original-band

PEC Perfect electric conductor

PDE Partial differential equation

PhC Photonic crystal

PhCnB Photonic crystal nanobeam cavity

PIC Photonic integrated circuit

PMC Perfect magnetic conductor

Q Quality factor

QNM Quasi-normal mode

$\mathbf{r_e}$ Extinction ratio

RF Radio frequency

SEM Scanning electron microscopy

sNSOM Scattering-type near-field scanning optical microscopy

SPM Scanning probe microscopy

_T_ Transmission

TE Transverse electric

TM Transverse magnetic

traNSOM Transmission-based near-field scanning optical microscopy

_V_ Mode volume

ACKNOWLEDGEMENTS

The following thesis and work is dedicated to my wonderful wife Lucinda
Schiller.

Writing and defending a thesis is a massive undertaking. Despite their only being
one name on the cover page, dozens of people have contributed large amounts
of time, effort, and support to make this thesis a reality. First and foremost, I
would like to thank my wife Lucy, who has gone above and beyond to be an
incredibly supportive, helpful and inspiring wife and mother while still excelling
with her own impressive work. Completing this thesis would certainly not have
been possible without the almighty effort that she contributed and I am forever
grateful.

I would also like to thank my parents (Philip Schiller and Kim Gassett-Schiller),
brother (Erik Schiller), parents in-law (David and Stephanie Knott) and brother in-
law (Henry Knott). Completing and writing a thesis can be a lonely and, at times,
demoralizing process. My family would always manage to pick me up during my
lowest points and re-inspire me to continue on the path toward a Ph.D.

I would next like to thank my advisor and thesis committee chair Professor
Michael J. Naughton. Thank you for giving me the opportunity to work in your

Chapter I

Introduction

1.1 Photonics

The question of whether light is a wave or a particle has divided the

physics community for over two centuries. Two of the early galvanizing figures

were Huygen and Newton, with the former writing, Traité de la lumière [1]

(published in 1690). Huygens described the birefringence caused by an Iceland

Crystal with a geometric description of light as a wavefront that propagates

through a medium known as ether, similar to how sound propagates as a

wavefront through air. On the other side of the argument, Newton published

Opticks [2] in 1704, where he took the view that light sources emit particles

known as corpuscles and that these particles are perfectly elastic, weightless

and rigid. Despite many experiments, such as Einsteins's demonstration of the

photoelectric effect [3], the idea that light is a quantized packet of energy wasn't

widely accepted until Compton scattered photons off of electrons, decreasing

their energy, and increasing their wavelength [4]. However, despite the wave and

particle natures of light both being widely accepted after Compton's experiment,

it was de Broglie who finally (exactly 100 years before this thesis was written)

merged the wave-particle contradiction into a unifying idea [5]. At this point, the

concept of light as *both* a wave *and* a particle was born.

The sub-field of photonics is based on the idea that light consists of

individual countable particles known as photons. Classical optics, on the other

hand, relies more on the group properties of light. Classical optical experiments

are inherently macro-scale, with components like mirrors, beamsplitters and lenses manipulating the light. Photonic experiments rely on incredibly accurate generation and detection of photons, as well as precision nano and micro fabrication. Because of this, photonics is inherently linked to the advances in micro and nano device fabrication. Constant evolutions in technologies such as photolithography, electron beam lithography (EBL), focused ion beam (FIB) milling, etc. have not only allowed researchers to push the limits of photonics devices, but also allowed major foundries to mass produce complex and highly efficient photonic integrated circuits (PICs). With these advances in fabrication, new understanding of nano and micro-scale physics has emerged.

1.2 Subwavelength apertures

Of specific interest over the past centuries has been the behavior and transmission of light through subwavelength apertures. In 1665, the Italian Jesuit Priest Francesco Maria Grimaldi became the first physicist to use the term "diffraction", when referring to the behavior of sunlight passing through a circular aperture [6]. He noticed that the light could not be following a rectilinear path, rather, once light passed through the aperture, it took on the shape of a cone. In 1944, Bethe became the first physicist to properly determine the transmitted intensity of light through a subwavelength aperture [7]. With the use of fictitious magnetic charges and moments within the aperture, he was able to satisfy the perfect electric conductor (PEC) boundary conditions within the aperture. He found that light transmission through a deeply subwavelength aperture of diameter d in an infinite PEC sheet should behave as,

$$T \propto \left(\frac{d}{\lambda}\right)^4 , \tag{1.1}$$

with λ being the wavelength. Though corrections have been made over the ensuing decades, this relation is still widely accepted [8].

Since Bethe's discovery, devices that generate T greater than what would be anticipated based on the geometric size of the apertures have emerged. This increased T is refereed to as extraordinary optical transmission (EOT). Schemes that generate EOT involve light matter interactions where either periodic structures or surface imperfections convert light into surface plasmons that propagate through the aperture and re-emit on the other side [9], or geometry-based cavity resonances increase photonic coupling [10, 11]. Essential to all of these schemes is the continual progress of precision micro and nano-scale fabrication techniques. As these techniques have improved over time, so has the researcher's ability to discover previously unknown phenomena and surpass previously-reported limits.

1.3 Integrated photonics

The ability to miniaturize electronic circuits in the form of microprocessors was potentially the greatest engineering feat of the 21st century. It allowed the average consumer to source any information; photograph, video, article, movie, news, etc. with a device that can fit in their pocket. The Intel 4004 microprocessor with its 2,400 transistors revolutionized the industry by being the first commercially available microprocessor in 1971 [12]. Since this moment, the increase in transistor count on leading edge microprocessors has roughly

followed Moore's Law, which projects that their number will double every two years [13]. With a quick calculation, one can see that, based on 4004's 2,400 transistors in 1971, the leading edge consumer microprocessor in 2023 should have roughly 2^{26} x 2,400 = 161,061,273,600 transistors. Indeed Apple's M2 Ultra chip (the leading microprocessor available to consumers in 2023) contained 134 billion transistors [14], right on track with Moore's prediction. This continual progress has, however, masked a fundamental shift in microchip development. Engineering was originally focused on the miniaturization of transistors but, with the physical limits of fabrication techniques being approached, focus now shifts to creating novel architectures, devices and integration schemes [15]. With a projected 147 zettabytes (1zb = 10^{21} bytes) of data to be created, captured, copied, and consumed in 2024 compared to just 12.5 zettabytes in 2014 [16], pressure to continue this unrelenting progress is higher than ever.

Integrating photonic and electronic devices into one monolithic chip is a solution that has gained traction over the past decade. One particular benefit to this scheme is the ability to multiplex many channels of data into one physical waveguide to allow much higher data transfer rates per cable when compared to their electronic counterparts. Recently, Intel reported data transfer rates of 256 Gbps/fiber using a silicon photonic microring dense wavelength division multiplexing (DWDM) transmitter scheme [17]. This transfer rate is more than 3 times faster than a state of the art USB4 gen 3 cable [18]. Potentially even more critical than the increased transfer rates of PICs is their decrease in power

consumption. This increased efficiency is due not only to the the decrease in losses from photonic signals, but also to the greatly reduced heat generation from photonic circuitry. With cooling contributing to roughly 40% of the power consumption in data centers worldwide [19, 20], replacing not only inter- but also intra-chip electronic signals with photonic ones would greatly reduce their power consumption, cost and environmental impact. Fortunately, this vision has already begun to be realized. Optical input/output (I/O) devices for data centers are now available to the consumer thanks to companies like Ayar Labs whose chiplets and lasers allow for 2 Tbps per chiplet data transfer which is 1000 times the rate of their electronic counterparts with 1/10th the energy consumption. [21]

Optical I/O, however, isn't the only benefit of PIC chips. Quantum computing is one of the many PIC applications that has recently gained traction. One particular scheme that is relevant to the work contained in this thesis is entangled photon pair generation using microring resonators and photonic crystal cavities [22,23,24]. These techniques rely on ultrafast laser pulses to generate energy-time-entangled photons. This means that a frequency measurement made by a detector on one of the photons will immediately determine the time at which the other photon will reach a separate detector. This type of entanglement is especially interesting because it is robust over long distances and enables several new methods of cryptography, among other applications. Researches have begun to achieve success with this technique and have demonstrated Bell type inequality violations in their experiments [25], which proves the generation and measurement of entangled states [22-24, 26].

To understand how these PICs work, let's briefly introduce the waveguides, GCs, microring resonators, and PhCs that serve as some of the main building blocks.

1.4 Waveguides

To have a functioning optical circuit, one must first be able to guide light. In photonics, this is most often done with circuit elements known as waveguides. On the macro-scale, these waveguides can be optical fibers which consist of a glass core surrounded by a lower index of refraction cladding [27]. When the core is large compared to the wavelength, total internal reflection and geometric (ray) optics govern the propagation. However, as the diameter of the core decreases, true waveguide properties begin to dominate the propagation, and the resonant modes of the fiber can be seen [28]. The field distribution of each mode depends on the geometry of the fiber and the wavelength of the propagating light.

As the diameter of the core decreases further, the number of modes is limited until only the fundamental mode(s) that can be supported by the waveguide [29]. An optical fiber of this type is known as a single mode fiber. Critically, for both this thesis and telecommunication applications, a large portion of the wave's energy in this mode is carried outside the core. This means that, although the wave propagates along the waveguide core, the wave itself is not contained within the core. Figure 1.1 depicts the field distribution of a fundamental mode for a rectangular Si waveguide surrounded by SiO_2 cladding. Note how the field extends into the SiO_2 cladding on the sides, and past the

cladding into the air on top. For the purposes of this thesis, this means that we will be able to access and measure this field. For telecommunication, it means that if the cladding is a low loss material, the signal attenuation can be minimized when single mode fibers are utilized [28]. This low loss nature and ease of use make optical fibers desirable for many application, from long distance communication (like high speed interned), to lab-based optical experiments (like coupling light from a laser or to a detector), and everything in between.

Though optical fibers are relatively low loss across a large spectral range, in telecom applications it is desirable to transmit signals at wavelengths with the lowest possible attenuation per kilometer. Originally, in the mid 1970's, it was believed that this occurred in what is now conveniently referred to as the original band (O-band), with near infrared (NIR) wavelengths ranging from 1260 to 1360 nm [30]. However, as fabrication techniques improved and the impurities in silica glass-cored fibers decreased, it was found that, despite the increase in chromatic dispersion, the conventional band (C-band), which encompasses wavelengths from 1530 to 1565 nm, features the lowest attenuation per kilometer [31]. While glass optical fibers are ideal for macro-scale applications, micro- and nano-scale PICs require a slightly different solution.

Because of fabrication constraints for a chip-packaged PIC, waveguides with a rectangular cross section are often used in place of the circular core solution used in optical fibers. Additionally, since complementary metal-oxide-semiconductor (CMOS) foundries are well versed in Si-based fabrication, and
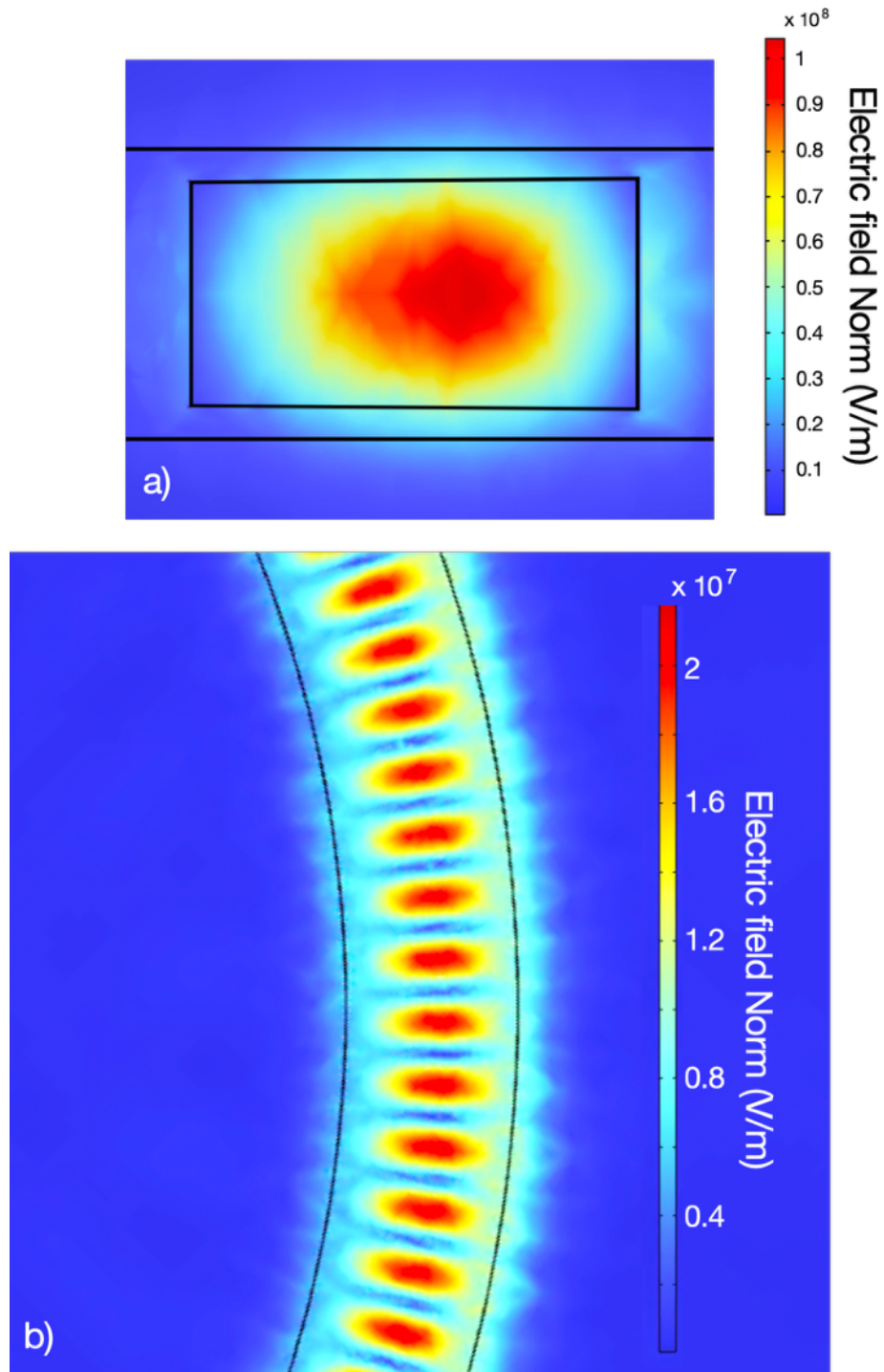
Figure 1.1 Simulated electric field norm* of a rectangular Si buried in SiO₂ waveguide in the form of a ring resonator.
(a) Cross sectional image depicting r-z plane and (b) x-y plane.

* normE = sqrt(realdot(Ex,Ex) + realdot(Ey,Ey) + realdot(Ez,Ez))

because of its low loss nature in the NIR, Si is often chosen to be the waveguide core [32]. Despite these differences, the principles that dictate wave propagation through the Si-cored waveguides are the same as those that govern fiber optics with sub-wavelength sized cores.

1.5 Vertical grating couplers

Often, in both lab-based experiments and commercial applications, it is desirable to use lasers and/or detectors that are not monolithically integrated onto a CMOS chip due to cost or packaging constraints. Forgoing this integration, however, means that light must be coupled from an optical fiber (which is connected to a laser and/or detector) to the waveguides on a chip. Though there are several fiber-to-chip coupling techniques, the device that we will focus on in this thesis is the in-plane vertical grating coupler (GC).

A GC serves two main purposes. The first is to change the energy distribution of the incoming mode. Since the optical fiber will often have a much larger diameter core than the PIC waveguide, to optimize the coupling efficiency, the energy distribution must be squeezed to achieve optimal modal-overlap. This is often done with a taper to a diffraction grating. In addition to this squeezing, the direction of wave propagation must be changed from out-of-plane to in-plane. Bending the direction of light propagation is done via Bragg diffraction using subwavelength patterning of the Si waveguide structure [33]. A cartoon image of the side view of such a grating coupler is depicted in Figure 1.2 (a) and a GC used in our own experiments is seen in Figure 1.2 (b).

9

There are many advantages to this style of GC. Since the GC is in-plane with the PIC, the fabrication of the device would be no more challenging than fabricating the rest of the circuit. Additionally, since it is a vertical GC, as long as there is optical access to either the top or bottom of the chip, light can be coupled to any PIC regardless of its location on the chip. Additionally, due to the symmetric nature of a planar grating coupler, it is often the case that the same design that was used for fiber-to-chip coupling can be used for chip-to-fiber coupling. There are, however, some drawbacks to contend with. Since Bragg diffraction is quite angle and polarization sensitive, the coupling angle and polarization must be carefully tuned to maximize the efficiency. Most notably though, GCs often suffer from large losses. This can be due to uncoupled light propagating past the coupler, or vertical symmetry splitting light both up and down in the chip-to-fiber direction, along with numerous other reflections and issues that limit efficiency [34]. Because of these issues, a large amount of work continues to be put into optimizing GC design, such as creating quasi 3-dimensionality to break vertical symmetry, and reducing the birefringence of the grating [35, 36].

1.6 Microring resonators

With the ability to couple light to and from a PIC and transmit it along a desired path, we now turn our attention to one of the most essential building blocks in PIC design: the passive microring resonator. A microring resonator is a circular waveguide that stores light in a resonant manner. In a monolithic PIC chip, the ring is often constructed from the same Si as the rest of the circuit and
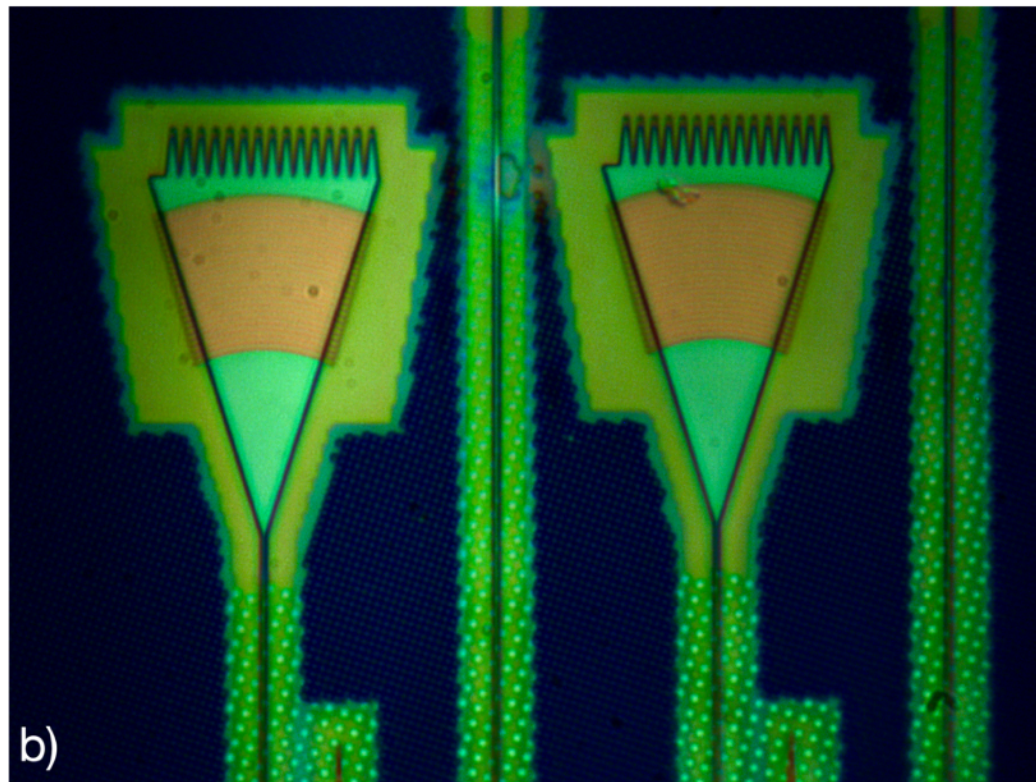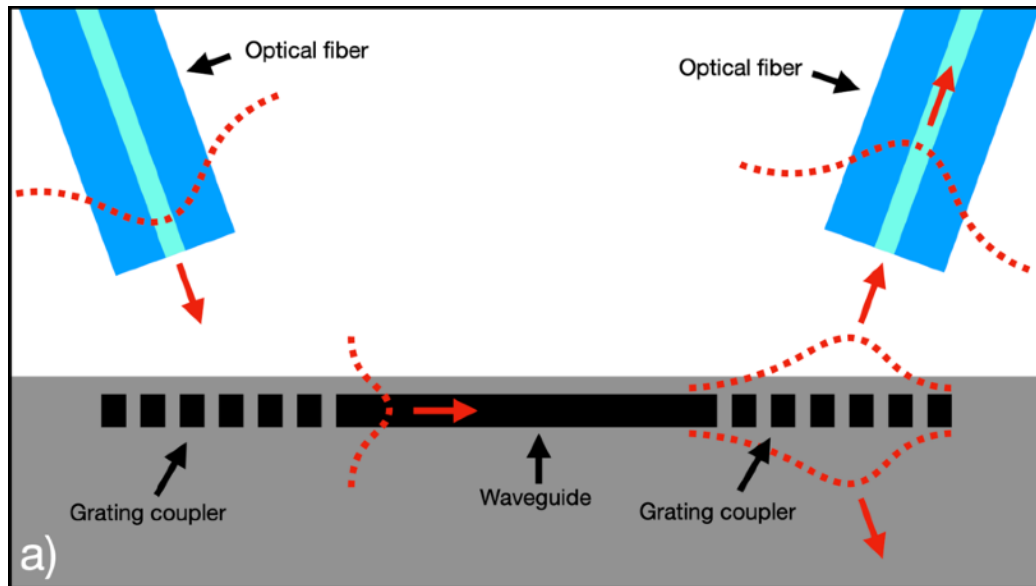
Figure 1.2 Grating couplers.
(a) Cartoon of grating coupler function. Red arrows depict direction of light propagation with the dotted red lines showing field intensity profile. Light blue is the fiber cladding with aqua being the core. (b) Optical micrograph of the grating couplers and waveguides used in our experiments.

is evanescently coupled to at least one of the PICs waveguides [37]. As the name suggests, these rings are usually at least several microns in diameter. The resonant condition of the microring is met when the wavelength of light within the ring is an integer multiple of the effective index $n_{eff}(\lambda_m)$ times the wavelength. At this wavelength, light within the ring will constructively interfere and be stored with very low loss.

Some of the key characteristics of resonators that we will focus on in this thesis are the free spectral range (FSR), the quality factor (Q), the extinction ratio r_e and the complex resonant frequency $\tilde{\lambda}_m$. Figure 1.3 depicts the ring used in our experiments, along with a spectral sweep which describes these important characteristics. The FSR is the wavelength spacing between two successive minima. Q is defined as the energy stored per cycle over the energy lost per cycle and can be determined by dividing the frequency of a given minimum over the full width at half max (fwhm), i.e. $f_o/\Delta f$. r_e is defined as the ratio of optical intensity at the output when the resonant condition is not met divided by the intensity when it is met. Since this ratio can be quite large, it is often measured in decibels (dB) or decibel-milliwatts (dBm).

One common application of microring resonators is as add/drop filters. In this case, a signal containing many wavelengths of light can be input to the circuit. When the signal reaches the resonator, only the wavelengths that meet the resonant condition will be filtered and the remaining wavelengths can pass uninterrupted. Increasing both Q and r_e allows the filter to be more selective and wavelengths closer to the resonant condition to pass without being perturbed.
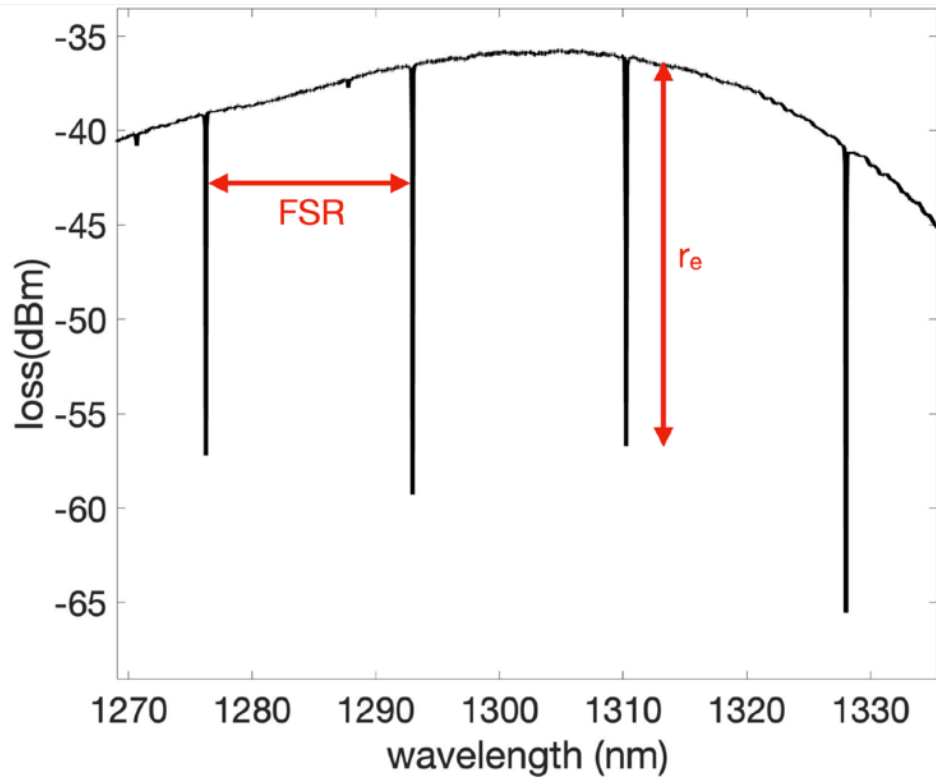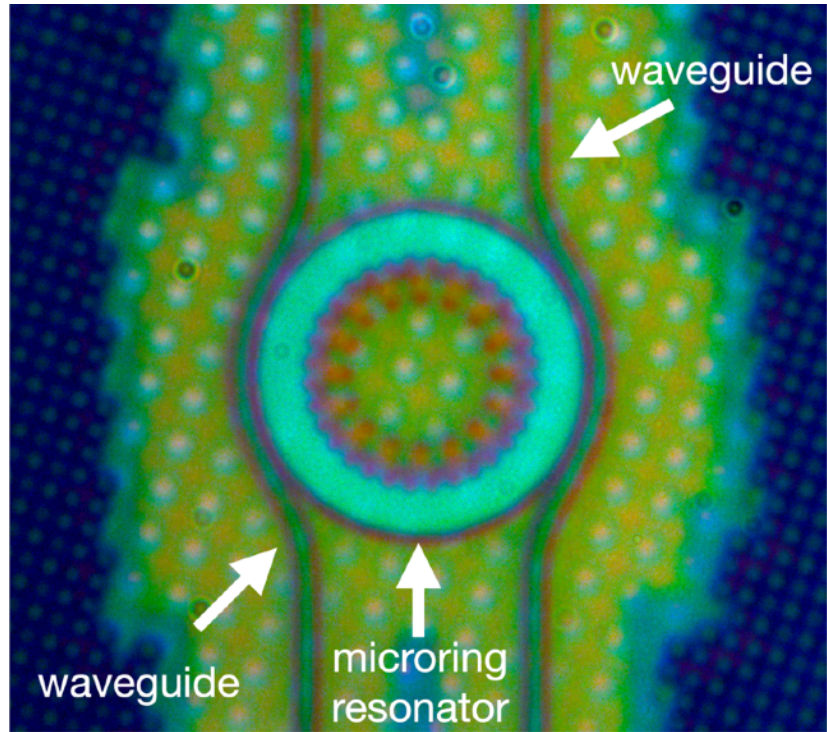
Figure 1.3 Passive spoked microring resonator.
(a) Optical micrograph (b) Spectral sweep including depiction of free spectral range (FSR) and extinction ratio r_e.

1.7 Photonic crystal nanobeam cavities

In a similar vein to microring resonators, photonic crystal cavities (PhC) are high Q photonic resonators used in PICs. PhCs are especially appealing because of their ability achieve high Q with mode volumes (V) on the order of a cubic wavelength $(\lambda/2n)^3$ with n being the index [38]. The basic concept of these cavities is to micro or nano engineer a periodic dielectric array of structures. This patterning creates an allowable range of wave vectors that a materials scientist would recognize as a Brillouin zone with a band gap. Creating a region where the periodicity is broken allows for a defect state to exist in the bandgap. In real space, this state exists at the impurity. Though PhCs can theoretically be 3D, the fabrication of such a device can be more challenging than the 2D and 1D alternatives. Although, both 2D lattices in semiconductor membranes and 1D photonic nanobeam cavities (PhCnB) are quite common, for the purposes of our work, we will focus on PhCnBs.

A PhCnB often consists of a 1D lattice along a waveguide. This periodic structure acts a Bragg mirror in the longitudinal direction, with total internal reflection confining light in the others (as depicted in Figure 1.4). Because of the 1D nature, it is easy to conceptualize the intensity profile of the resonant modes. The fundamental mode (plotted in panel (b)) is just like any other standing wave resonator, with two nulls at either end and an intensity peak in the center. The first order mode will have a null at the center with two intensity peaks on either side. Higher order modes will follow this same trend. There are many advantages to PhCnBs. They are often used as laser sources and filters because

of their high Q, or as sources for spontaneous emission [39]. Manufacturing is relatively straightforward (as long as 100 nm feature size can be achieved) because of their relatively simple design. They are also relatively easy to incorporate into a PIC using evanescent coupling. Because of their narrow width, they also have a smaller footprint than microring resonators.

One of the main areas of interest in PhCnBs is achieving a high Q to V ratio, i.e. confining energy to a small volume while maintaining low losses to radiation. This is quite nontrivial, as to create highly reflective Bragg mirrors requires a large number of small reflections over a long distance. Because of this, often times high Q comes at the expense of increased V [40]. Similarly, when the index contrast of a Bragg mirror is increased, the V is decreased, but so is the Q as the losses to radiation modes are often increased in the process. [39]. Because of this, there is an entire field of research dedicated to developing novel schemes that increase the Q to V ratio of PhCnBs. [39, 41, 42]

1.8 Near-field scanning optical microscopy

Despite the continual research and development into PIC elements, design and implementation is still an iteration-based process that requires many cycles and long time horizons to arrive at an design that achieves targeted performance parameters. There are many reasons for this. First, analytic solutions do not currently exist for the vast majority of PIC elements. Therefore, optimizing designs requires exhaustive numerical-based parameter searches. Optimization is often done using 3D simulation software that solves Maxwell's equations and then maps electric and magnetic fields for a given geometry.
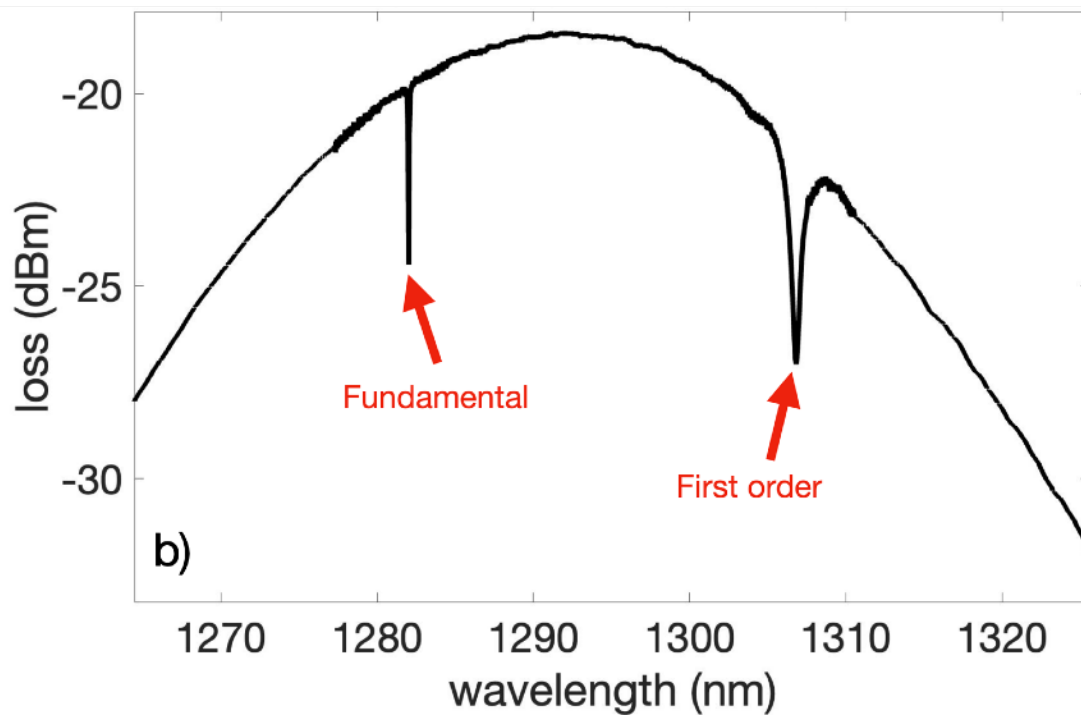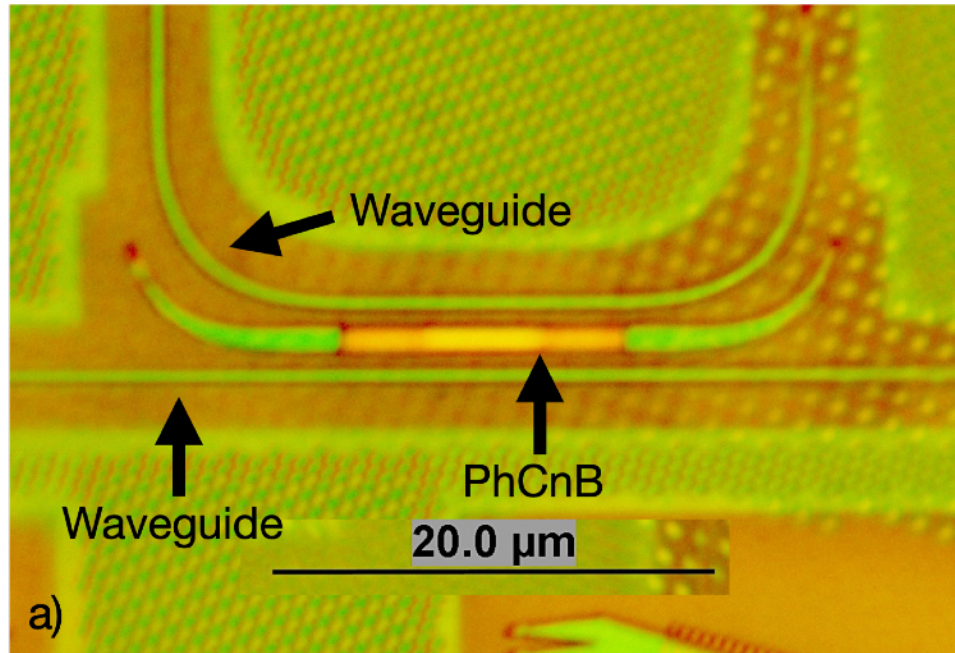
Figure 1.4 Photonic crystal nanobeam cavity (PhCnB).
(a) Optical micrograph. (b) Spectral sweep including labeled fundamental (0th order) and 1st order modes.

Researchers will iterate these designs by slightly changing the geometric parameters and re-running the simulations until the desired targets have been met. Since these optical devices are so sensitive to even nanometer changes, often seemingly minuscule alterations can have drastic effects. Once a design has been optimized, there is still considerable work and further iterations that remain.

It is often the case that actual device performance differs greatly from what was simulated. There are several reasons for this, but one main issue is that material properties and tolerances can vary from foundry to foundry, so a design that works as intended for one, may not necessarily work for another. If this is the case, the PICs would have to be re-designed and optimized with new material parameters and tolerances in mind. With lead times from foundries often being more than a month, this process can be expensive, resource heavy, and time consuming.

Since correlation between simulation and the practical device is so critical in PICs, accurate near-field imaging of the device via near-field scanning optical microscopy (NSOM) could be one way to more throughly and quickly compare simulated and actual device performance.

NSOM is a scanning microscopy technique that breaks the diffraction limit and allows for super-resolution imaging. Abbe approximated the diffraction limit of a microscope to be:

$$d = \frac{\lambda}{2NA} \qquad (1.2)$$

with NA being the numerical aperture of the lens [43, 44, 45]. Therefore, the resolution of any measurement using such a device is inherently limited by NA and wavelength of light. With the NA of a standard microscope lens being below 1 and a highest theoretically possible NA of 1.51 when oil immersion is used, a maximum resolution of only $d \sim \lambda/2$ is possible in air. A slightly higher resolution $d \sim \lambda/3$ can be achieved with oil immersion [46]. This would yield about 750 nm resolution for an optical measurement for a C-band signal.

The most commonly-used NSOM technique is collection-based NSOM (cNSOM). In cNSOM, a sub-wavelength aperture is used to couple light to an optical fiber at a given *x-y-z* location. The fiber then transmits the signal to a detector, as depicted in Figure 1.5. As was discussed in Section 1.2, when apertures become deeply subwavelength, light is transmitted at a diminished intensity that is proportional to $(r/\lambda)^4$. Depending on the sensitivity of the detector, as well as the intensity of the measured signal, the cNSOM aperture diameter can be deeply subwavelength while still producing a clear cNSOM signal [47]. Commercially available cNSOM tips, like the ones our lab purchases from Nanonics [48], can have apertures as small as 25-50 nm, yielding a roughly 30x increase in resolution for imaging C-Band in the far field. Because the location of the NSOM probe is controlled by x, y and z piezoelectric micromanipulators, NSOM images can be taken at nearly any desired plane, and can even be 3 dimensional, which is another advantage over conventional microscope imaging.

Another advantage of NSOM, is the ability to image the near-field. In order for a conventional microscope to generate an image, light needs to propagate from the sample to the lens. With the non-propagating, exponentially decaying, evanescent near-field only extending roughly a wavelength above or below the sample, it can never be detected by a conventional microscope. However, a NSOM probe is able to move close enough to the sample to collect, scatter, or absorb light from this previously inaccessible field [49, 50].

For PICs, this is especially interesting because, as previously mentioned, large amounts of the energy from the optical signal propagate outside of the waveguide core. This signal, however, is not normally coupled to radiation modes, since this would dramatically increase signal losses. This signal, therefore, can only be accessed with near-field imaging techniques. When the near field is physically accessible, NSOM provides an unparalleled high-resolution and nondestructive view into the inner workings of photonic devices [51,52].

1.9 Transmission-based near-field scanning optical microscopy

Aside from the issue of designing PICs with physically accessible near-fields, there are two fundamental problems with cNSOM measurements of PICs; the $(r/\lambda)^4$ signal-to-resolution limit and the significant perturbation caused by near-field scattering off of the cNSOM probe.

The tip generated perturbation is of particular concern with PICs, because, as was discussed previously, even nanometer-sized impurities along a PIC device can cause dramatic changes to performance. Although cNSOM

19
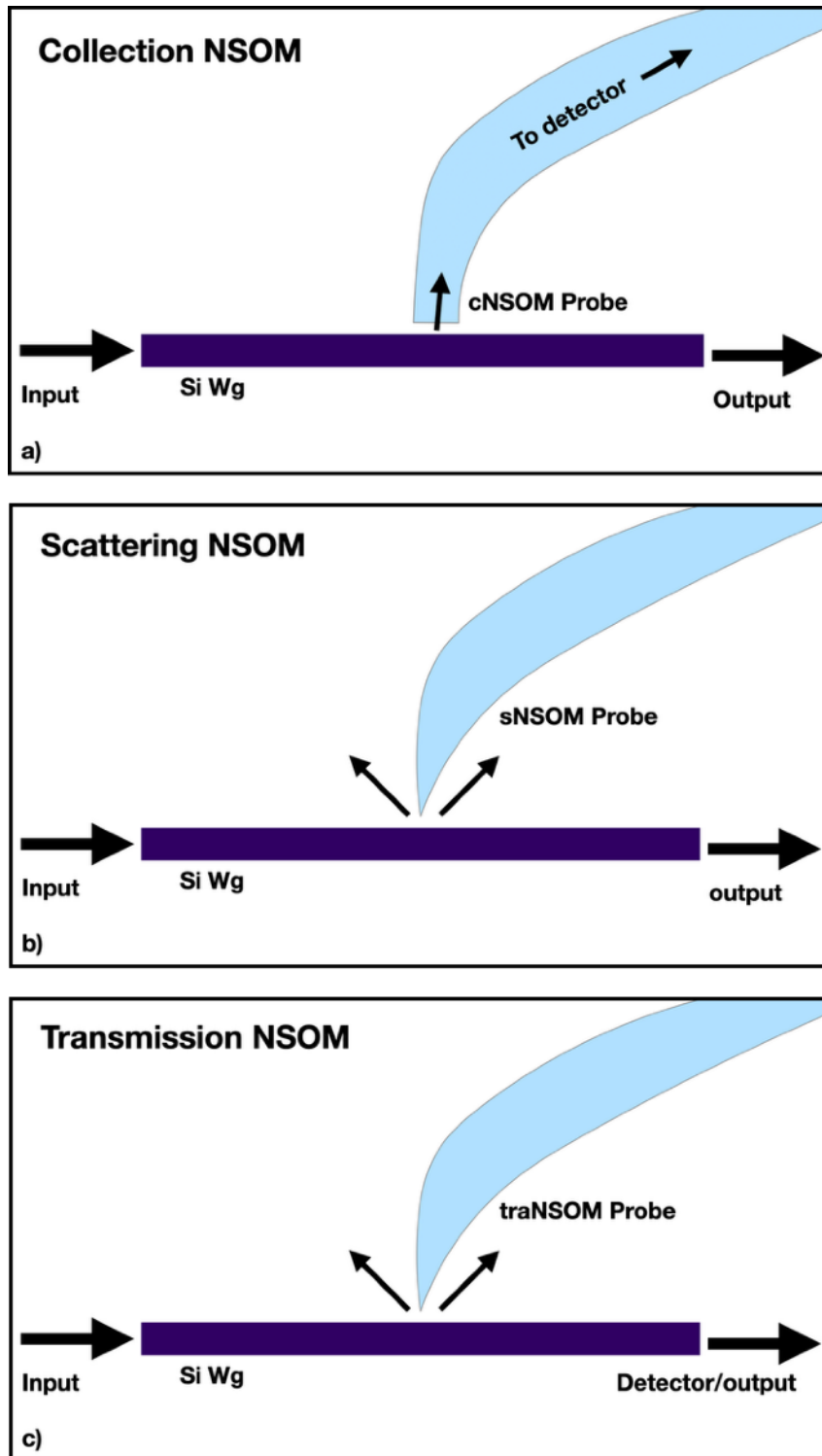
Figure 1.5 Comparison of near-field scanning optical microscopy (NSOM) techniques.
(a) Collection NSOM (cNSOM). (b) Scattering NSOM (sNSOM). (c) Transmission NSOM (traNSOM).

aperture diameters can be as small as 20 nm, the diameter of the tip itself will be much larger (often at least 300-500 nm in diameter). As will be discussed in later Chapters, when perturbations of this size are brought close enough to collect near-field light, they will inevitably perturb the local fields. Whether or not this perturbation is detrimental to device performance depends upon the sensitivity of the device and magnitude of the perturbation.

Fortunately, much smaller non-apertured atomic force microscope (AFM) style probes, which reduce the magnitude of the perturbation, can be implemented in scattering NSOM (sNSOM) (depicted in panel (b) of Figure 1.5) [53]. Rather than collecting light through an optical fiber to be sent to a detector like cNSOM, in sNSOM the tip is used to scatter near-field light into the far-field where both amplitude and phase can be detected [54]. This tip-size reduction is ideal for PIC measurements as it both increases resolution while decreasing tip-generated losses. The added complexity, however, of an sNSOM measurement compared to more traditional cNSOM can make implementation more challenging.

Transmission based NSOM (traNSOM) solves the main issues of both cNSOM and sNSOM. As shown in panel (c) of Figure 1.5, traNSOM measurements are conducted using an aperture-less tip just like sNSOM. So, traNSOM measurements benefit from the same increased resolution and decreased losses when compared to cNSOM [55]. Unlike sNSOM, however, the signal is collected at the PIC output. This greatly reduces the system complexity compared to sNSOM. TraNSOM is ideal for measuring PICs because all that is

needed to conduct a measurement is physical access to the near-field and a sharp AFM-style tip to generate the perturbation. The same inputs and outputs can be used as in normal operation with minimal changes to device operation and performance. If the near-field is not already accessible, additional etching steps can often allow it to be reached without too much effort. Because of its ease of implementation, capability of high resolution images and surprising lack of current use in the field, studying traNSOM scans of PICs will be a main focus of this thesis.

1.10 Outline of thesis

Chapters II-VI of this thesis cover near-field imaging of integrated photonics-electronics chips. Chapter II covers theory and simulation of the interaction between a near-field probe and resonant integrated photonic circuit (PIC) devices. Chapter III delves into the essentials of near-field scanning microscopy (NSOM) on PIC devices. First, common pitfalls from previously reported NSOM scans are discussed. Next, our NSOM on PIC technique is outlined, which avoids these previously reported issues. In Chapters IV-VI we use the lessons from Chapter III to generate near and far field maps of various PIC devices integrated onto the same monolithic complementary metal-oxide-semiconductor (CMOS) chip. In Chapter IV a 3D map of the far field beam angle and profile from a vertical grating coupler (GC) is generated. In Chapters V and VI high resolutions NSOM scans of a microring resonator and photonic crystal cavity (PhC) are reported. We change gears for Chapter VII and focus on the

novel transmission T properties of subwavelength cylindrical waveguide

apertures in real opaque metal films made of Au and Cr.

[1] C. Huygens, in *Traité De La Lumière* (Leiden, 1690).

[2] I. Newton, in *Opticks: or, A treatise of the reflexions, refractions, inflexions and colours of light. Also two treatises of the species and magnitude of curvilinear figures.* (London, 1704).

[3] A. Einstein, Ann. of Phys. **17**, 132-147 (1905). doi: 10.1002/andp.200590004

[4] A. H. Compton, "A quantum theory of the scattering of x-rays by light elements," Phys. Rev. **21**, 483-502 (1923). doi: 10.1103/PhysRev.21.483

[5] L. de Broglie, "Recherches sur la théorie des quanta," Ann. of Phys. **10**, 22-128 (1925). doi: 10.1051/anphys/192510030022

[6] F.M. Grimaldi, in *Physico-mathesis de Lumine, Coloribus, et Iride, Aliisque Sequenti Pagina Indicatis* 9 (Bologna, 1665).

[7] H.A. Bethe, "Theory of diffraction by small holes," Phys. Rev. **66**, 163-181 (1944). doi: 10.1103/ PhysRev.66.163

[8] C.J. Bouwkamp, "Diffraction Theory," *Rep. Prog. Phys.* **17**, 35 (1954). doi: 10.1088//0034-4885/17/1/302

[9] W. Ebbesen, H.J. Lezec, H.F. Ghaemi, T. Thio, P.A. Woff, "Extraordinary optical transmission through sub-wavelength hole arrays," *Nat.* **391**, 667-660 (1998). doi: 10.1038/35570

[10] F.J. García de Abajo, "Light transmission through a single cylindrical hole in a metallic film", Optics Express **10**, 1475-1484 (2002). doi: 10.1364/OE.10.001475

[11] Q. Cao and P. Lalanne, "Negative role of surface plasmons in the transmission of metallic gratings with very narrow slits," Phys. Rev. Lett. **88**, 057403 (2002). doi: 10.1103/PhysRevLett.88.057403

[12] "The story of Intel 4004," Intel.com, 16 Feb 2024, www.intel.com/content/www/us/en/history/museum-story-of-intel-4004

[13] G.E. Moore, "Progress in Digital Integrated Electronics," *IEEE International Electron Device Meeting Technical Digest* **21,** 11-13 (1975)

[14] "Apple introduces M2 Ultra." Apple.com, 16 Feb 2024, www.apple.com/newsroom/2023/06/apple-introduces-m2-ultra/

[15] T.N. Theis, "The End of Moore's Law: A New Beginning for Information Technology"

[16] P. Taylor, "Amount of data created, consumed, and stored 2010-2020, with forecasts to 2025," statista.com, 27 Feb 2024, https://www.statista.com/statistics/871513/worldwide-data-created/

[17] C. Levy, Z. Xuan, D. Huang, R. Kumar, J. Sharma, T. Kim, C. Ma, G. Su, S. Liu, J. Kim, X. Wu, G. Balamurugan, H. Rong, and J. Jaussi "A 3D-integrated 8λ x 32 Gbps/λ Silicon Photonic Microring-based DWDM Transmitter," *IEEE CICC 2023*

[18] GRL Team, "Welcome to the 80 Gbps Ultra High Speed Era of USB4," graniteriverlabs.com, 27 Feb 2024, https://www.graniteriverlabs.com/en-us/technical-blog/usb4-80-cio80

[19] H. Rong, H. Zhang, S. Xiao, C. Li, and C. Hu, "Optimizing energy consumption for data centers," *Renewable and Sustainable Energy Rev.* **158**, 674-691 (2016). doi: 10.1016/j.rser.2015.12.283

[20] R. Danilak, "Why Energy Is A Big And Rapidly Growing Problem For Data Centers," Forbes.com, 28 Feb 2024, www.forbes.com/sites/forbestechcouncil/2017/12/15/why-energy-is-a-big-and-rapidly-growing-problem-for-data-centers/?sh=194cc4505a30

[21] R. Meade, S. Ardalan, M. Davenport, J. Fini, C. Sun, M. Wade, A. Wright-Gladstein, and C. Zhang, "TeraPHY: A High-Density Electronic-Photonic Chiplet for Optical I/O from a Multi-Chip Module," *2019 Opt. Fiber Commun. Conf.* Exhib. OFC 2019 - Proc., no. Mcm, 5–7 (2019)

[22] J.W. Silverstone, R. Santagati, D. Bonneau, M.J. Strain, M. Sorel, J.L. O'Brien, and M.G. Thompson, "Qubit entanglement between ring-resonator photon-pair sources on a silicon chip," *Nat. Comm.* **6**, 7948 (2015). doi: 10.1038/ncomms8948

[23] T.J. Steiner, J.E. Castro, L. Chang, Q. Dang, w. xie, J. Norman, J.E. Bowers, and G. Moody, "Ultrabright Entangled-Photon-Pair Generation from an AlGaAs-On-Insulator Microring Resonator," *PRX Quantum* **2,** 010337 (2021) doi: 0.1103/PRXQuantum.2.010337

[24] A. Chopin, A. Barone, I. Ghorbel, S. Combrié, D. Bajoni, F. Raineri, M. Galli, and A. De Rossi, "Ultra-efficient generation of time-energy entangled photon pairs in an InGaP photonic crystal cavity," *Commun. Phys*. **6**, 77 (2023) doi: 10.1038/s42005-023-01189-x

[25] J.S. Bell, "On the Einstein Podolsky Rosen paradox," *Phys. Physique Fizika* **1**, 195 (1964) doi: 10.1103/PhysicsPhysiqueFizika.1.195

[26] J.P.W. MacLean, J.M. Donohue, and K. Resch, "Direct Characterization of Ultrafast Energy-Time Entangled Photon Pairs," *Phys. Rev. Lett.* **120**, 053601 (2018) doi: 10.1103/PhysRevLett.120.053601

[27] US patent 3845293, Börner, Manfred, "Electro-optical transmission system utilizing lasers"

[28] E. Snitzer and H. Osterberg, "Observed Dielectric Waveguide Modes in the Visible Spectrum," *JOSA* **51**(5), 499-505 (1961)

[29] K. C. Kao and G.A. Hockham., "Dielectric-fibre surface waveguides for optical frequencies," *Proc. Inst. Elec. Eng.* **113** (7), 1151 (1966).

[30] FiberLabs Inc., "Original Band (O-band)," fiberlabs.com, 29 Feb 2024, www.fiberlabs.com/glossary/original-band/ www.fiberlabs.com/glossary/conventional-band/

[31] FiberLabs Inc., "Conventional Band (C-band)," fiberlabs.com, 29 Feb 2024, www.fiberlabs.com/glossary/conventional-band/

[32] R. Soref and J. Larenzo, "All-silicon active and passive guided-wave components for λ = 1.3 and 1.6 µm," *IEEE Journal of Quantum Electronics* **22**(6), 873-879 (1986) doi: 10.1109/JQE.1986.1073057

[33] W.H. Bragg, "The Reflexion of X-rays by Crystals," *Proc. R. Soc. Lond. A*. **88** (605): 428–438 (1913) doi: 10.1098/rspa.913.0040

[34] L. Cheng, S. Mao, Z. Li, Y. Han, and H.Y. Fu, "Grating Couplers on Silicon Photonics: Design Principles, Emerging Trends and Practical Issues," *Micromachines* **11**(7), 666 (2020) doi: 10.3390/mi11070666

[35] F. Van Laere, T. Claes, J. Schrauwen, S. Scheerlinck, W. Bogaerts, D. Taillaert, L. O'Faolain, D. Van Thourhout, and R. Baets, "Compact Focusing Grating Couplers for Silicon-on-Insulator Integrated Circuits," *IEEE Photonics Tech. Lett.* **19**(23), 1919-1921 (2007) doi: 10.1109/LPT.2007.908762

[36] B. Zhang, M. Schiller, K. Al Qubaisi, D. Onural, A. Khilo, M.J. Naughton, and M.A. Popović, "Polarization-insensitive 1D grating coupler based on a zero-birefringence subwavelength corelet waveguide," *Optics Lett.* **47**(13), 3167-3170 (2022) doi: 10.1364/OL.459306

[37] P. Dumon, W. Bogaerts, V. Wiaux, J. Wouters, S. Beckx, J. Van Campenhout, D. Taillaert, B. Luyssaert, P. Bienstman, D. Van Thourhout, and R. Baets, "Low-Loss SOI Photonic Wires and Ring Resonators Fabricated With Deep UV Lithography," *IEEE Journal of Quantum Electronics* **16**(5), 1328-1330 (2004) doi: 10.1109/ LPT.2004.826025

[38] J.S. Foresi, P.R. Villeneuve, J. Ferrera, E.R. Thoen, G. Steinmeyer, S. Fan, J.D. Joannopoulos, L.C. Kimerling, H.I. Smith, and E. P. Ippen , "Photonic-bandgap microcavities in optical waveguides," *Nat.* **390**, 143–145 (1997) doi: 10.1038/36514

[39] H. Yokoyama "Spontaneous Emission and Laser Oscil- lation in Microcavities," Boca Raton, FL: CRC Press, 1995

[40] P. Lalanne and J.P Hugonin, "Bloch-Wave Engineering for High-Q, Small-V Microcavities," *IEEE Photonics Tech. Lett.* **39**(11), 1430-1438 (2003) doi: 10.1109/ JQE.2003.818283

[41] P.B. Deotare M.W. McCutcheon, I.W. Frank, M. Khan, and M. Lončar, "High quality factor photonic crystal nanobeam cavities," *Applied Phys. Lett.* **94**, 121106 (2009) doi: 10.1063/1.3107263

[42] K. Al Qubaisi, M. Schiller, B. Zhang, D. Onural, M.J. Naughton, and M.A. Popović, "Cubic-wavelength mode volume photonic crystal nanobeam cavities in a monolithic CMOS platform ," *Optics Lett.* **48**(4), 1024-1027 (2023) doi: 10.1364/ OL.481483

[43] G.B Airy, "On the diffraction of an object-glass with circular aperture," *Transactions of the Cambridge Philisophical Soc.* **5**, 283-291 (1835)

[44] E. Abbe, "Beiträge zur Theorie des Mikroskops und der mikroskopischen Wahrnehmung," *Archiv f. Mikrosk. Anatomie.* **9**, 413-468 (1873) doi: 10.1007/ BF02956173

[45] L. Rayleigh "LVI, investigations in optics, with special reference to the spectroscope," *Phil. Mag. Ser.* **5**, 477-486

[46] M. Abramowitz, "Original Band (O-band)," Olympus-lifesciences.com, 5 March 2024, www.olympus-lifescience.com/en/microscope-resource/primer/anatomy/ numaperture/

[47] E.A . Ash and G. Nicholls, "Super-resolution Aperture Scanning Mircroscope ," *Nature*, **237**, 510-512 (1972) doi: 10.1038/237510a0

[48] https://www.nanonics.co.il/products/multiview-4000-system

[49] U. Dürig, D.W. Pohl, and F. Rohner, "Near-field optical-scanning microscopy," *J. Appl. Phys.* **59**, 3318-3327 (1986) doi: 10.1063/1.336848

[50] E. Betzig, A. Lewis, A. Harootunian, M. Isaacson, and E. Kratchmer., "Near Field Scanning Optical Microscopy (NSOM): Development and Biophysical Applications," *Biophysics J.* **49**, 269-279 (1986) doi: 10.1016/S0006-3495(86)83640-2

[51] S. Bourzeix, S. Bourzeix, J. M. Moison, F. Mignard, F. Barthe, A. C. Boccara C. Licoppe B. Mersali M. Allovon, and A. Bruno "Near Field optical imaging of light propagation in semiconductor waveguide structures," *Appl. Phys. Lett.* **73**, 1035-1037 (1998) doi: 10.1063/1.122076

[52] G. H. Vander Rhodes, B. B. Goldberg, M. S. Ünlü, S. T. Chu, W. Pan, T. Kaneko, Y. Kokobun, and B. E. Little, "Measurement of internal spatial modes and local propagation properties in optical waveguides," *Appl. Phys. Lett.* **75**, 2368-2370 (1999) doi: 10.1063/1.125017

[53] F. Zenhausern, M.P. O'Boyle, and H.K. Wickramasinghe, "Apertureless near-field optical microscope," *Appl. Phys. Lett.* **65**, 1623-1625 (1994) doi: 10.1063/1.112931

[54] "Scattering SNOM," Bruker.com, 5 March 2024, www.bruker.com/en/products-and-solutions/infrared-and-raman/nanoscale-infrared-spectrometers/scattering-snom.html

[55] J.T. Robinson, S.F. Preble, and M. Lipson, "Imaging highly confined modes in sub-micron scale silicon waveguides using Transmission- based Near-field Scanning Optical Microscopy," *Optics Express* **14**(22), 10589 (2006) doi: 10.1364/OE.14.010588

Chapter II

Theory and simulations of NSOM scans of a microring resonator

2.1 Introduction

The goal of this research is to gain an in depth knowledge of the near-field of photonic devices. With that in mind, a study would not be complete without rigorous simulations, which will provide us with in depth knowledge as to how our experimental techniques interact with this field, and the properties of the device itself. The goal of these simulations is not necessarily to re-create any of the experiments that were conducted on the photonics chips or in the lab itself, but rather to further understand how an NSOM probe interacts with a resonant photonic device, and then use this knowledge to conduct accurate near-field measurements.

2.2 Time and frequency domain solvers

Finite difference time domain (FDTD) solvers are among the most ubiquitous techniques for simulating the 3D electromagnetic response to a signal. As the name implies, FDTD discretizes Maxwell's equations in both time and space to obtain a desired steady-state solution [1]. It is a full wave solver, meaning that the full electromagnetic wave propagation is calculated and there are no simplifications to Maxwell's equations. In this technique, a 3D model is broken up into a volumetric grid of mesh cells (the size of which is determined by the user) each with its own differential equations to be solved (usually via leapfrogging the **E** and **H** solutions). This iteration continues until either the

desired energy decay criterion is met (it has "converged"), or the maximum

iteration has been reached (it has not "converged"). Finite difference frequency

domain (FDFD) behaves much like FDTD, but with Maxwell's equations Fourier

transformed into a reciprocal representation in frequency space. With this

transform into frequency space, equations are defined for a single frequency

and can be represented as a matrix. Researches have taken advantage of this to

generate algorithms that simplify complex problems and architectures

(particularly with periodic or resonant structures) into ones that are much less

taxing computationally [2].

FDTD and FDFD can often be thought of as "simulated experiments"

because they are set up much in the same way one would set up an experiment

in a lab. For example, a user must define an input and an output port in the

same way a lab researcher would connect a light source and a detector.

Similarly, in order to find a resonance, a range of frequencies must be swept

across, just as in the lab.

While both of these techniques have been workhorses of electromagnetic

research for engineers and physicists alike for more than 30 years, our work

requires a different approach. This is because both FDTD and FDFD rely on

calculating the electromagnetic response to an input signal. In the case of

resonant devices, this is a "brute force" approach that ignores the elegance of a

resonator. Resonators have inherent resonant frequencies that are independent

of the driving frequency (within linear response theory). So, rather than solving

for many frequencies until the correct one is found, it is much more appropriate to use the inherent geometry of the resonator itself to tease out the eigenmodes.

2.3 Electromagnetic micro- and nano-resonators

The microrings and PhCnBs that we will be studying are both examples of electromagnetic micro or nano resonators. All electromagnetic resonators follow the same characteristic interaction between light and the resonant structures where, after an excitation from a pulse of light, an intrinsic mode (or modes) of the device briefly stores this energy before releasing it in a spatially exponentially decaying fashion. Since these structures are resonant, there is a characteristic frequency ω_m associated with each intrinsic mode. Take for example the string of a guitar. If one were to pluck the string, it would resonate at a characteristic frequency. The same holds true for electromagnetic resonators but, instead of storing mechanical energy, they store electromagnetic energy.

The characteristic time that this energy is stored is known as the mode lifetime or τ_m. Going back to the guitar string example, after being plucked, it will ring resonantly for a period of time before once again returning to rest due to damping. If the string vibrates longer, then the lifetime is increased and *vice versa*. The lifetime is inversely related to another quantity known as the loss rate Γ_m:

$$\tau_m = \frac{1}{\Gamma_m} \tag{2.1}$$

31

This parameter describes how much energy is radiated from the resonator to the environment per cycle. Measuring how long it takes the guitar string to ring out, we can calculate how much energy the guitar string loses in each round trip at a given frequency.

An important measure associated with the loss rate and frequency is the quality factor or Q:

$$Q_m = \frac{\omega_m}{\Gamma_m} = \omega_m \cdot \tau_m \qquad (2.2)$$

which is the ratio of energy stored per cycle over energy lost per cycle. So, the more energy that can be stored and the less energy that is lost to the environment, the greater the Q. Another way of looking at it would be, higher Q cavities can store energy longer than low Q cavities. In the case of micro resonators in PICs, the Q can be quite large ($> 10^5$) which, from equation 2.2, tells us that the losses are very low. For computing both numerical and analytical solutions, it can be tempting to ignore losses in this case, since they are so small. However, as we will discuss later in this Chapter and thesis, these losses are essential to understanding these physical systems and ignoring them would provide an incomplete and incorrect picture of the physics at play. These losses cannot be ignored, therefore we must rigorously introduce and understand them. This will be a main goal for not only this Chapter but also this thesis and work.

2.4 Quasi-normal modes

The resonant, quasi-normal modes (QNMs) of an electromagnetic system are found by solving the time-harmonic source-free Maxwell's equations [3] :

$$\nabla \times \tilde{\mathbf{E}}_m(\mathbf{r}) = -i\tilde{\omega}_m \mu(\mathbf{r}, \tilde{\omega}_m)\tilde{\mathbf{H}}_m(\mathbf{r})$$

$$\nabla \times \tilde{\mathbf{H}}_m(\mathbf{r}) = i\tilde{\omega}_m \varepsilon(\mathbf{r}, \tilde{\omega}_m)\tilde{\mathbf{E}}_m(\mathbf{r}).$$ (2.3) (2.4)

$\tilde{\omega}_m$ is the mth complex eigenfrequency defined as

$$\tilde{\omega}_m = \omega'_m + i\omega''_m = \omega_m + 1/2\Gamma_m$$ (2.5)

where ω'_m is the real component of the resonant frequency for the mth resonant mode (what we would measure in a spectral sweep measurement) and ω''_m is the combined losses for that mode. μ and ε are the spatially-varying and frequency-dependent magnetic permeability and electric permittivity of the system, respectively.

Although it may seem tedious, it is important to the following work that we take a close look at the distinction between approaching high Q cavities as being part of a closed (lossless) or an open system that radiates energy.

2.5 Hermitian (closed) systems

As with any theoretical work, one of the most critical stages happens before any modeling has begun, when we are selecting which approximations to make, and what fields we will be solving for. An approximation that is often made for high Q photonic devices, like the ones our collaborators at Boston University (BU) have designed, is that there are essentially no losses in the system. This is known as "Hermitian."

Before moving further, it will be useful to formally define the mode volume V. Q describes how the resonance behaves as time evolves, while V describes the spacial extent of the mode by determining the interaction between the cavity mode and a small polarizable object at position **r** and polarization direction **u**. (Bold letters are used to indicate vectors). With the assumption of a high Q cavity and Hermitian system, the mode volume is found to be

$$V(\mathbf{r}, \mathbf{u}) = \frac{\int [\varepsilon |\tilde{\mathbf{E}}|^2 + \mu_0 |\tilde{\mathbf{H}}|^2] d^3\mathbf{r}}{2\varepsilon(\mathbf{r}) |\tilde{\mathbf{E}}(\mathbf{r}) \cdot \mathbf{u}|^2}, \tag{2.6}$$

as originally reported by Bethe [4].

Using the mode volume as a starting point, cavity perturbation theory can be applied to determine the change in resonant frequency $\Delta\tilde{\omega}_m$ of a non perturbed state $\tilde{\omega}_m$ with the presence of a small perturbation with a dipolar polarizability α at a position $\mathbf{r}_0$. For the NSOM research we will be conducting, this is a critical calculation, because it should directly describe how the cavity resonance will respond to the presence of the NSOM tip. The result when assuming a closed system is

$$\frac{\Delta\tilde{\omega}_m}{\tilde{\omega}_m} \simeq \frac{-\alpha\varepsilon(\mathbf{r}_0) |\tilde{\mathbf{E}}(\mathbf{r}_0)|^2}{\int \varepsilon(\mathbf{r}) |\tilde{E}(\mathbf{r}_0)|^2 + \mu_0(\mathbf{r}_0) |\tilde{H}(\mathbf{r}_0)|^2 d^3\mathbf{r}} = \frac{-\alpha}{2V(\mathbf{r})}. \tag{2.7}$$

To test this equation, we can look at how it predicts a small perturbation, like our NSOM tip, will change the characteristic properties of a given resonant device. Since V is defined to be all real, this equation predicts that

$$\Delta\tilde{\omega}_m \propto \tilde{\omega}_m. \tag{2.8}$$

In other words, the changes in both the real and imaginary parts follow an identical spatial dependance. Thus, any shift up in resonant frequency as a result of a perturbation *must* be associated with a decrease in the cavity losses. Similarly, a decrease in resonant frequency *must* come with increased losses. Despite these flaws, this equation and theory have regularly been used to describe the modification of resonant cavity modes in the presence of a perturbation [5,6,7,8].

As a brief personal aside, I spent several months trying to understand why the results of our NSOM measurements and other related experiments didn't align with this Hermitian theory. Over time, I began to doubt myself and my work. Fortunately, when I came across the papers of Dr. Philippe Lalanne describing non-Hermitian resonators, seemingly in an instant, all of my issues were resolved.

2.6 Non-Hermitian (open) systems

To rectify the inconsistencies with assuming the system to be Hermitian when applying perturbation theory, we will follow the approach first used by Lalanne *et al.* to describe the coupling between dipole emitters and dissipative nano-resonators [9,10]. In this theory, the all real mode volume *V* from equation 3.6 is replaced with a complex mode volume $\tilde{V}$, defined as

$$\tilde{V}(\mathbf{r}, \mathbf{u}) = \frac{\int \left[\tilde{\mathbf{E}} \cdot \frac{\partial(\omega\varepsilon)}{\partial\omega} \tilde{\mathbf{E}} - \tilde{\mathbf{H}} \cdot \frac{\partial(\omega\mu)}{\partial\omega} \tilde{\mathbf{H}} \right] d^3\mathbf{r}}{2\varepsilon(\mathbf{r}) \left[\tilde{\mathbf{E}}(\mathbf{r}) \cdot \mathbf{u} \right]^2}. \tag{2.9}$$

It is important to note that, although the numerator grows exponentially when integrated far away from the location of the resonator, the implementation of perfectly matched layers (PML) will dissipate the outgoing field and allow it to converge both numerically and analytically [11].

With this new definition for $\tilde{V}$, cavity perturbation theory can be applied once more to find that

$$\frac{\Delta\tilde{\omega}_m}{\tilde{\omega}_m} \simeq \frac{-\alpha\varepsilon(\mathbf{r}_0)\tilde{\mathbf{E}}(\mathbf{r}_0)^2}{\int\left[\tilde{\mathbf{E}}\cdot\frac{\partial(\omega\varepsilon)}{\partial\omega}\tilde{\mathbf{E}} - \tilde{\mathbf{H}}\cdot\frac{\partial(\omega\mu)}{\partial\omega}\tilde{\mathbf{H}}\right]d^3\mathbf{r}} = \frac{-\alpha}{2\tilde{V}(\mathbf{r}_0)} \qquad (2.10)$$

This re-defined V and $\Delta\tilde{\omega}$ are essential to understand the effect of a small perturbation not only on the frequency, but also the quality factor, of a low Q or "lossy" cavity, The initial emphasis of that work was on modeling resonance shift-based sensing [12,13]. Fortunately, for our purposes, this updated cavity perturbation theory does not only apply to lossy cavities but can also predict the wavelength and Q shifts of a high Q resonator in the presence of a perturbation [14]. Unlike previous results, as shown in Ref. [14], this method can be used to accurately predict increases and decreases in not only the resonant frequency but *also* in the losses, i.e. increases and decreases to Q as a function of perturbation (in our case NSOM tip) position.

If we consider this result practically, it makes complete sense that the system has to be non-Hermitian in order to be properly understood. Practically speaking, we often think of a small perturbation as a scattering source. Therefore, if we want to properly model the effects of a scattering source on a

system, we *must* consider the fact that there will be tip-induced losses. This is especially true for high Q photonic resonators, which, as we know, are very sensitive to nano-scale imperfections.

While it is enlightening to understand the theory behind an NSOM measurement of a high Q photonic resonator, to be truly useful, this theory must be implemented properly in 3D electromagnetic simulations.

2.7 Solvers

This work follows that of **MAN** (Modal Analysis of Nanoresonators), a free software developed over the past decade with many models and examples for solving the QNMs of electromagnetic micro and nanoresonators [15,16]. Though **MAN** itself is entirely open source, certain solvers are designed to work in tandem with COMSOL and CST [17,18], which are commercial multiphysics products with a variety of proprietary solvers, commonly used for 3D electromagnetic simulations. Though there is entirely free QNMPole software in **MAN**, which, as the name suggests, finds the QNMs by searching the complex plane around the pole created by the divergent electromagnetic response at resonance [19], we will instead be using the slightly more robust QNMEig solver, which utilizes COMSOL's RF eigenmode and weak form modules. COMSOL's eigenmode solver is highly effective at finding the NMs of nanoresonators by solving the linearized equations (3.3) and (3.4), however, it is not appropriate for dispersive materials. So, although it is quite straightforward to simulate a micro ring resonator in COMSOL or CST with numerous examples being available in each [20,21], when we add a small metallic perturbation to the system, the

37

problem quickly becomes unsolvable. To understand this, we consider a

material with dispersive permittivity in the form of a Lorentz pole:

$$\tilde{\varepsilon}(\omega) = \varepsilon_\infty \left(1 - \frac{\omega_p^2}{\omega^2 - \omega_0^2 + i\omega\gamma} \right) \tag{2.11}$$

where, ε_∞ is the permittivity at infinite frequency, ω_p the plasma frequency, ω_0

the the resonant frequency, and γ the damping [22,23,24]. Equations (2.3) and

(2.4) are now no longer linear and it is quite likely that COMSOL would be unable

to find a solution. Judicious definitions of two new auxiliary fields, the

polarization $\tilde{\mathbf{P}}$:

$$\tilde{\mathbf{P}} = -\varepsilon_\infty \frac{\omega_p^2}{\omega^2 - \omega_0^2 + i\omega\gamma} \tilde{\mathbf{E}} \tag{2.12}$$

and the current density $\tilde{\mathbf{J}}$:

$$\tilde{\mathbf{J}} = -i\omega\tilde{\mathbf{P}} \tag{2.13}$$

allow us to formulate a linearized eigenvalue problem [25].

$$\begin{bmatrix} 0 & -i\mu_0^{-1}\nabla\times & 0 & 0 \\ i\varepsilon_\infty^{-1}\nabla\times & 0 & 0 & i\varepsilon_\infty^{-1} \\ 0 & 0 & 0 & i \\ 0 & i\omega_p^2\varepsilon_\infty & -i\omega_0^2 & -i\gamma \end{bmatrix} \begin{bmatrix} \tilde{\mathbf{H}}_m(\mathbf{r}) \\ \tilde{\mathbf{E}}_m(\mathbf{r}) \\ \tilde{\mathbf{P}}_m(\mathbf{r}) \\ \tilde{\mathbf{J}}_m(\mathbf{r}) \end{bmatrix} = \tilde{\omega}_m \begin{bmatrix} \tilde{\mathbf{H}}_m(\mathbf{r}) \\ \tilde{\mathbf{E}}_m(\mathbf{r}) \\ \tilde{\mathbf{P}}_m(\mathbf{r}) \\ \tilde{\mathbf{J}}_m(\mathbf{r}) \end{bmatrix} \tag{2.14}$$

For the purposes of solving this series of linearized equations with COMSOL, a further step is taken where equation 2.14 is transformed into the quadratic eigenvalue equation:

$$\hat{\mathbf{K}} \begin{bmatrix} \tilde{\mathbf{E}}_m \\ \tilde{\mathbf{P}}_m \end{bmatrix} + \tilde{\omega}_m \hat{\mathbf{C}} \begin{bmatrix} \tilde{\mathbf{E}}_m \\ \tilde{\mathbf{P}}_m \end{bmatrix} + \tilde{\omega}_m^2 \hat{\mathbf{M}} \begin{bmatrix} \tilde{\mathbf{E}}_m \\ \tilde{\mathbf{P}}_m \end{bmatrix} = 0 \tag{2.15}$$

Just like any other harmonic oscillator, $\hat{\mathbf{K}}$ is the stiffness matrix:

$$\hat{\mathbf{K}} = \begin{bmatrix} \nabla \times \mu_0^{-1} \nabla \times & 0 \\ \varepsilon_\infty \omega_p^2 & -\omega_0^2 \end{bmatrix} \tag{2.16}$$

$\hat{\mathbf{C}}$ is the damping matrix:

$$\hat{\mathbf{C}} = \begin{bmatrix} 0 & 0 \\ 0 & i\gamma \end{bmatrix} \tag{2.17}$$

and $\hat{\mathbf{M}}$ is the mass matrix:

$$\hat{\mathbf{M}} = \begin{bmatrix} -\varepsilon_\infty & -1 \\ 0 & 1 \end{bmatrix}. \tag{2.18}$$

In order to be implemented by COMSOL's weak form module, these equations are converted into their weak form before being entered and then solved. If there are additional poles to be simulated, this can be done by simply increasing the number of auxiliary fields and their related Weak Form PDEs [24].

2.8 3D modeling

As was mentioned previously, the purpose of these simulations is not to exactly re-create the passive spoked ring resonator used experimentally. Rather,
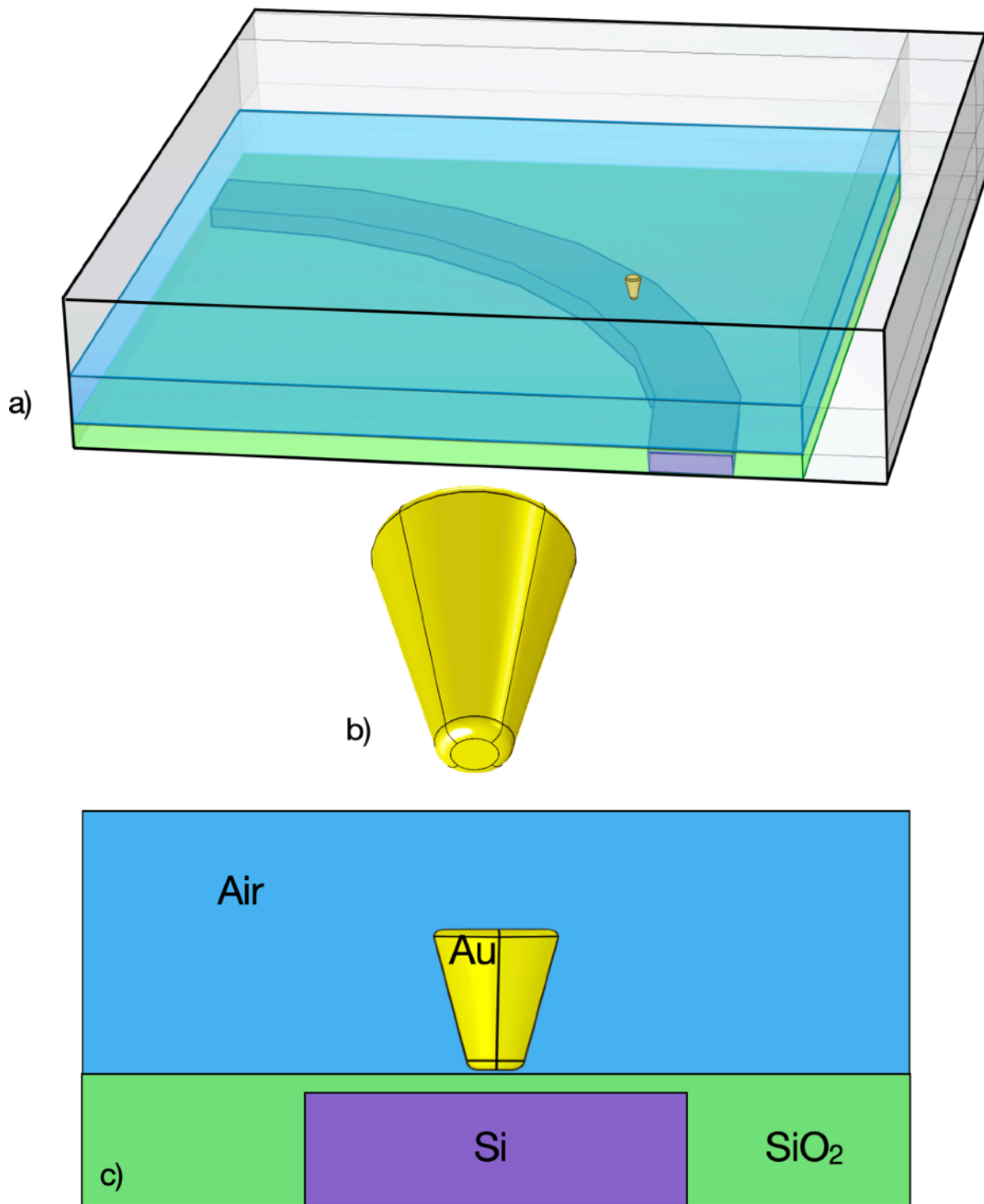
Figure 2.1 COMSOL model of Si Microring Resonator embedded in SiO$_2$ surrounded by air with Au Perturbation.
(a) 3D image of system (b) 3D image of perturbation (c) Cross sectional proportional image of the Au perturbation above the Si microring.

it is to understand generally how a metallic perturbation of similar proportions to our NSOM tip would interact with the field of a general microring resonator of a similar size and Q. As such, the ring (depicted in Figure 2.1) is modeled as a 300 nm tall and 450 nm wide rectangular Si waveguide (purple) with a ring radius of 4.5 μm (as measured from the center of the waveguide). Just like the experiment, the Si waveguide is embedded in planarized SiO_2 (green). The thickness of the SiO2 above the Si waveguide determines the z proximity of the perturbation to the microring. Air (light blue) surrounds the system.

Because of the cylindrical symmetry, the system can be reduced in size to dramatically reduce compute times. The vertical symmetry allows the ring to be split horizontally across the middle and the radial symmetry allows us to make two vertical cuts. The result is one quarter of the top half of the ring. To understand the basic properties of the ring without the perturbation, simulations can be run in this configuration.

In most other simulations, perturbations are treated spherically. However, we believe this is quite a dramatic oversimplification that greatly reduces the strength of the interaction, because of the reduction in volume as compared to the actual Au tip perturbation. After much consideration, the Au perturbation was modeled as a truncated cone with a flat bottom and rounded edges (Figure 2.1 (b)). The diameter of the bottom face is 50 nm with a 10 nm radius edge leading to the rest of the cone. The taper angle is 15 degrees and the height is 170 nm. The smoothed edges were added to help reduce the sharp edge effects that commonly plague electromagnetic simulations.

41

This Au perturbation is placed 5 nm above the top surface of the planarized SiO$_2$ layer (Figure 2.1 (c)). This small gap allows the perturbation to be surrounded by air on all sides. As was the case in the experiment, the z height of the perturbation is determined by the oxide thickness and the distance between the perturbation and the oxide remains constant.

2.9 Material definitions

For the following experiments, we chose to focus on one resonant mode in the region of 1315 nm (228 THz), and track how it is modified with the presence of a perturbation at different *x, y, z* locations. Because of this, μ and ε are defined as constants rather than a dispersion for all materials, other than the Au perturbation. (When results are discussed, it will be clear that the shifts in frequency as a function of perturbation position are nearly undetectable, so this was an appropriate simplification to make.) It is also worth noting that, although we use reported permittivities in our calculations, in practice these can vary depending on vendor and conditions. So, it is not only possible, but likely that actual values will be slightly different from the ones used in the simulation.

With that in mind, air is defined simply as $\mu = 1$ and $\varepsilon = 1$. In a similar vein, SiO$_2$ has $\mu = 1$ and $\varepsilon = 2.1025$ [26][27]. However, we need to employ a bit more care for the material definitions of Si. We define $\mu = 1$ and add a small imaginary component to the permittivity $\tilde{\varepsilon} = \varepsilon' - i\varepsilon'' = 12.3 - i0.001$ [28,29,30]. Without this imaginary component, COMSOL struggles to properly determine systematic losses, and often reports $\tilde{\omega}_m'' < 0$, implying that the

system is actually *gaining* energy rather than losing it, which is obviously

unphysical. This loss is handled by adding a finite "loss tangent, loss angle" to

the Wave Equation section of the Electromagnetic Waves, Frequency Domain

(*emw*) solver within COMSOL with the options "from material" selected for both

ε' and δ. In all other cases, the imaginary component (δ) is defined to be zero,

since the vast majority of non-perturbative losses will be cause by the Si rather

than the SiO_2 or surrounding air.

Special care must be taken with the material definitions for the Au

perturbation as well. This is because the metallic tip generates a great deal of

loss, and if not properly handled, will cause issues as described in the solvers

Section 2.7. The permeability and permittivity are defined as $\mu = 1$ but for ε a

two pole Lorentz-Drude model was used (in a similar fashion to the

QNMEig_cubesubstrate model from **MAN)** [31]. As depicted in Figure 2.2, the

poles were selected to most closely follow experimental data in the near

resonant frequency range [32]. The constants were chosen, as shown below,

from a Rakić paper [33] that models Au using a 5 pole Lorentz-Drude model fit

to permittivity data from Dold and Mecke, and Theye [34][35].

pole	ω_p (rad/s)	ω_0 (rad/s)	γ (rad/s)
1	1.1960E+16	0	8.0521E+13
2	1.3719E+15	1.2610E+15	5.2415E+14

Table 2.1 Lorentz-Drude constants for simulated Au permittivity.
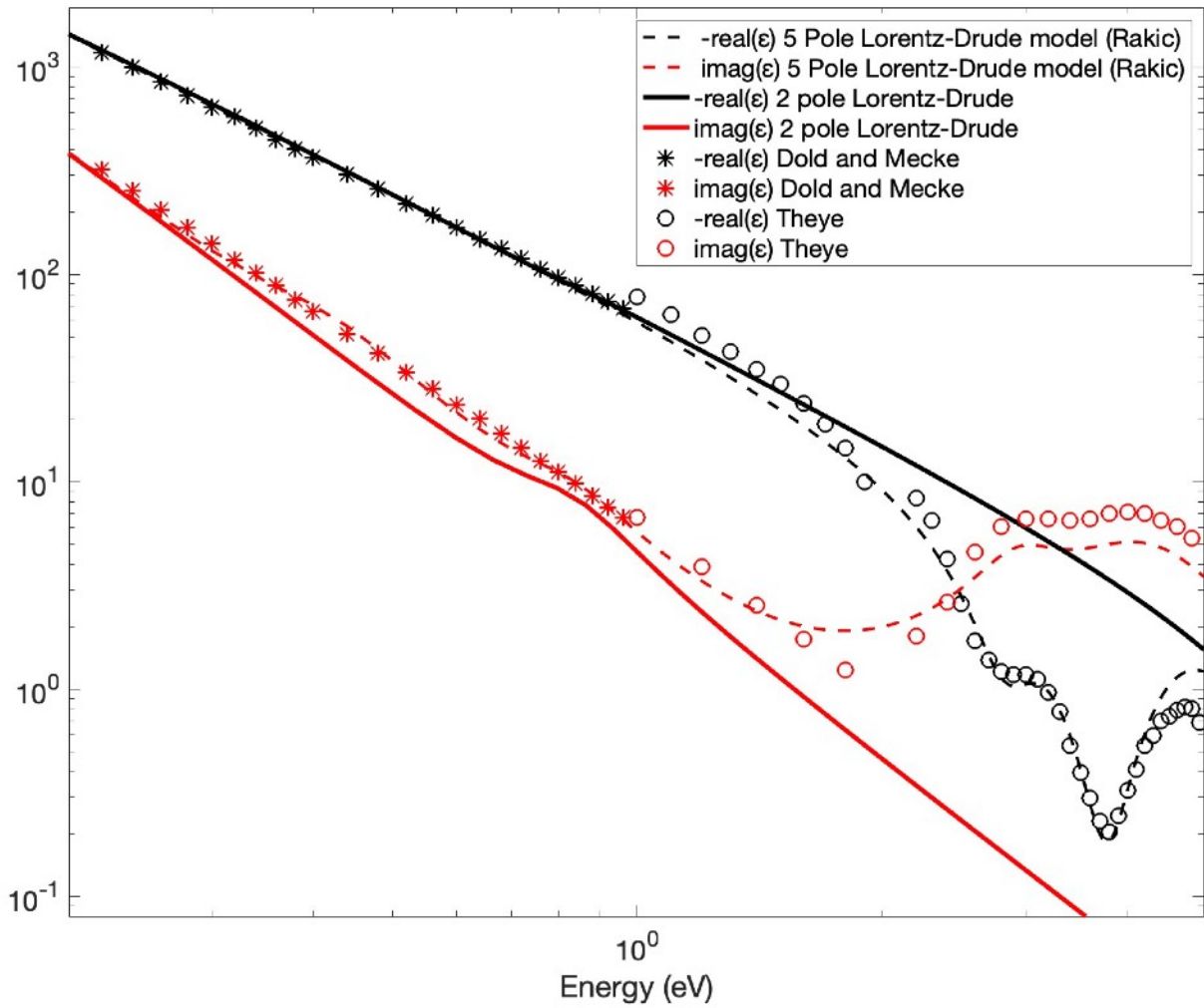
Figure 2.2 Dispersion relation between ε', ε'', and Energy.
Comparison between experimental results of experimental data from Dold and Mecke (stars)[], and Theye (circles)[], with a 5 pole Lorentz-Drude from Rakić (dashed line)[], with that used in simulations of resonances near 1 eV (solid line)

44

In the region near $\lambda = 1.3$ µm (0.947 eV or 229.5 THz), the calculated values for the epsilon will be roughly, $\tilde{\varepsilon} \simeq -69 - i5.6$.

2.10 Perfectly matched layer (PML), domain definitions, and boundary conditions

The domain and boundary conditions as well as the PML are potentially more influential to the simulation than any of the material definitions listed in the previous Section. The equations used here will ultimately determine how each region, material, and resonance is handled by COMSOL. Poor definitions here will lead to incorrect or, more likely, non-convergent results.

As shown in Figure 2.3, a 600 nm deep PML surrounds the external boundaries of the simulation. The PML serves two important functions; first, to maintain the outgoing wave (i.e. to not disrupt the resonant fields "inside" the PML) and second, to dampen the EM signal as it propagates towards the external boundary. A cartoon of this dampening is shown in Figure 2.3 (b). As was mentioned in a previous Section, unless properly handled with a dispersive PML, the fields will grow exponentially away from the resonator [36]. However, as shown in the supplemental material for Ref [25] (Section 3) although often used solely as a numerical method, when rigorously defined, PMLs can also be used to solve for analytic QNM quantities like $\tilde{V}$. For our purposes, the PML is defined in COMSOL as Cartesian. The typical wavelength is user defined to be 1200 nm.

For external boundaries beyond the PML, PEC boundary conditions, which set the tangential electric field to zero, are used. For the vertical symmetry
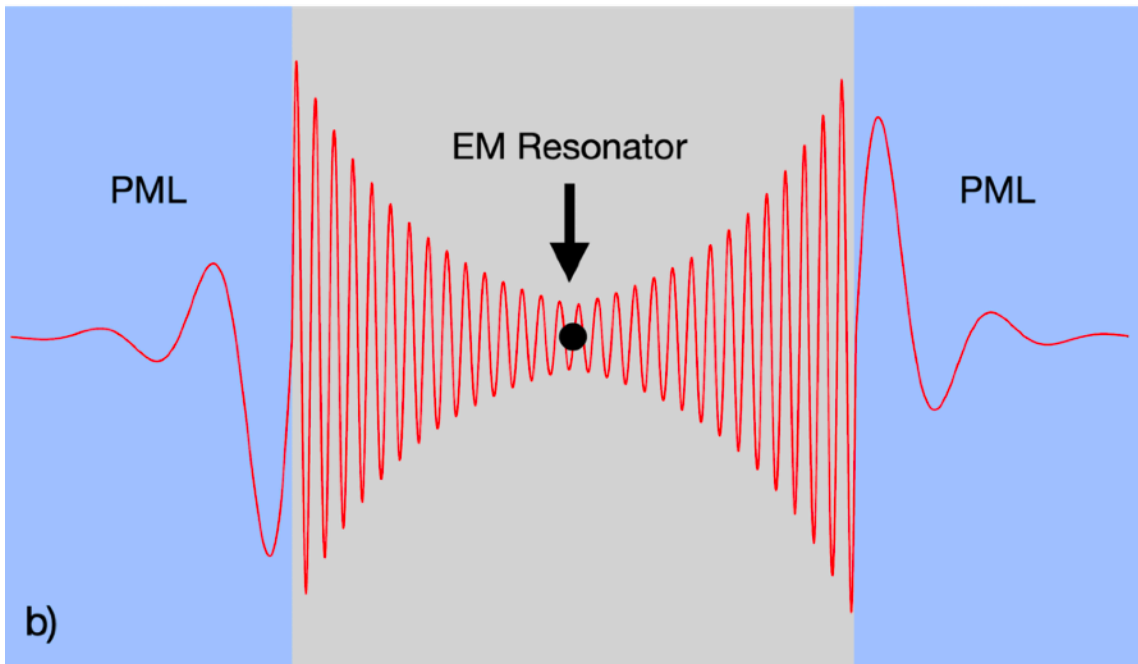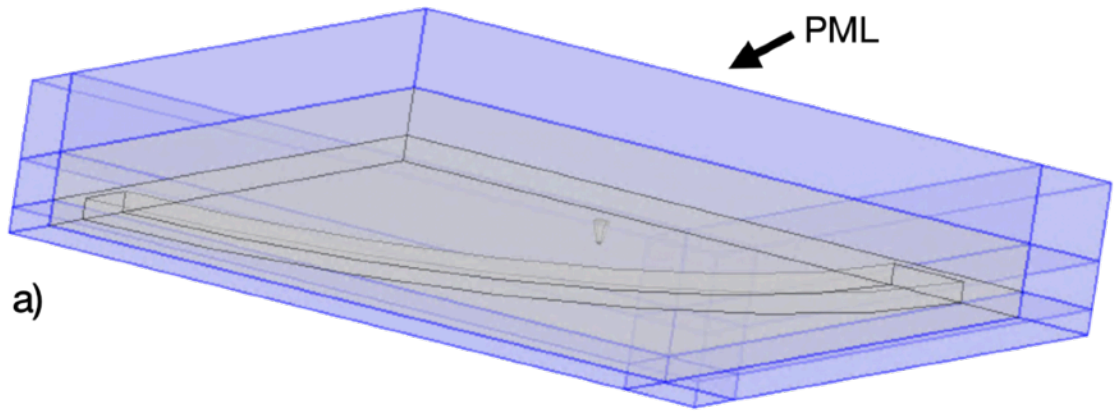
Figure 2.3 Perfectly Matched Layers (PMLs).
(a) 3D image of COMSOL model with PML colorized in blue. (b) Cartoon of PML function.

plane, a perfect magnetic conductor (PMC) boundary (the magnetic equivalent of a PEC) is used. Meanwhile, one of the radial symmetry planes is PEC with the other being PMC.

Three coupling integration operators are used in various domains within the simulation. The first, **intAll** integrates over all domains, the other two, **intMetal1** and **intMetal2** integrate over the Au domain.

As was first mentioned in Section 2.7, weak form partial differential equations (PDEs) will allow us to properly solve the linear equations from Eq. 2.14. We will once again be using **MAN** and following a similar model to the one used in QNMEig_Cubesubstrate, in which a Ag cube is modeled on an Au substrate closely resembling a 2014 paper on Purcell enhancement [37, 38]. Since there are two poles in our definition of $\tilde{\varepsilon}_{Au}$, that requires two separate weak form PDEs in the simulation. These weak form PDEs are only applied to the domains containing Au, which, in this case, is just the perturbation. The dependent variables are P1$_x$, P1$_y$, P1$_z$ for the first PDE and P2$_x$, P2$_y$, P2$_z$ for the second with:

$$\mathbf{P1} = -\frac{\omega_{p,1}^2}{\omega^2 - \omega_{0,1}^2 + i\omega\gamma_1}\mathbf{E} \qquad (2.19)$$

$$\mathbf{P2} = -\frac{\omega_{p,2}^2}{\omega^2 - \omega_{0,2}^2 + i\omega\gamma_2}\mathbf{E}. \qquad (2.20)$$

To explain how these functions are used, we need to discuss how Weak Form PDE solutions work in COMSOL. Weak Form PDEs are most often used

when there are dramatic gradients or divergent values in a solution. To get around this issue, a weak form PDE integrates over the boundary, rather than volume, of the divergent region. The domain integral of the solution variable u reads as [39]

$$c*(ux*test(ux)+uy*test(uy)+uz*test(uz))-f*test(u). \qquad (2.21)$$

There is an infinite number of solution functions u, but COMSOL is limited by computation time and therefore cannot solve for every u. Instead, COMSOL uses a Ritz-Galerkin approach to approximate the field through a superposition of a finite number of carefully selected u [40].

Looking back at Eq. 2.21, we can now see that test(ux) is really the partial derivative of u with respect to x, more generally:

$$\frac{\partial f}{\partial x} = test(fx) \qquad (2.22)$$

and the test function itself is the solution u.

With a general understanding of how Weak Form PDE's work on COMSOL, we now need to define two sets of additional local variables that relate to **P1** and **P2** in the Au domain, $DP1_x, DP1_y, DP1_z$ and $DP2_x, DP2_y, DP2_z$:

DP1x =

epsilon0_const*(emw.epsilonrxx*P1x+emw.epsilonrxy*P1y+emw.epsilonrxz*P1z),

DP1y =

epsilon0_const*(emw.epsilonryx*P1x+emw.epsilonryy*P1y+emw.epsilonryz*P1z)

DP1z =

epsilon0_const*(emw.epsilonrzx*P1x+emw.epsilonrzy*P1y+emw.epsilonrzz*P1z)

and similar for DP2$_x$, DP2$_y$, DP2$_z$. emw.epsilonyx being the yx component of the relative permittivity. These newly defined variables are used in two separate Weak Form solvers, the first being:

mu0_const*QNM_omega^2*(test(emw.Ex)*DP1x+test(emw.Ey)*DP1y+test(emw.Ez)*DP1z)*pml1.detInvT

and the second being:

mu0_const*QNM_omega^2*(test(emw.Ex)*DP2x+test(emw.Ey)*DP2y+test(emw.Ez)*DP2z))*pml1.detInvT .

There are two additional Weak Form PDEs for auxiliary fields **P1** and **P2** defined within this domain, as well. For P1$_x$, P1$_y$ and P1$_z$ we have:

1/lambda_N^2*((test(P1x)*P1x + test(P1y)*P1y + test(P1z)*P1z)*(QNM_omega^2 - j*gamma1*QNM_omega - omega01^2) / omegap1^2 + (test(P1x)*emw.Ex + test(P1y)*emw.Ey + test(P1z)*emw.Ez))

and for P2$_x$, P2$_y$ and P2$_z$:

1/lambda_N^2*((test(P2x)*P2x + test(P2y)*P2y + test(P2z)*P2z)*(QNM_omega^2 - j*gamma2*QNM_omega - omega02^2) / omegap2^2 + (test(P2x)*emw.Ex + test(P2y)*emw.Ey + test(P2z)*emw.Ez)).

With this, the domains have now been properly defined and we can move one step closer to running the simulation.

2.11 Mesh size

The mesh is what determines the "finite element " aspect of FDTD and FDFD. The mesh consists of sub-domains within each material domain where

49

Maxwell's equations are solved. Rather than determine each of these individually, COMSOL determines the mesh based on a few parameters input by the user.

Free tetrahedral mesh was used for the the Si, SiO$_2$, air and Au perturbation. For the simulations in all following Sections, a maximum element size of 300 nm was used for the air and SiO$_2$ with a maximum of 220 nm for the Si. To see how the mesh size affects both modeling and results, a study was conducted where the Au perturbation is scanned starting toward the center of the ring, and ending at the center of the waveguide at varying maximum Si mesh sizes. In panels (a-d) of Figure 2.4 two distinct partitions of the Si ring domain can be seen, with either 280 nm or 100 nm maximum mesh size selected. As one would expect the larger mesh is much more coarse with fewer cells. The smaller mesh is more refined albeit the increased number of cells will increase the compute time as well.

In Figure 2.4 (e) and (f) we can see the effect that this change has on both the real and imaginary frequencies computed by COMSOL, ω' and ω''. Though we will dig deeper into understanding the implications of these results in Section 2.12, it's worth empirically comparing the results to see if the different mesh sizes significantly affect either of these results. The result is that changing to a more refined mesh slightly decreases the resonant wavelength for mesh sizes below 220 nm, with a change from about 229.5 THz (1.306 µm) to about 229.1 THz (1.309 µm). Despite this slight change in resonant wavelength, all four simulated mesh sizes behave the same and remain relatively unchanged as the
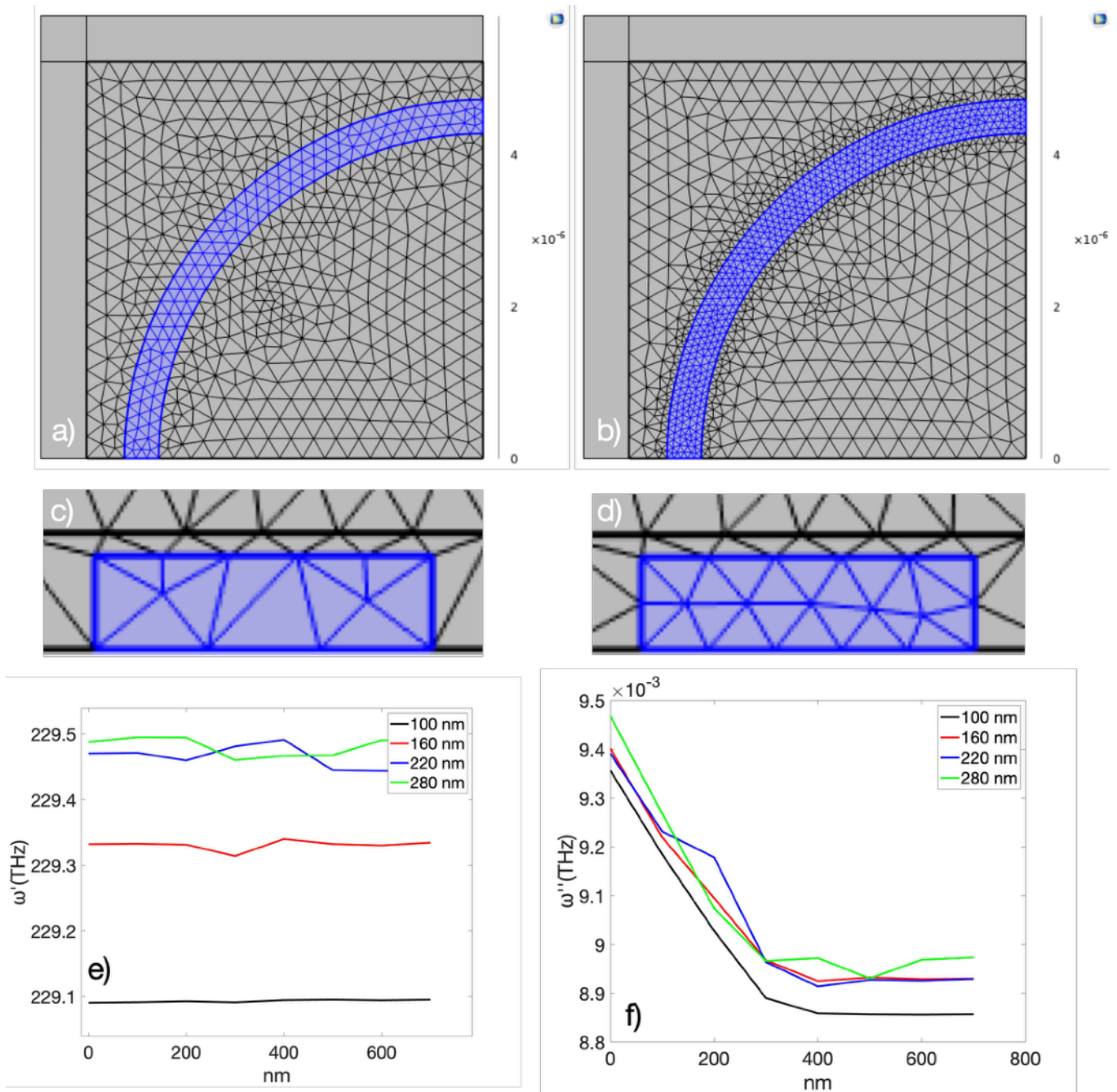
Figure 2.4 Si waveguide mesh size comparison.
3D rendering of mesh with (a,b) 280 nm and (b,d) 100 nm maximum element sizes. (c)
Simulated ω' and (b) ω'' as a function of distance from center of waveguide with minimum element size denoting the differently colored plot lines.

Au tip position changes. It is a similar story for ω'' which decreases by about 1%

(from 8.95E-3 THz to 8.85E-3 THz) for tip locations > 400 nm from the center of

the waveguide, as the mesh size decreases from 280 nm to 100 nm. However,

the general trend that sees losses decrease at a constant rate as the tip move

away from the center of the waveguide, and then levels off to a constant value

400 nm from the waveguide center, remains the same for all mesh sizes. Thus,

changing the mesh size of the ring seems to have no affect on the physics of the

tip-sample interaction, which is what we would hope.

Because of its size and shape, rather than being limited by the maximum

element size, the Au tip is limited by the minimum size, which was set to 16.5

nm for the experiments in the following Sections. It is important for us to also

test how changing the mesh size on the Au tip will affect the simulations. The

same simulations that were just described for the Si mesh change were also

conducted for Au tip minimum mesh sizes from 20 nm down to 2 nm. The

results are depicted in Figure 2.5. When comparing the 20 nm to the 2 nm

minimum element sizes, the center of the Au perturbation appears very similar,

however, these meshes diverge dramatically at the rounded edges. Because of

the much smaller element size, the 2 nm mesh can create much more of a

smooth contour on the bottom and top edges, whereas only 3 mesh elements

make up the curves on the 20 nm mesh. Since field intensity increases

dramatically around sharp edges, it is not unreasonable to suspect that a

change like this could have a dramatic effect on the results of the simulation.
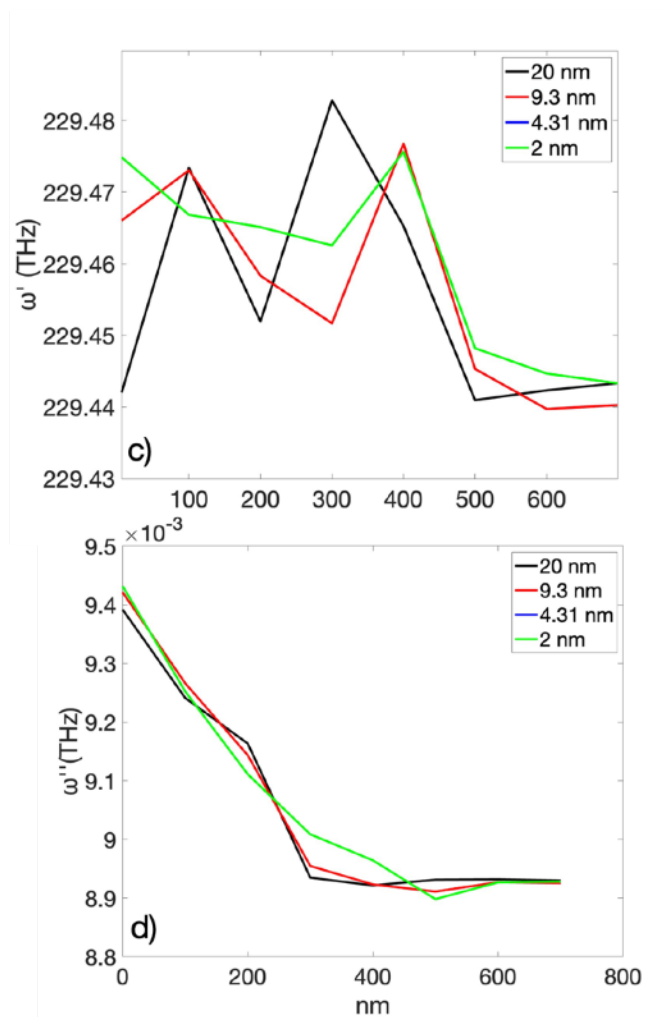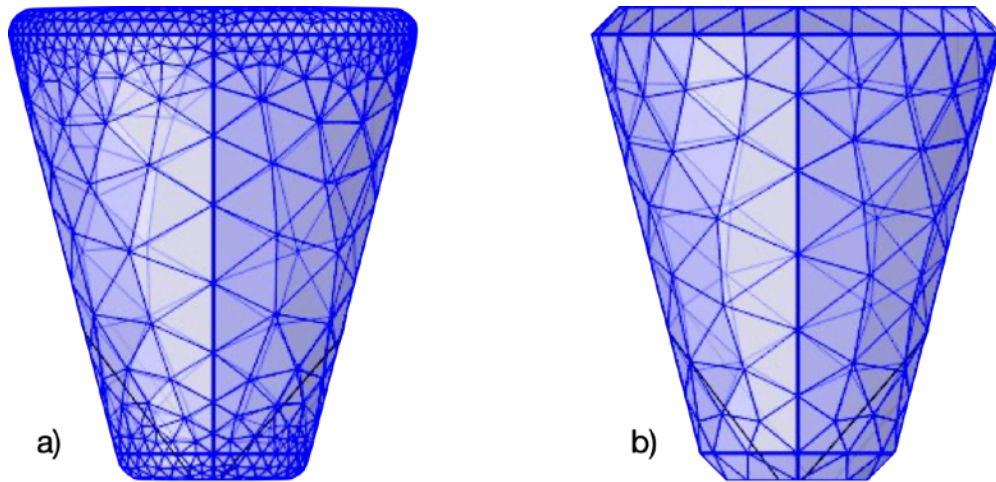
Figure 2.5 Au perturbation mesh size comparison.
3D rendering of mesh with (a) 2 nm and (b) 20 nm minimum element sizes. (c)

Simulated ω' and (b) ω'' as a function of distance from center of waveguide with minimum element size denoting the differently colored plot lines. Note: the data for the blue and green curves were nearly (but not perfectly in agreement) which is why it cannot be seen on the plot.

Fortunately, when looking at the results in panels (c) and (d) of Figure 2.5 it is clear that this is not the case. As the minimum element size decreases, there is no noticeable change in the resonant frequency. Similarly, as the tip scans away from the waveguide, the values all remain relatively constant at around 229.46 THz (1.3065 μm) with some small (0.02 THz, 0.1 nm) fluctuations. There is no discernible mesh-related difference for the ω'' values far from the waveguide either. As the perturbation moves away from the center of the waveguide, all mesh sizes follow the same general trend, with roughly the same values.

From these two studies, we can conclude that changing the mesh of the the Si waveguide will very slightly modify the calculated $\tilde{\omega}$, as one might expect since the geometry of the ring is what determines the resonant mode. However, this modification does not change the interaction between the field generated by the Si ring and Au perturbation. Changing the Au perturbation has no affect on either the calculated $\tilde{\omega}$ or the interaction between the field generated by the Si ring and Au perturbation. Therefore, we can be confident that our choices of 220 nm for the Si mesh and 16.5 nm for the Au mesh will not affect the conclusions we draw from the simulations in the following Sections.

For the PML domains a swept mesh (which extrudes the surface mesh throughout the domain to minimize compute time) is used [41].

2.12 Simulating NSOM scans at varying oxide thicknesses

The first study we conduct will examine how our choice of oxide thickness affects the interaction between the resonant field and the Au
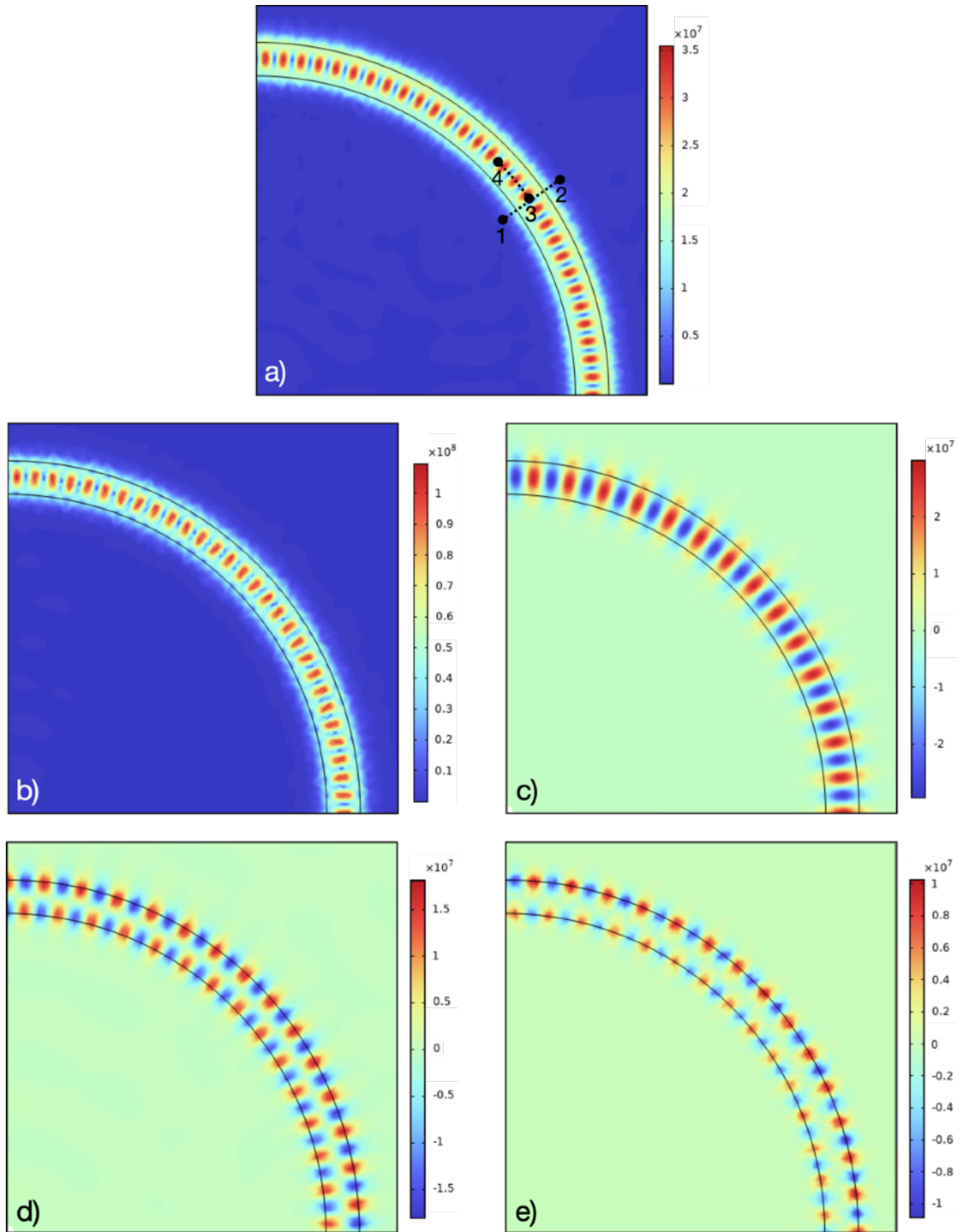
Figure 2.6 Simulated fields of microring resonator with 30nm thick oxide layer.
(a) normE at the center of the ring. Points 1 to 2 depict the tip path for Figure 2.9 (a). Points 3 to 4 depict the tip path for Figure 2.9 (b) normE, (c) E perpendicular to propagation sin(atan(x/y))*E_x + cos(atan(x/y))*E_y, (d) E parallel to propagation cos(atan(x/y))*E_x - sin(atan(x/y))*E_y, (e) E_z calculated on the top surface of the oxide layer (30 nm above the top of the Si waveguide)

perturbation. To study this, we must first look at the field and $\tilde{\omega}$ of an

unperturbed ring. Figure 2.6 depicts the fields generated for the system with a

30 nm SiO$_2$ layer. $\omega' = 229.44$ THz (1.3066 μm) and $\omega'' = 8.9328$E-3 THz yielding

Q = 12,842.8. There are 118 total E-field intensity peaks along the ring, which,

with a radius of 4.5 μm, yields a wavelength of 479.225 nm and an effective

index $n_{eff} = 2.726$. Importantly, panels (b) and (a) depict the field intensity (V/m)

at the center of the waveguide, and at the top SiO$_2$ surface, respectively.

Although the intensity diminishes at the SiO$_2$ air interface, the field profile

appears nearly identical. This is an important feature, as this is the portion of the

field that the Au tip will be interacting with during the simulated NSOM scans. If

the field was near zero or distinctly different on this surface, it would throw the

results of the NSOM scan into question. Components of the electric field taken

from the top SiO$_2$ surface can be seen in panels (c), (d) and (e).

To test the affect of Au tip proximity, a parametric sweep is conducted

where the Au tip is "scanned" across the waveguide from point 1 to point 2 on

Figure 2.6 (a). The tip moves radially at a constant 36 degree angle when viewed

in the xy plane from -700 nm to +700 nm, with zero being the center of the

waveguide (as opposed to the center of the ring). A new simulation is computed

for each 25 nm interval. This scan is conducted at 3 tip heights above the Si

ring: 20, 35 and 50 nm. Since the tip is located 5 nm above the oxide layer,

these equate to t = 15, 30, and 45 nm.

To understand generally how the tip-field interaction behaves, let's first

look at a side profile of the electric field norm (V/m) as the tip scans across the
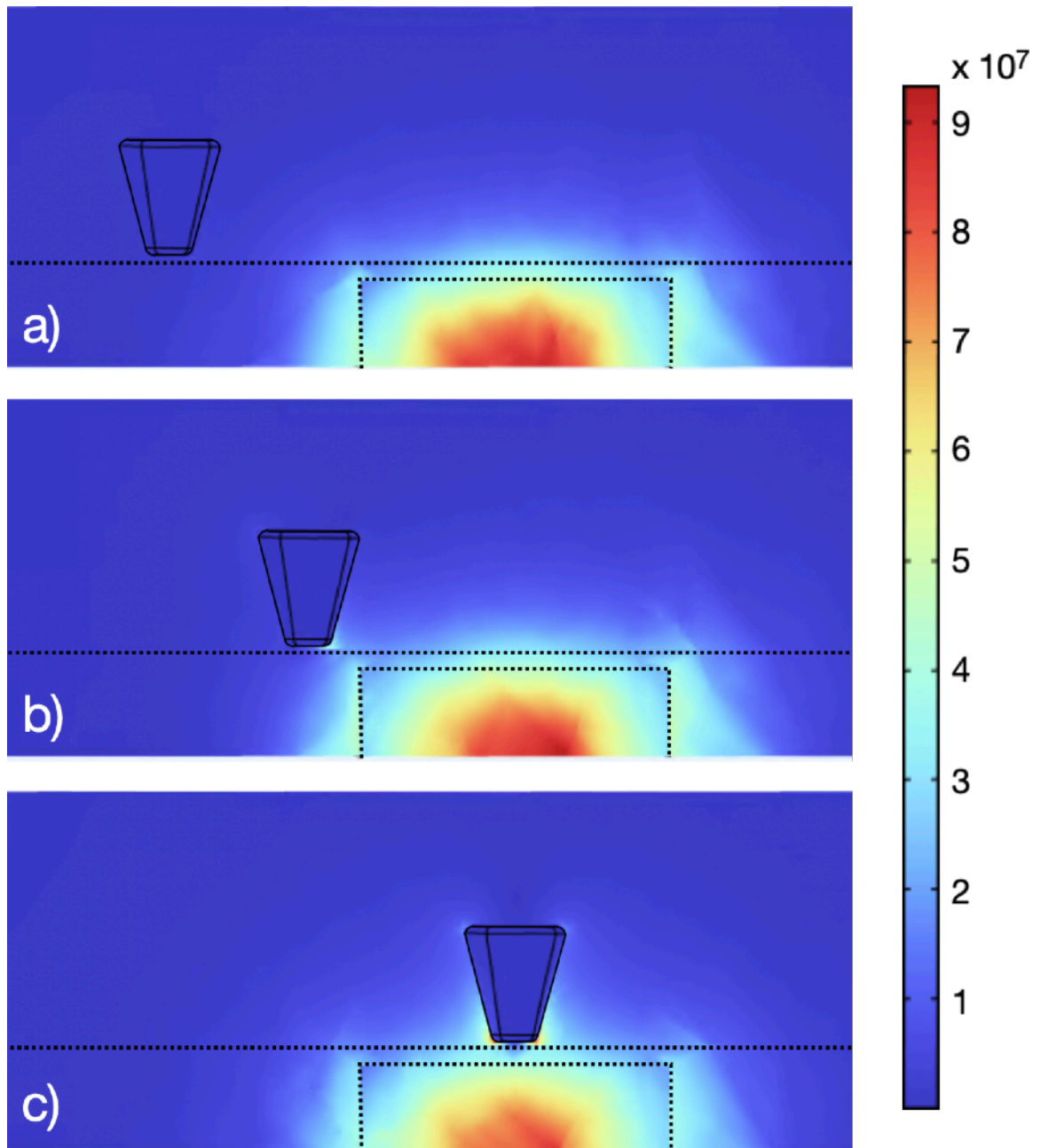
Figure 2.7 Cross sectional view of simulated Electric field norm as a function of NSOM tip position.
(a) Au tip 500 nm (b) 300nm (c) and at the microring waveguide center with a z height of 35 nm above the waveguide. (Locations -500 nm, -300 nm and 0 respectively in Figure 2.9 Dotted lines depict boundaries of the Si waveguide and oxide layer.

waveguide (Figure 2.7). With the tip 500 nm away from the center of the

waveguide (-500 nm on Figure 2.9), the field within the waveguide appears

unperturbed and there is no field intensity worth noting at the tip. At this point, it

appears that the is no real interaction between the tip and the resonant field.

When the tip moves to 300 nm from the waveguide center and 75 nm from the

edge in panel (b) (-300 nm on Figure 2.9), the field profile within the waveguide

still appears ostensibly similar to that in panel (a). However, the intensity has

been slightly diminished. At this point, a small amount of field can also be seen

at the very tip of the Au perturbation. At this location, the tip and the field are

now interacting and a small amount of energy is coupling from within the

waveguide to the tip; however, the mode profile remains the same. When the tip

moves to be directly over the center of the waveguide (0 nm on Figure 2.9) the

mode profile still appears as it did in the previous two panels, however the

intensity is even further reduced. The field intensity at the tip increases beyond

what was seen in panel (b). At this location, the tip-sample interaction is further

increased with a larger portion of the local field being located at the tip rather

than within the waveguide.

Now that we have a general understanding of how the Au tip interacts

with the field locally, lets look at an *x-y* cross section to see how it affects the

ring globally. Figure 2.8 depicts the electric field norm (in COMSOL normE =

sqrt(realdot(Ex,Ex)+realdot(Ey,Ey)+realdot(Ez,Ez)) at the SiO_2-air interface as the

tip is scanned from -500 nm to 0. As was the case in panel (a) of Figure 2.7 with

the tip 500 nm from the waveguide, the mode appears identical to the
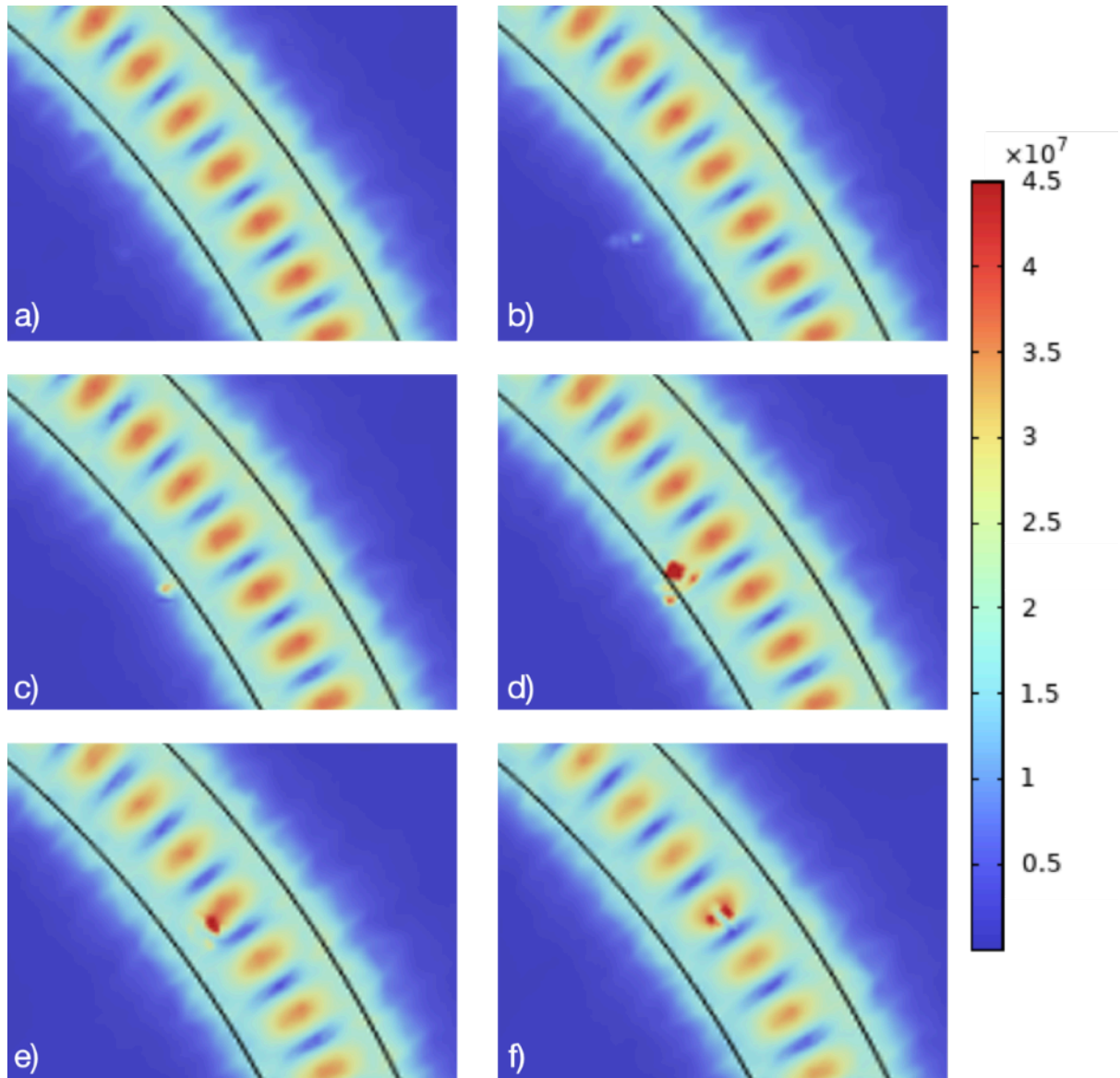
Figure 2.8 Simulated normE of microring resonator with 30nm thick oxide layer at varying Au perturbation positions.
(a) 500 nm (b) 400 nm (c) 300 nm (d) 200 nm (e) 100 nm from center and (f) at center. Field is measured at oxide layer-air interface (30 nm above Si waveguide and 5nm below tip)

unperturbed simulation and there is no field visible at the location of the tip. As the tip moves closer to the ring, panels (b) and (c), we can begin to see the intensity at the tip increasing, but the resonant mode of the ring still appears relatively unchanged. However, once the the tip is over the waveguide and 200 nm from the center (panel (d)), the intensity at the tip dramatically increases and we can begin to visibly see a decrease of field intensity throughout the entire ring, not just in the location of the perturbation. As the tip moves towards the center (panels (e), (f)), the intensity of the tip continues to increase (this is beyond the scale on the right which is why it is not evident from the images) and the energy contained within the waveguide continues to decrease. We can conclude that this interaction is not solely a local effect as seen in Figure 2.7, but a global affect that decreases the intensity throughout the entire ring as the tip interacts with stronger fields.

To explore the effect of this tip-sample interaction quantitatively, lets investigate how the calculated $\tilde{\omega}$ is affected by the presence of the tip, and how that changes for varying tip-sample interaction distances. The dashed lines in Figure 2.9 (a) depict how the resonant frequency changes in the absence of the Au perturbation at the three oxide thicknesses mentioned previously, whereas the solid curves depict this calculated value at a given radial position of the Au perturbation. The dashed lines indicate that as the oxide is thinned, ω' slightly increases from roughly 229.2 THz (1.308 µm) to about 229.8 THz (1.3046 µm). All three solid curves depict the same general behavior. When the tip is more than 500 nm from the center on either side, the calculated ω' is nearly identical to the

60
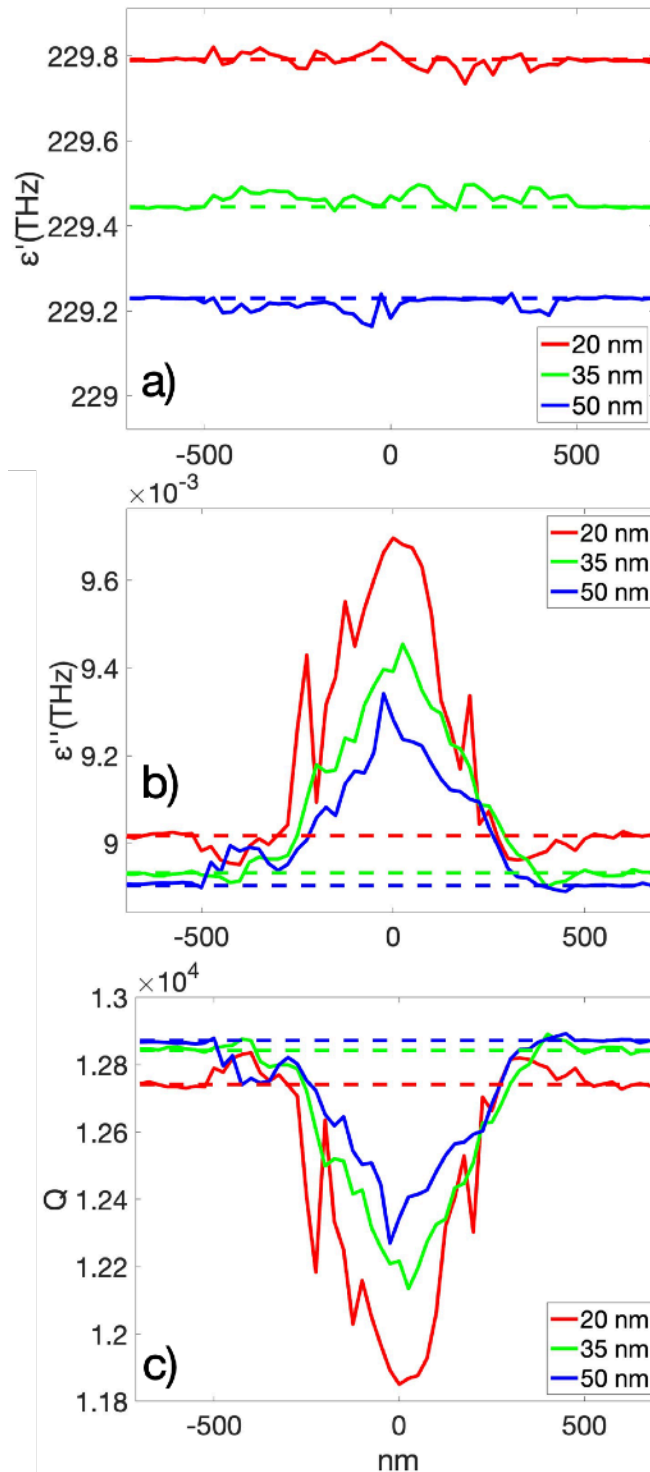
Figure 2.9 Simulated ω', ω'' and Q as a function of Au tip position and oxide thickness (Across Ring).
Each data point represents a simulation at a given tip position as the perturbation scans along the dotted line in Figure 2.6 (a) from point 1 to point 2, with zero being the center of the waveguide. (a) ω' (b) ω'' and (c) Q vs radial position of perturbation.

value calculated without the perturbation present. As the tip moves within 500 nm of the center, ω' begins to very slightly fluctuate around the calculated value, albeit with no obvious pattern. The fluctuations appear to be of the same relative magnitude, irrespective of t.

Without a perturbation present, ω'' slightly increases as t decreases, since a larger portion of the mode propagates though air. Once again, the behavior of ω'' with respect to tip position follows the same general pattern regardless of t. When the perturbation is more than 500 nm from the waveguide center, ω'' is nearly identical to the value computed without a Au perturbation. However, as the Au tip moves from left to right within 500 nm, ω'' increases until reaching a maximum near the center of the waveguide. As the tip moves away from the center, ω'' decreases until once again returning to the unperturbed value. Although this peak is near zero, it is actually slightly > 0, or to towards the outside of the ring waveguide, just as the peak calculated normE appears, slightly towards the outside in Figure 2.8. Unlike the plot for ω', there is an increase in $\Delta\omega''$ as the z height of the tip decreases. Interestingly, on both sides of the 20 nm scan and on the positive side of the other two, just inside of 500 nm from the waveguide the value of ω'' is actually less than the calculated unperturbed value. This isn't an artifact or an error, and is actually predicted by Ref. [14]. In this region, instead of scattering light, the perturbation is actually reflecting radiated light *back* to the waveguide which decreases the loss and increases Q.
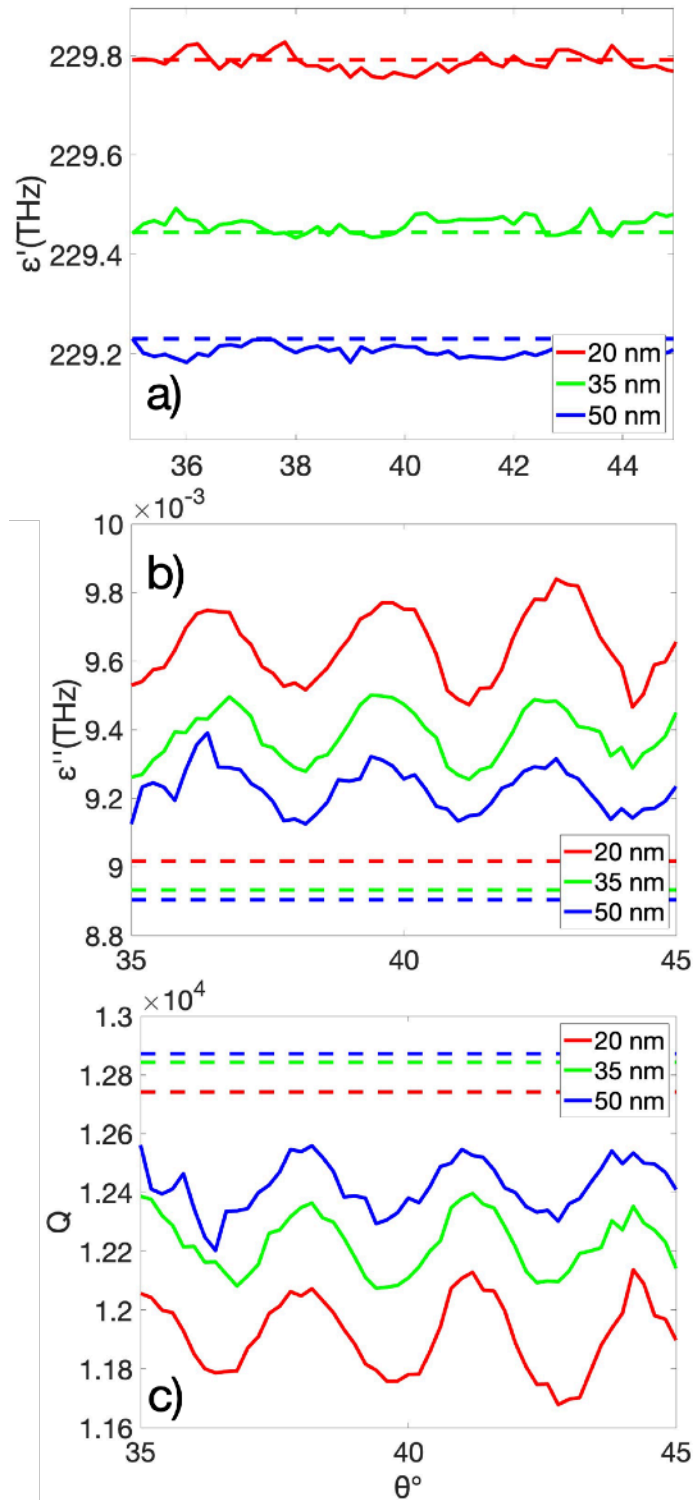
Figure 2.10 Simulated ω', ω'' and Q as a function of Au tip position and oxide thickness (Along center of ring waveguide).
Each data point represents a simulation at a given tip position as the perturbation scans along the dotted line in Figure 2.6 (a) from point 3 to point 4 (a) ω' (b) ω'' and (c) Q vs angular position of perturbation.

With Q being computed by $\dfrac{\omega'}{2 \cdot \omega''}$ and ω' being ostensibly constant, Q

follows the inverse of what was described in the previous paragraph.

One additional study is conducted which is nearly identical to the one just described, except the path was changed from points 1-2 to points 3-4 in Figure 2.6. Points 3 and 4 are located at the center of the waveguide at radial locations 35 and 45 degrees, respectively.

Panel (a) of Figure 2.10, in which ω' is plotted vs θ (the radial angle with x = y = 0 being the origin), appears nearly identically to how it was in Figure 2.9, with values oscillating very slightly without any clear pattern from the unperturbed value. Even when scanning above the center of the ring where there is a periodic electric field, the fluctuations still fail to display any pattern or periodicity. Unlike panel (b) in Figure 2.9, ω'' never approaches the unperturbed value, instead, it oscillates in a periodic manner with the minimum value being significantly larger than the unperturbed ω''. The magnitude of this $\Delta\omega''$ increases as t decreases. The period of oscillation is the same for all three simulated t values and is roughly 6.2 ± 0.2 degrees or a 25 ± 20 nm arc-length. This would imply a full period of 500 ± 40 nm, which is in agreement with the calculated wavelength of 481 nm. Once again, with ω' being nearly constant, Q follows the inverse of what was just discussed for ω''.

From these studies we can arrive at main five results.

1. There is no evidence of ω' modification as a result of tip-sample interaction. In both studies, values of ω' simply fluctuated with very minor random deviations from the unperturbed value.

2. When the Au tip is far from the waveguide (> 500 nm), there is no modification to $\tilde{\omega}$, i.e. the simulation behaves as if the perturbation does not exist.

3. Aside from a few very specific locations, the overwhelming result of the tip-sample interaction is an increase of ω'' when the tip is within 500 nm of the waveguide.

4. The strength of the tip-sample interaction and therefore the increase of ω'' is a function of the strength of the local electric field. i.e. ω'' is larger in areas of larger field.

5. With ω' being ostensibly constant the Q modification as a result of the tip-sample interaction is simply the inverse of $\Delta\omega''$.

2.13 Simulating a complete NSOM scan

With the tip-sample interaction now understood we can simulate an entire NSOM scan. For this scan, t = 30 and the tip will scan both radially from -500 nm to +500 nm with a step size of 25 nm (using the same definition from the previous Section) and along the arc of the ring, starting at 35 degrees and going to 45 degrees with a step size of 0.25 degrees. In total, this simulated scan requires 1681 individual simulations (which ran over the course of two days). The unperturbed electric field norm can be seen in panel (a) of Figure 2.11. The area that the scan sweeps across is shown in the inset. There are three peaks in
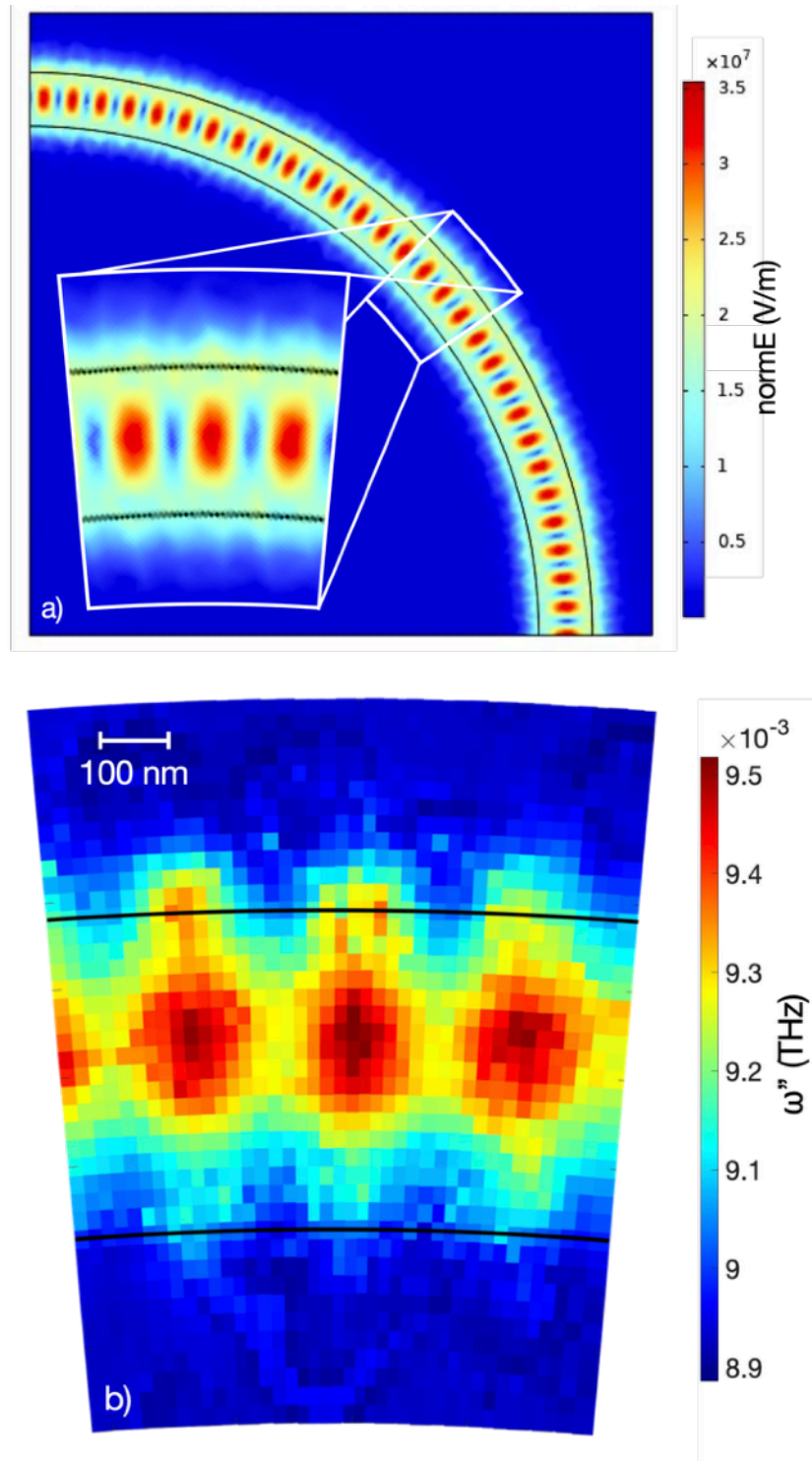
Figure 2.11 Comparison of simulated NSOM measurement losses to simulated electric field intensity.
(a) Simulated electric field norm taken from the plane at the top surface of the oxide layer (30 nm above Si waveguide 5 nm below where the tip would be) (inset) Area in which the NSOM "scan" will be conducted (b) Simulated ε" as a function of NSOM tip position. (each pixel represents a simulation with the tip at that location)

the electric field norm in the scanned region. The maxima don't appear to be exactly at the center of the waveguide, instead they are a bit closer to the outside of the ring. The results of the scan are depicted in panel (b), where ω'' is plotted vs *xy* position. Each pixel represents the imaginary component of the eigenfrequency for an individual simulation. There are three tip-induced loss peaks, which appear periodically, just outside of the centerline of the ring waveguide. There is a strong correlation, between locations with higher field intensity and larger tip-induced losses. One slight difference, however, appears where in the middle of the waveguide, where the field goes to zero in panel (a), but the tip still induces losses in panel (b). The reason for this, is that the tip is not infinitely thin, and, although it only has a 50 nm diameter nearest to the ring, as *z* increases, so does the diameter of the perturbation. This increased size decreases the resolution of the scan and explains why these minima go to zero on the simulation but don't go to the unperturbed value on the NSOM scan.

2.14 Conclusion

In this Chapter, we have introduced the concept of quasi-normal modes (QNMs) which, unlike a large body of the work preceding this thesis, do *not* approximate high Q electromagnetic resonators as lossless. Following the work of Lalanne and the **MAN** software package, we designed simulations in COMSOL which utilized not only an eigenmode solver, but also two weak form PDE solvers to find a QNM in a Si microring resonator embedded in a thin layer of SiO_2 with air as the background. We then simulated how a small Au tip, designed to be a similar size and shape to an aperture-less NSOM tip, would

perturb this system. By scanning this perturber at different heights and *x-y* locations, we found that there was no evidence of resonant frequency modification for this NSOM configuration. There is, however, evidence of tip-induced losses. The losses increase when the tip is at locations of higher electric field intensity. This result directly contradicts prior work on cavity perturbation theory in which the resonators were approximated to be lossless. We determined that the NSOM tip scatters more energy in areas of higher electric field. This scattering decreases the Q and reduces the field intensity within the resonator. Using this new understanding of the tip-field interaction a simulated NSOM was conducted, where the near-field just above the SiO_2 surface was mapped by plotting ω'' as a function of tip position. There was strong agreement between $\Delta\omega''$ and the electric field intensity, implying that tip induced losses can map electric field intensity. We can extrapolate these results, to conclude that world NSOM scan which measures $\Delta\omega''$ (or a quantity related to ω'') as a function of NSOM tip position, would properly map of the local electric field intensity.

[1] D.H. Choi and W.J.R. Hoefer, "The Finite-Difference-Time-Domain Method and its Application to Eigenvalue Problems," *IEEE Transactions on Microwave Theory and Techniques* **34**(12), 1464-1470 (1986) DOI: 10.1109/TMTT.1986.1133564

[2] F. Xu,Y. Zhang and W. Hong, "Finite-Difference Frequency-Domain Algoirthm for Modeling Guided-Wave Properties of Substrate Integrated Waveguide," *IEEE Transactions on Microwave Theory and Techniques* **51**(11), 2221-2227 (2003) DOI: 10.1109/TMTT.2003.818935

[3] P. Lalanne, W. Yan, K. Vynck, C. Sauvan, and J.P. Hugonin, "Light Interaction with Photonic and Plasmonic Resonances," *Laser Photonics Rev.* **12**, 1700113 (2018) DOI: 10.1002/lpor.201700113

[4] H. A. Bethe and J. Schwinger, "Perturbation theory for cavities," N.D.R.C. Rpt. D1-117 Cornell University, (1943).

[5] A.F. Koenderink, M. Kafesaki, B.C. Buchler, V. Sandoghdar, "Controlling the Resonance of a photonic Crystal Microcavity by a Near-Field Probe," *Phys. Rev. Lett.* **95**, 153904 (2005) doi: 10.1103/PhysRevLett.95.153904

[6] S. Mujumdar, A.F. Koenderink, T. Sünner, B.C. Buchler, M. Kamp, A. Forchel and V. Sandoghdar, "Near-field imaging and frequency tuning of a high-Q photonic crystal membrane microcavity," *Opt. Express* **15**, 17214-17220 (2007) doi: 10.1364/OE.15.017214

[7] F. Intonti, S. Vignolini, F. Riboli, A. Vinattieri, D.S. Wiersma, M. Colocci, L. Balet, C. Monat, C. Zinoni, L.H. Li, R. Houdré, M. Francardi, A. Gerardino, A. Fiore, and M.Gurioli, "Spectral tuning and near-field imaging of photonic crystal microcavities," *Phys. Rev. B* **78**, 041401(R) (2008) doi: 10.1103/PhysRevB.78.041401

[8] S. Vignolini, F. Intonti, F. Riboli, A. Vinattieri, L. Balet, L.H. Li, M. Francardi, A. Gerardino, A. Fiore, D.S. Wiersma, and M.Gurioli, "Magnetic Imaging in Photonic Crystal Microcavities," *Phys. Rev. Lett.* **105**, 123902 (2010) doi: 10.1103/PhysRevLett.105.123902

[9] C. Sauvan, J.P. Hugonin, I.S. Maksymov, and P. Lalanne, "Theory of the Spontaneous Optical Emission of Nanosize Photonic and Plasmon Resonators," *Phys. Rev. Lett.* **110**, 237401 (2013) doi: 10.1103/PhysRevLett.110.237401

[10] T. Wu, M. Gurioli, and P. Lalanne, "Nanoscale Light Confinement: the Q's and V's," *ACS Photonics* **8**, 1522-1538 (2021) doi: 10.1021/acsphotonics.1c00336

[11] C. Sauvan, J.P. Hugonin, I.S. Maksymov, and P. Lalanne, "Supplementary Material, section 2: Theory of the Spontaneous Optical Emission of Nanosize Photonic and Plasmon Resonators," *Phys. Rev. Lett.* **110**, 237401 (2013) doi: 10.1103/PhysRevLett.110.237401

[12] J. Yang, H. Giessen and P. Lalanne, "Simple Analytical Expression for the Peak-Frequency Shifts of Plasmonic Resonances for Sensing," *Nano Lett.* **15**, 3439-3444 (2015) doi: 10.1021/acs.nanolett.5b00771

[13] T. Weiss, M. Mesch, M. Schäferling, H. Giessen, W. Langbein, and E.A. Muljarov, "From dark to bright: first-order perturbation theory with analytical mode normalization for plasmonic nanoantenna arrays applied to refractive index sensing," *Phys. Rev. Lett.* **116**, 237401 (2016) doi: 10.1103/PhysRevLett.116.237401

[14] K.G Cognée, W. Yan, F. La China, D. Balestri, F. Intonti, M. Gurioli, A.F. Koenderink, and P. Lalanne, "Mapping complex mode volumes with cavity perturbation theory," *Optica* **6** (3) 269-273 (2019) doi: 10.1364/Optica.6.000269

[15] T. Wu, D. Arrivault, W. Yan, and P. Lalanne, "Modal analysis of electromagnetic resonators: user guide for the MAN program," arxiv.org, 8 March 2024, https://arxiv.org/pdf/2206.13886.pdf

[16] software: https://github.com/Light-in-complex-nanostructures/MAN/tree/master

[17] https://www.comsol.com

[18] https://www.3ds.com/products/simulia/cst-studio-suite

[19] Q. Bai, M. Perrin, J-P Hugonin, and P. Lalanne, "Efficient and intuitive method for the analysis of light scattering by a resonant nanostructure," *Opt. Exp.* **21** (22) 27371-27382 (2013) doi: 10.1364/OE.21.027371

[20] "Optical Ring Resonator Notch Filter 3D" comsol.com (8 March 2024) www.comsol.com/model/optical-ring-resonator-notch-filter-3d-73821

[21] https://www.3ds.com/products/simulia/cst-studio-suite

[22] P. Drude, "Zur Elektronentheorie der Metalle," *Ann. der Phys.* **306** (3) 566-613 (1900) doi: 10.1002/andp.19003060312

[23] P. Drude, "Zur Elektronentheorie der Metalle; II. Teil. Galvanomagnetische und thermomagnetische Effecte," *Ann. der Phys.* **308** (11) 369-402 (1900) doi: 10.1002/andp.19003081102

[24] H.A. Lorentz, (1909). "The theory of electrons and its applications to the phenomena of light and radiant heat. Vol. Bd. XXIX," New York; Leipzig

[25] W. Yan, R. Faggiani, and P. Lalanne, "Rigorous modal analysis of plasmonic nanoresonators," *Phys. Rev. B.* **97** 205422 (2018) doi: 10.1103/PhysRevB.97.205422

[26] M.N. Polyanskiy, "Refractiveindex.info database of optical constants," *Sci. Data* **11**, 94 (2024) doi: 10.1038/s41597-023-02898-2

[27] I.H. Malitson, "Interspecimen Comparison of the Refractive Index of Fused Silica," *J. Opt. Soc. Am.* **55** (10) 1205-1209 (1965) doi: 10.1364/JOSA.55.001205

[28] C.D. Salzberg and J.J. Villa. Infrared "Refractive Indexes of Silicon, Germanium and Modified Selenium Glass," *J. Opt. Soc. Am.*, **47**, 244-246 (1957)

[29] B. Tatian, "Fitting refractive-index data with the Sellmeier dispersion formula," *Appl. Opt.* **23**, 4477-4485 (1984)

[30] H.H. Li. "Refractive index of silicon and germanium and its wavelength and temperature derivatives," *J. Phys. Chem. Ref. Data* **9**, 561-658 (1993)

[31] T. Wu, D. Arrivault, W. Yan, and P. Lalanne, "Modal analysis of electromagnetic resonators: User guide for the MAN program," Mendeley Data, V1, doi: 10.17632/wdz5pd4sb4.1

[32] P.B Johnson and R.W. Christy, "Optical constants of the noble metals," *Phys. Rev. B.* **55** 43704379–1209 (1972) doi: 10.1103/PhysRevB.6.4370

[33] A.D. Rakić, A.B. Djurišić, J.M. Elazar, and M.L Majewski "Optical properties of metallic filmsfor vertical-cavity optoelectronic devices," *Applied. Opt.* **37** (22) 5271–5283 (1998) doi: 10.1364/AO.37.005271

[34] B. Dold and R. Mecke, "Optische Eigenschaften von Edelmet- allen, Übergangsmetallen und deren Legierungen im Infrarot (1. Teil)," *Optik* **22,** 435– 446 (1965)

[35] M. L. Thèye, "Investigation of the optical properties of Au by means of thin semitransparent films," *Phys. Rev. B* **2,** 3060 - 3078 (1970) doi: 10.1103/PhysRevB.2.3060

[36] G. Demésy, T. Wu, Y. Brûlé, F. Zolla, A. Nicolet, P. Lalanne, and B. Gralak "Dispersive perfectly matched layers and high-order absorbing boundary conditions for electromagnetic quasinormal modes," *J. Opt. Soc. Am. A* **40** (10) 1947-1958 (2023) doi: 10.1364/JOSAA.499370

[37] "A Tutorial: Computing QNMs for a Silver Cube on a Gold Substrate"

[38] G.M. Akselrod, C. Argyropoulus,T.B. Hoang, C. Ciraì, C. Fang, J. Huang, D.R. Smith, M.H. Mikkelsen"Probing the mechanisms of large Purcell enhancement in plasmonic nanoantennas," *Nat. Photonics* **8**, 835–840 (2014) doi: 10.1038/NPHOTON.2014.228

[39] B. Schieche "The Strength of the Weak Form," comsol.com March 18, 2024 www.comsol.com/blogs/strength-weak-form/

[40] W. Ritz "Ueber eine neue Methode zur Loesung gewisser Variationsprobleme der mathematischen Physik," *J. Reine Angew. Math.* **135**, 1-61 (1908)

[41] "Fundamentals of Swept Meshing," comsol.com April 11, 2024 https://www.comsol.com/support/learning-center/article/Fundamentals-of-Swept-Meshing-51861/152

Chapter III

Near-field scanning optical microscopy of integrated photonic integrated circuits (NSOM of PICs)

3.1 Introduction

Near-field scanning optical microscopy (NSOM) is a super-resolution imaging technique that transcends the diffraction limit, which restricts the spatial resolution conventional optical microscopes. Many techniques for super-resolution imaging exist. In scanning electron microscopy (SEM), which was first developed in 1935 [1]. In SEM, a sample is placed in a chamber under high vacuum, and a beam of electrons is raster scanned across the sample and, typically, either backscattered or secondary electrons are detected. Though often used for a broad range of applications, samples must be conductive and grounded in order to be imaged, otherwise a cloud of electrons will form above the surface and obfuscate the image. A close sibling of SEM is focused ion beam imaging (FIB), where rather than electrons, a beam of focused ions (typically gallium), is directed at the sample. In transmission electron microscopy (TEM), electrons are transmitted through the sample, which is typically on the order of 100 nm thick, and then focused onto a detector.

While all of these imaging techniques make use of the fact that the de Broglie wavelength of electrons is much shorter than the wavelength of visible light, scanning probe microscopies (SPM) like scanning tunneling microscopy (STM) and atomic force microscopy (AFM) bring physical probes close to the sample to make nanoscale topographic maps of the surface. In STM, a sharp

metal tip is scanned over a conductive sample, and electrons tunnel between the sample and the tip. Very slight changes in the tip to sample separation will cause a detectable change in the tunneling current. A piezoelectrically-controlled driver adjusts the z-height of the tip, such that the tunneling current remains constant as it scans in *x-y* across the sample. By recording the z-height as a function of tip position, a 2D topographic map of the sample surface is made with high enough resolution to detect individual atoms [2]. AFM, unlike STM, allows for topographic maps of both conductors and insulators. With an AFM, rather than a constant current between the tip and sample, a constant force is held between the tip and sample [3]. This force is often measured via the deflection of a cantilever, although other techniques exist, such as the one we will implement herein, which utilizes piezoelectric quartz tuning forks [4].

Unfortunately, when used to image a PIC on a CMOS chip, all of these techniques would require some form of destructive post-processing. The Si circuits of interest are often buried in a thick (> 1 μm) buried-oxide layer (BOX). This BOX would need to be completely etched away or otherwise removed, to allow for physical contact between the sharp probe and the Si waveguides/devices. The same is true for SEM and FIB imaging, as the charged particles would accumulate to form a cloud on the top SiO_2 surface, making the circuits below invisible. FIB milling and subsequent SEM imaging *is* often utilized, however, to conduct "post-mortems" on PICs. TEM would require the most post-processing, with the PICs needing to be sectioned into 100 nm thick samples before imaging could take place.

In this Chapter, we will describe NSOM techniques that, in contrast to the previously described methods, allow for non-destructive super-resolution imaging of PICs.

3.2 Collection NSOM

Collection NSOM (cNSOM) is essentially a form of AFM where the sharp metallic tip is replaced by a pulled glass fiber with a small-metal coated aperture at the tip. The sample can be illuminated from the top, bottom, through the probe aperture itself, or by connecting it to some other input. The cNSOM tip is then placed close to the sample (typically on the surface like AFM or STM), allowing the aperture to couple near-field light (theoretically any electromagnetic wavelength) at the location of the tip to the optical fiber. Light then propagates through the fiber to a detector. Both z height and light intensity are measured as functions of tip position. Spectroscopic and phase data are also commonly recorded as well. Though this scheme is not limited by Abbe's diffraction limit for optical microscopes, it *is* limited by Bethe's aperture theory, where transmitted intensity through a circular hole (of diameter d) in a thin planar PEC is proportional to $(d/\lambda)^4$. So, as the aperture becomes more and more sub-wavelength, the transmitted intensity decreases dramatically. This will limit the resolution of the measurement depending on the sensitivity of the detector, intensity of the measured field, and the measurement (collection) time.

An added benefit of cNSOM is that, unlike AFM and STM, the probe does not have to be in physical contact with the sample to make a measurement. In fact, any arbitrary plane in space that is physically accessible can be chosen to

collect light from. Though not technically NSOM, in that near-field light is not

collected, this form of scanning probe microscopy (SPM) is widely used [5].

3.3 cNSOM on PICs (the measurement problem)

cNSOM is an obvious candidate for non-destructive super-resolution,

near and far-field imaging of PICs. If there is optical access to the PIC through

the BOX layer, then an NSOM can collect sub-wavelength resolution images of

the radiated light without any additional post-processing required. Some non-

destructive etching of the BOX layer can also be done to decrease the thickness

from several microns to a few nanometers, allowing for a true near-field scan of

the device (as will be described in Sections 3.7-3.9 as well as Chapters V and VI)

Though, on the surface, this technique may seem relatively

straightforward, there is a common pitfall that researchers often encounter. The

main issue lies in the fact that any probe is both a measurer _and_ a perturber. It is

impossible for an NSOM probe, either apertured or not, to collect near-field light

and not disrupt the local fields. The problem becomes how to disentangle the

perturbation from the measurement, and how to understand if the measurement

itself is parasitic to the PIC circuit that the researcher is trying to understand.

Resonant devices are particularly challenging (though much care is

required on non-resonant devices as well) because they are so sensitive to even

the tinniest of impurities or perturbations. To understand this, let's look at a few

examples of published NSOM measurements of resonant photonic devices.

Abashin _et al._ nicely summarizes the main issues that plague NSOM

measurements of photonic resonators [6]. As shown in Figure 3 of Ref. [6], when

the probe is above a bus waveguide, light is scattered, reducing the

transmission of the entire circuit. However, when placed above the resonator, a

resonance shift $\Delta\lambda$ of ~ 1 nm is induced, as well as a dramatic reduction in the

extinction ratio (r_e). This causes a huge issue when attempting to measure the

device. Any time the probe is placed above the ring, the optical properties of the

device are dramatically altered. It is essentially a different circuit depending on

whether or not the probe is above the resonator. The only way to properly scan

this circuit as described and disentangle the perturbation from the near-field

would be to conduct a frequency sweep at every *x-y* location of the probe and

plot $\Delta\lambda'$ and $\Delta\lambda''$ as a function of tip position. Unfortunately, measuring this

way is quite time-consuming and very data intensive, so it is often conducted

using scans at a constant frequency, as shown in the following examples.

Mujumdar, *et al.* imaged a PhC at a selection of wavelengths near and on

resonance as shown in Figure 2 of Ref. [7]. As was the case in the previous

paper (Ref. [6]), they find that when the NSOM probe is above various locations

on the sample, the resonant wavelength is shifted dramatically (as shown in

Figure 4 (b) of Ref. [7]). This $\Delta\lambda'$ is so large, that there is nearly no overlap for the

Lorentzian-shaped resonances between certain tip locations. So, as the tip

scans across the device and collects light, the device itself switches between

"on" and "off" states as a function of tip position. Using the equation for $\Delta\tilde{\lambda}$ of a

Hermitian resonator (not the proper equation for QNMs), they then calculated

how the NSOM scans should look in the presence of a perturber. Agreement is

shown between the simulated perturbed fields and those measured at various

wavelengths in Figure 3 panel (b) of Ref. [7]. However, there is an inherent flaw with this measuring technique. The resonant field as shown in Figure 1 (d) of Ref. [7] can *never* be measured with this technique. This is because the state of the resonator changes with each change in NSOM tip position. Others have conducted the same or similar measurements with nearly identical results [8], yet others have conducted similar studies on non-resonant devices [9].

Although being able to find agreement between simulations that have been amended to predict what the perturbed field would look like is a step in the right direction, it does not have the same value as being able to disentangle the perturbation from the field. Several groups have attempted to do just that with cNSOM. One interesting avenue is the concept of tip "cloaking", where a probe is nano-pattered in an attempt to suppress the tip-induced perturbations by controlling the electric and magnetic polarizabilities [10]. Arango, *et al.* demonstrate decreased tip-induced perturbation in Figure 4 (a-c) from Ref. [10]. Unfortunately, as was the case with the previous examples, these Figures also demonstrate that the resonant mode of a photonic cavity is still dramatically and destructively altered when the nano-pattered probe is positioned above the center.

Rather than try to reduce the tip-sample interaction, le Feber, *et al.* implemented an algorithm to disentangle the three E and three H near-field components of a photonic crystal waveguide (PhCW) collected by the probe [11]. As shown in Figure 3 of Ref. [11], their results are promising. However, the authors note in the conclusion that using this method for cavities with $Q > 1,000$

would require special care to be taken, as the tip-sample interaction would become large. So, this method would not be useful for our measurements of Q >10,000 devices.

The issue with these schemes is that an apertured NSOM probe is simply too large of a perturbation to the strong near-fields of a high Q resonator. With so much energy confined to such a small volume, perturbations of this magnitude are detrimental the resonator's function. Though cNSOM appears to be an elegant means of near-field characterization, another solution, with a smaller perturbation, is required.

3.4 Scanning thermal microscopy (SThM) of PICs

Scanning thermal microscopy (SThM) is one near-field imaging candidate that has shown promising results in recent years. Ironically, this method of near-field imaging was discovered somewhat by accident. Originally, Tzur, *et al.* set out to to understand the issues of self heating and heat removal in PICs [12]. In their study, a Pt-Au thermocouple probe with a roughly 300 nm diameter tip is used to investigate a Si ring resonator which is evanescently-coupled to a bus waveguide. Although they report a 10° C increase in Si temperature as a result of linear absorption from a 2 mW laser source, this result was quickly amended by Grajower, *et a*l [13]. In that work, they report that the heating isn't sample induced, rather, it is field induced. They find that the temperature measured at the tip is directly proportional to the optical input intensity. Instead of SThM measuring the temperature of the silicon waveguide, it is measuring the strength of the absorbed field.

Though this technique cannot be used to measure thermal effects in PICs, it is well suited for measuring the near-field of PICs. Figure 3 of Ref [13] demonstrates the ability of SThM to measure the near-field of a Q = 30,000 micro-disk resonator in a PIC. Though this is a proven method for near-field characterization of PICs, we will investigate a more simple solution with smaller tip sizes that allows for higher resolution images.

3.5 traNSOM of PICs

Transmission-based NSOM (traNSOM) is a near-field imaging technique that, unlike the previously described methods, takes advantage of the PIC architecture, and uses the PIC output as the measured signal. A schematic of a traNSOM measurement is depicted in Figure 3.1. An apertureless probe scans across a PIC and, much like a scattering type NSOM (s-SNOM) [14], the tip scatters and absorbs the local near-field light. With the normal PIC input being the light source, the PIC output is also the NSOM signal. Using a metallic tip, Robinson, *et al.* first implemented the traNSOM technique to imaged highly confined modes in Si waveguides [15]. As seen in Figure 3 panel (d) of Ref [15], change in transmittance ΔT is measured through the PIC and plotted vs *x-y* tip position. As the tip scatters light, the optical power transmitted through the circuit decreases. Their scans demonstrated sub-micron resolution and strong agreement when comparing with simulated ΔT. This group went on to conduct further traNSOM studies of near-field intensities of single-mode silicon waveguides [16].
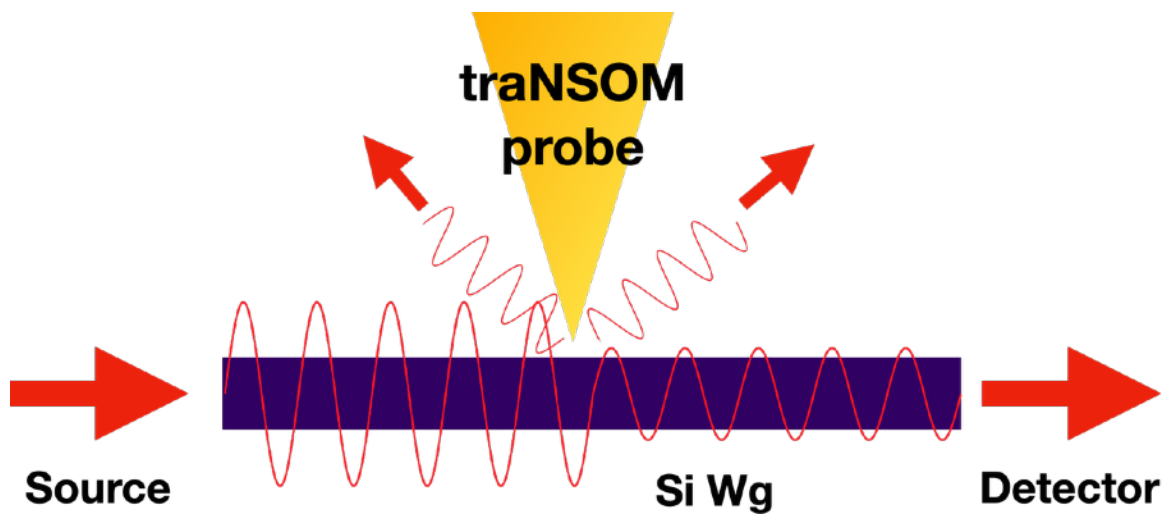
Figure 3.1 Cartoon of traNSOM experiment.
Red sinusoidal curves depict the intensity of light as it propagates through the
waveguide and is scattered by the apertureless tip. Red arrows depict the direction of
light propagation.

There are many advantages to this NSOM technique. Instead of the scattering and absorption being detrimental to the measurement and significant post-processing of data being required to disentangle the two, the desired data are inherently baked-in without any disentangling required. Without the need for light to be collected through the probe, the tip can be as small as desired. With the freedom to select various tip sizes and materials, the tip-induced losses can be tuned depending on the sensitivity required; if the perturbation is too small to be detected a larger tip can be used, if the perturbation becomes detrimental to device performance the tip size can be decreased.

3.6 Our NSOM set-up

As depicted in Figure 3.2, a Nanonics Multiview 4000 is used for our experiments. This system allows us to conduct both cNSOM and traNSOM measurements simultaneously. The set-up consists of a metallic sample stage on which sit two towers, labeled blue and yellow. Each of these towers is connected to a separate computer which runs the Nanonics NSOM custom control software. The towers control both the macro and nano-positioning of the NSOM tip. While both are controlled via piezoelectric transducers, the range for macro positioning is on the order of several mm, whereas the nano positioning during a scan only encompasses a 35 µm square window. We have added an additional piezoelectric micro manipulator, the Sutter Instruments MP-225 [17], to position either the output or input fibers which are coupled to the PIC. Though not visible in Figure 3.2, there is a roughly 2 cm hole in the middle of the stage that allows light to be either collected or input via the lower microscope.
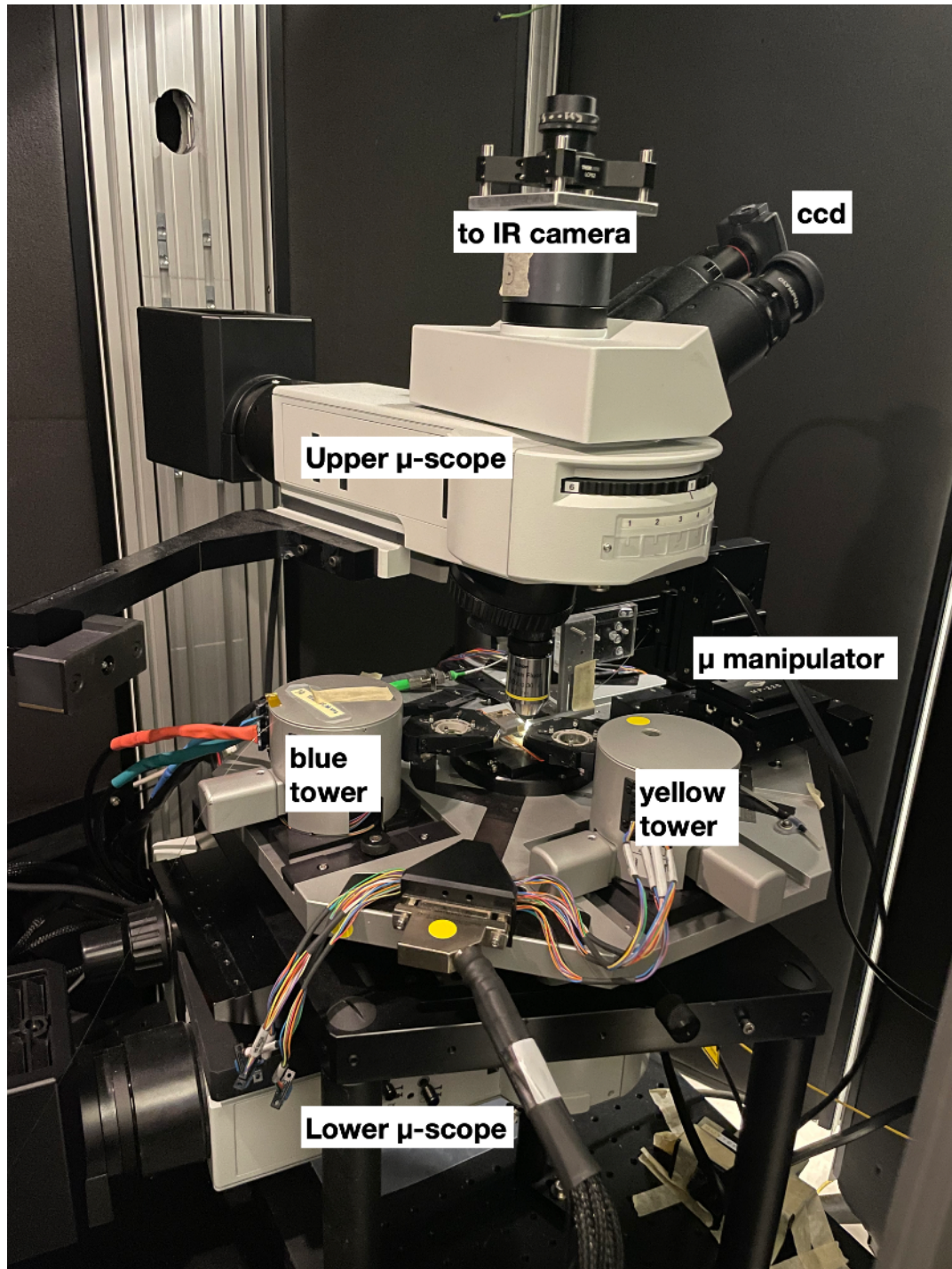
Figure 3.2 Photograph of Nanonics Multiview 4000 NSOM set-up.
Shown is the set-up used for the following NSOM experiments, two towers allow for *x-y-z* piezoelectric manipulation of NSOM probes. An additional micro-manipulator was added to control additional output and input fibers. Though not shown, an IR camera could be attached to the top of the upper microscope.
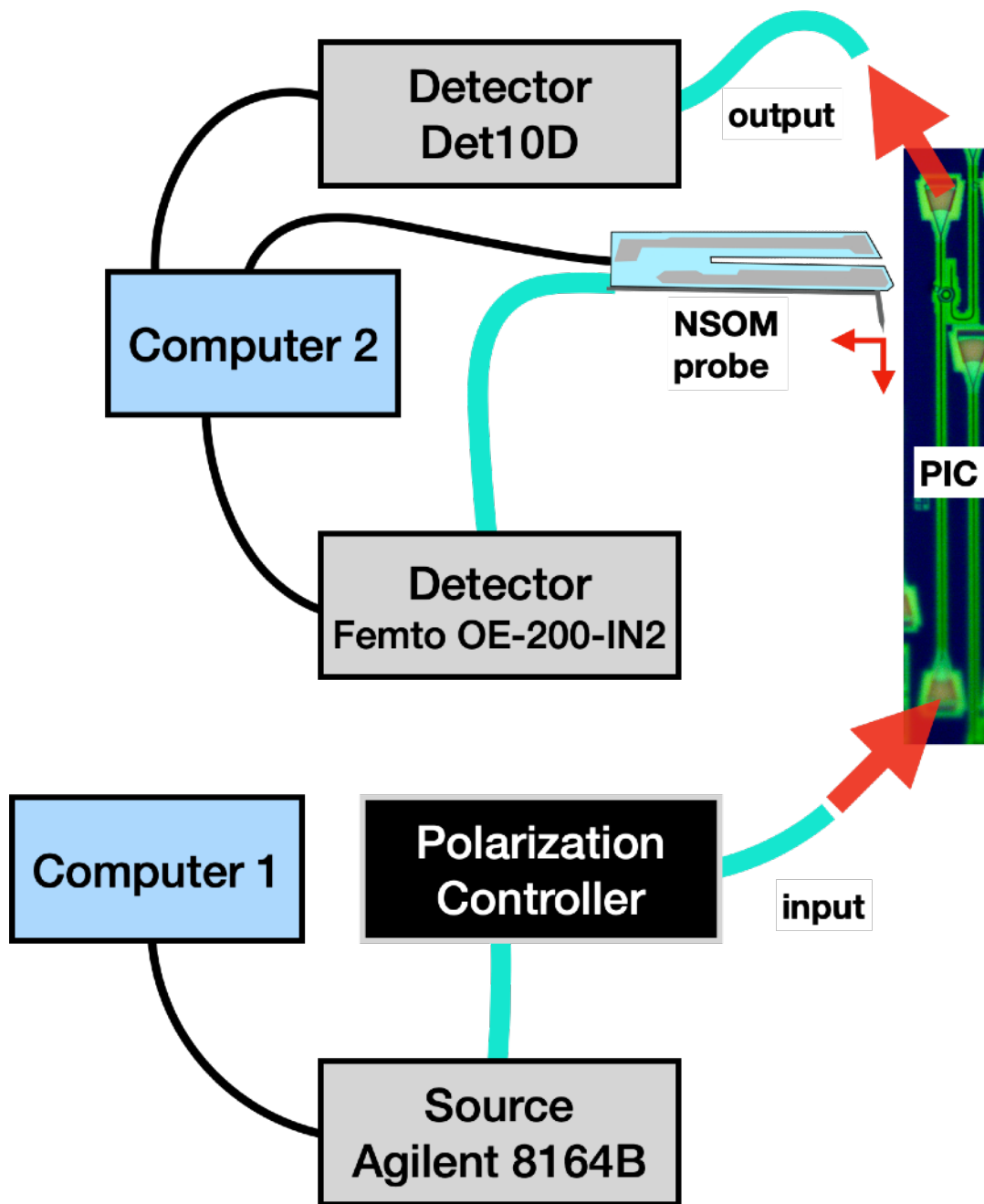
Figure 3.3 Schematic cartoon of experimental NSOM set up.
The light blue curves represent optical fibers with the translucent red arrows depicting coupling into and out of the PIC. Computer 1 controls the source while computer 2 collects data from the detectors and controls the NSOM positioning

Typically, we would only use the upper microscope to illuminate and image the sample while we positioned the various optical fibers and NSOM probes. A CCD camera is connected to one of the eyepieces, while an IR camera can be attached to the top of the upper microscope. The entire system is encased in a foam and metal box and sits on a vibration isolation table (look up model number). (Although, it is still important to plan the timing of experiments wisely. The NSOM is located below a few classrooms, so if one conducts a scan during a period of time when students are walking between classes, at best one's scans will appear a little shaky, and, at worst, the vibrations will cause the probe to break against the sample surface.)

To understand further how this experimental set up works, we refer to the schematic in Figure 3.3. Light is generated by a computer-controlled Agilent 8164B O-band tunable laser source and fiber-coupled to manually operated polarization controller paddles. From there, light travels through an optical fiber and is coupled via GC to a PIC. A GC at the end of the PIC directs the output signal into an optical fiber, which guides it to a Thorlabs DET10D InGaAs detector. (For tuning purposes and frequency sweeps, the output light was coupled back to the Agilent and monitored via Computer 1.) Another computer controls positioning and scanning of the NSOM probe via the yellow tower. If a cNSOM scan is conducted, the collected light is detected with the Femto OE-200-IN2 avalanche photodiode. Measurements from both detectors are collected with the same computer that conducts the NSOM scans.
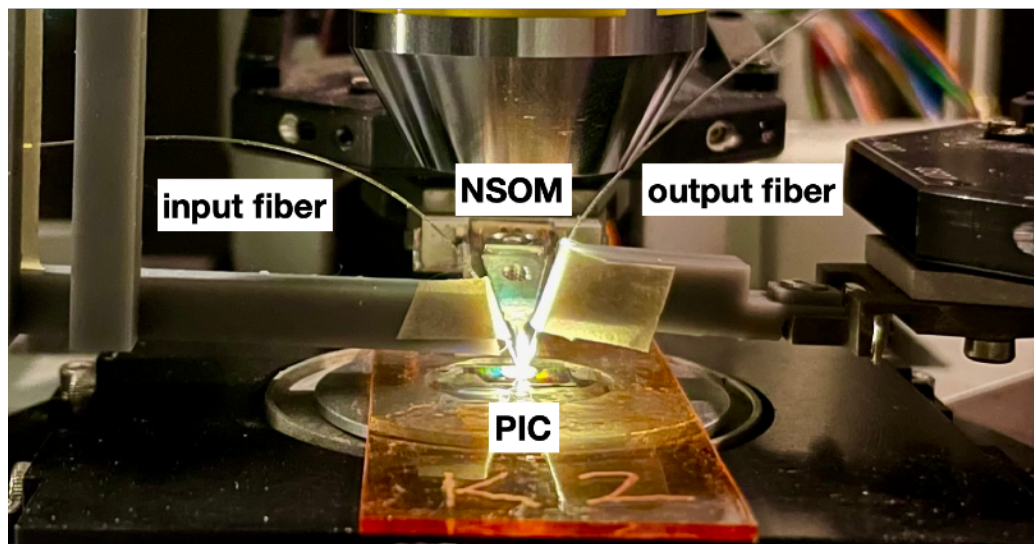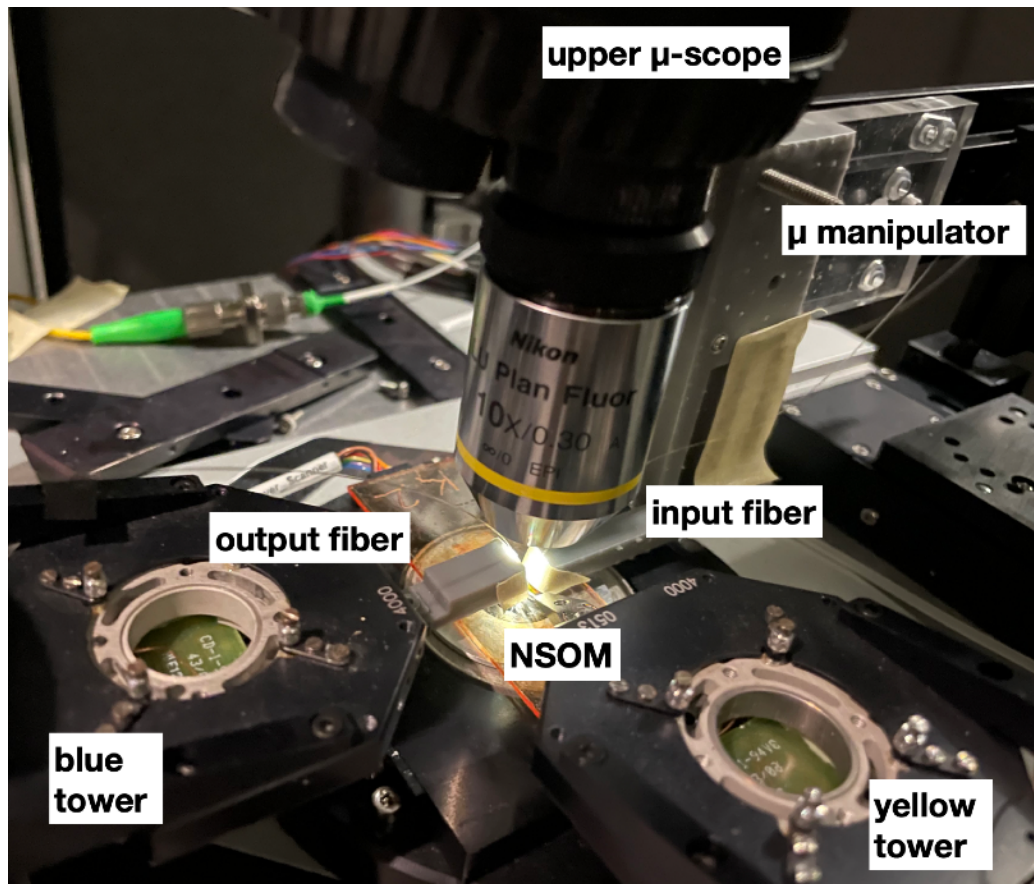
Figure 3.4 Close up photographs of Nanonics Multiview 4000 NSOM set-up.
Shown is an example layout of an NSOM scan of a PIC. Output and input fibers couple light into and out of the PIC. The output fiber is connected to a re-purposed NSOM tower. 3D printed holders are used to mount the output and input fibers to the NSOM tower and micro manipulator. Though the optical microscope is illuminating the sample, it was often turned off during the measurements to reduce heat build-up.

With an understanding of how the scans operate, let's take a closer look at the experiment in Figure 3.4. The input fiber is mounted to the Sutter Instruments micromanipulator with a 3D printed (Formlabs) fiber holder. The micromanipulator is operated with a proprietary controller and has no ability to be computer controlled or monitored. A simple piece of tape is used to adhere the fiber to the holder, which has a groove through the middle for the fiber to sit in. Once light has traveled through the PIC, it is coupled via GC to the output fiber. This fiber is mounted with another 3D printed holder to the blue tower which is controlled by a 3rd computer not shown in Figure 3.3. The upper microscope, which is used for imaging and to observe positioning, is also connected to computer 3. The NSOM tip is manipulated with the yellow tower which is controlled by Nanonics software on computer 2.

The feedback mechanism used in the Nanonics NSOM system is slightly different from the conventional AFM and NSOM method. Traditionally, a cantilever with a sharp dielectric or metallic tip is driven at a high frequency as it approaches a sample. When the tip touches the sample, the cantilever bends as a result of the contact force. To maintain a constant force, a laser is reflected off the top surface of the cantilever into the center of a photodetector. As the probe scans in x or y, a change in z height of the sample will either increase or decrease the contact force, which changes the amount that the cantilever is bent and the positioning of the laser on the detector. A feedback mechanism then changes the z height of either the probe or the stage until the laser light is once again positioned in the center of the detector, returning the contact force
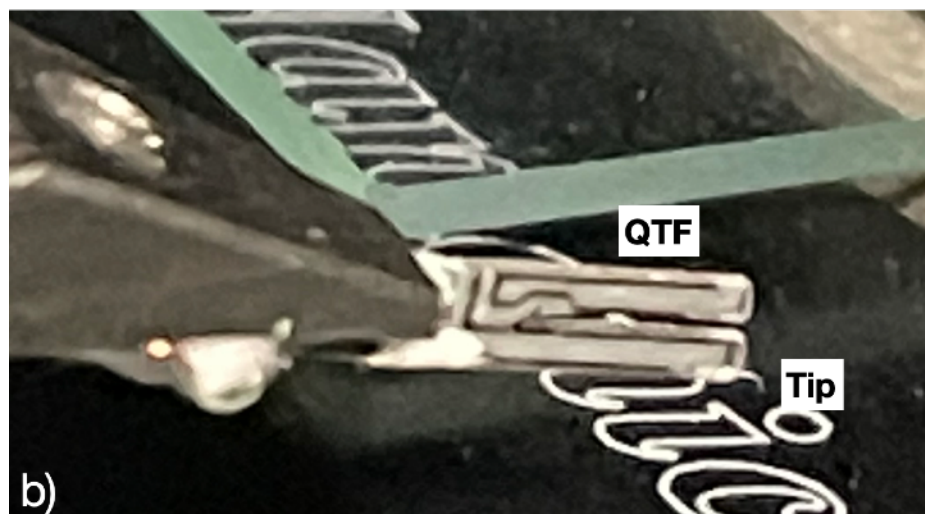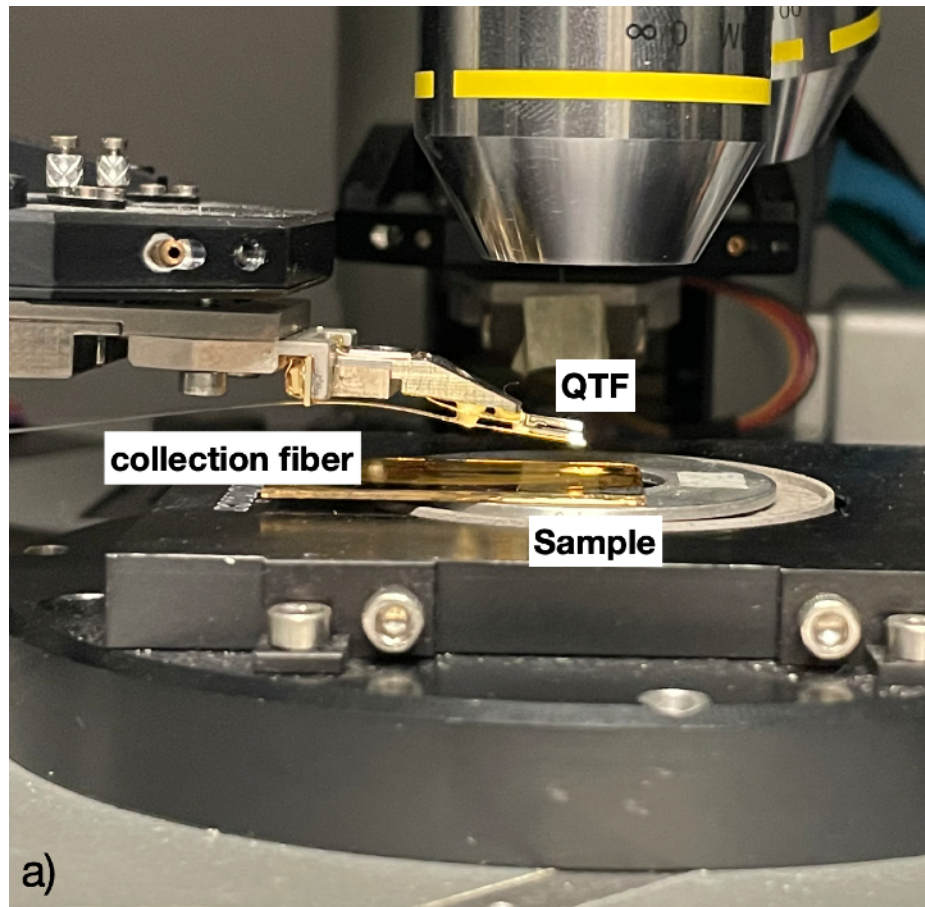
Figure 3.5 Close up photographs of cNSOM Probe.
The cNSOM probe has a quartz tuning fork QTF based feedback mechanism which controls the tip sample separation. Visible in the image (a) are the the tapered glass collection and the quartz tuning fork which is placed above the sample. The tip which is curved at the end of the QTF is visible in image (b).
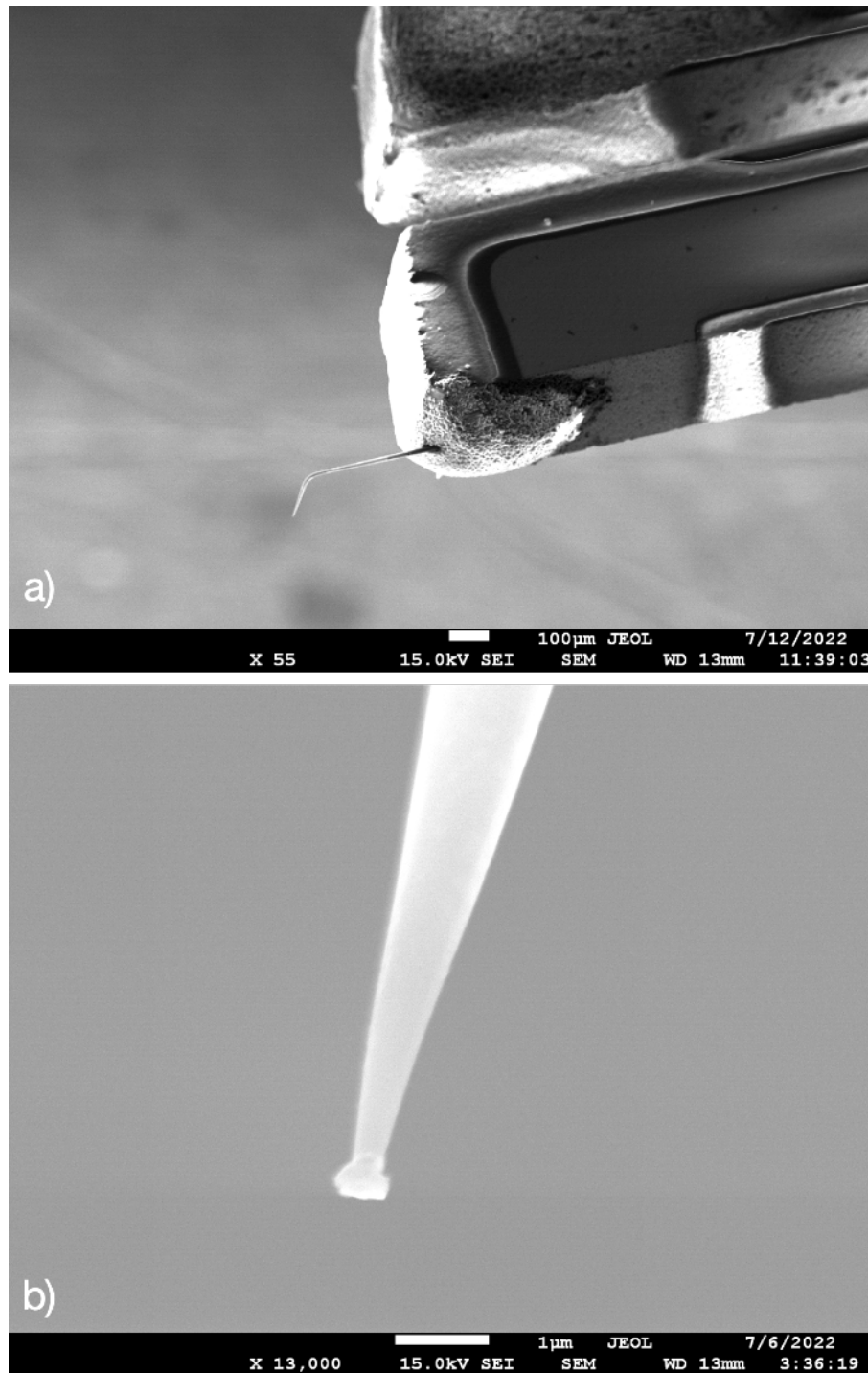
Figure 3.6 SEM imaging of an apertureless NSOM probe.
(a) SEM image displaying the end of the QTF with a small curved metallic tip adhered to the bottom surface. (b) Close up of the end of the metallic tip which comes in contact with the surface of the sample.

to its original value. This z height is collected as a function of tip position to generate a topographic map of the sample.

Rather than a cantilever, the Nanonics system relies on a more elegant solution: a quartz crystal tuning fork oscillator (QTF). QTFs are most commonly used in digital watches to keep time. They are designed to reliably resonate at 32.768 kHz so that, when placed in a circuit with 15 flip flop gates which halve the frequency, 1 second is counted after all $2^{15} = 32,768$ flips of the gates [18]. Because of this use, QTFs have been engineered to be precise, reliable, small, inexpensive and abundant. As of March 2024 one can purchase a single 20 ppm 32.768 kHz QTF for as little as $0.11 if bought in bulk [19]. A Nanonics Multiview 4000 probe consists of a QTF which is placed on its side with a sharp tip (Figure 3.6) or a sharp pulled tapered fiber (Figure 3.5) adhered to the bottom end of the lower prong. QTFs are very sensitive to changes in mass of the prongs so, with a tip being placed on one prong, a small amount of mass is added to the other to balance the resonance. Much like a cantilever tip, the probe is driven on resonance as it approaches the sample. Once contact is established between the sharp tip and the sample, the resonance of the tip will shift, causing a change in the error signal. In the same way that the feedback mechanisms in a cantilever system keep the laser at a constant position, the feedback of our NSOM system works to keep the error signal at a constant value. The user can determine what the set-point is for this error value, which corresponds to the strength of the contact force. Once again, as the tip scans, the *z* position of the

piezo is recorded in tandem with the *x-y* position to generate a topographic map of the sample.

Although topographic maps aren't a point of focus in our research, keeping the probe exactly on the surface while limiting the contact force is necessary when conducting an NSOM scan. Too high of a contact force will likely break the tip and, with the near-field intensity exponentially decaying as a function of distance, any small separation from the surface will dramatically reduce the signal. (As a side note, even with optimal feedback settings, tips tend to break and wear over time. Over the course of this project alone roughly 20 tips were consumed.) With our NSOM set-up, computer 2 controls the NSOM scan and collects signal from the DET10D and Femto detectors. So, one scan can generate as many as 3 separate maps as a function of tip position: height, cNSOM intensity, and PIC output intensity.

3.7 Sample preparation and buried oxide (BOX) thinning

Now that we have an understanding of the measurement apparatus, it is time to take a look at the PIC chips. The chips, which were designed by the Popovič group in the Electrical Engineering department at Boston University, were fabricated using GlobalFoundries 45 SPCLO process at FAB8 in Malta, New York. 45 SPCLO is a 45 nm Si-on-insulator (SOI), CMOS technology that allows for the monolithic integration of O- and C-band photonic, digital, and RF ICs [20]. When the chip arrives from GlobalFoundries, some critical post-processing is required to gain optical access to the PICs. Panels (a-c) in Figure 3.7 depicts the flip-chip procedure, which was conducted by Deniz Onural and
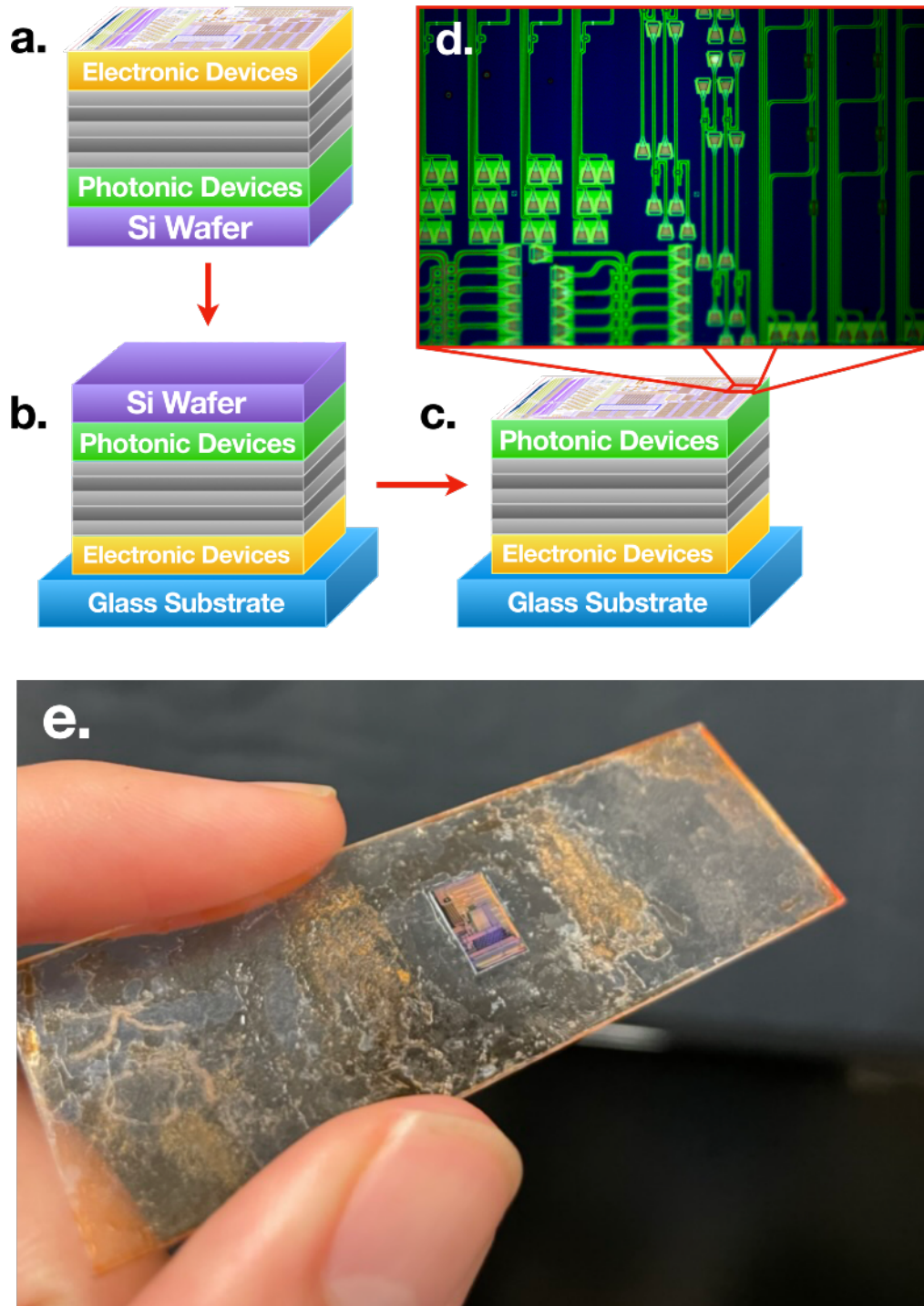
Figure 3.7 Cartoon of flip-chip post processing procedure.
(a-c) Cartoon of flip-chip procedure. (d) Micrograph of PIC after the flip-chip process has been completed. (e) Photograph of the entire chip with the PICs visible.

other members of the Popovič group. As the chip arrives, the electronic circuit contacts are on the top layer with the Si wafer serving as the base. The PICs, which are embedded in a several micron thick SiO2 buried oxide (BOX), are in the first device layer, just above the Si wafer. The first step of the flip-chip procedure is, naturally, to flip the chip over and either bond it to a glass slide, as we have, or to a circuit board which can control the electronic circuits. Next, the Si wafer is completely etched away with XeF_2, leaving the PIC layer as the top surface. Now, as is seen in panels (d) and (e) of Figure 3.7 optical investigation and experiments can begin.

While this procedure has granted optical access to the PIC, with the BOX being several microns thick, more etching needs to be completed to access the near-field, which extends less than λ above the PIC. Special care must be taken in this next step, as this BOX thickness will be critical in determining the strength of the perturbation caused by the tip. Additionally, since the Si waveguides are embedded in the BOX layer, over-etching on a large scale will dislodge the Si PICs. To properly monitor the etch rate and oxide thickness, windows are opened via etching up above another PIC that is not being measured in this experiment. These windows will allow us to make profilometry measurements that determine the oxide thickness above the top surface of the Si waveguides (this thickness will be referred to as *t*). The windows are created by Deniz Onural at BU using precise photolithography. The location and appearance of the rings which will have windows are shown in Figure 3.8, while a cartoon of the process is shown in Figure 3.9. First, a photoresist layer is spun
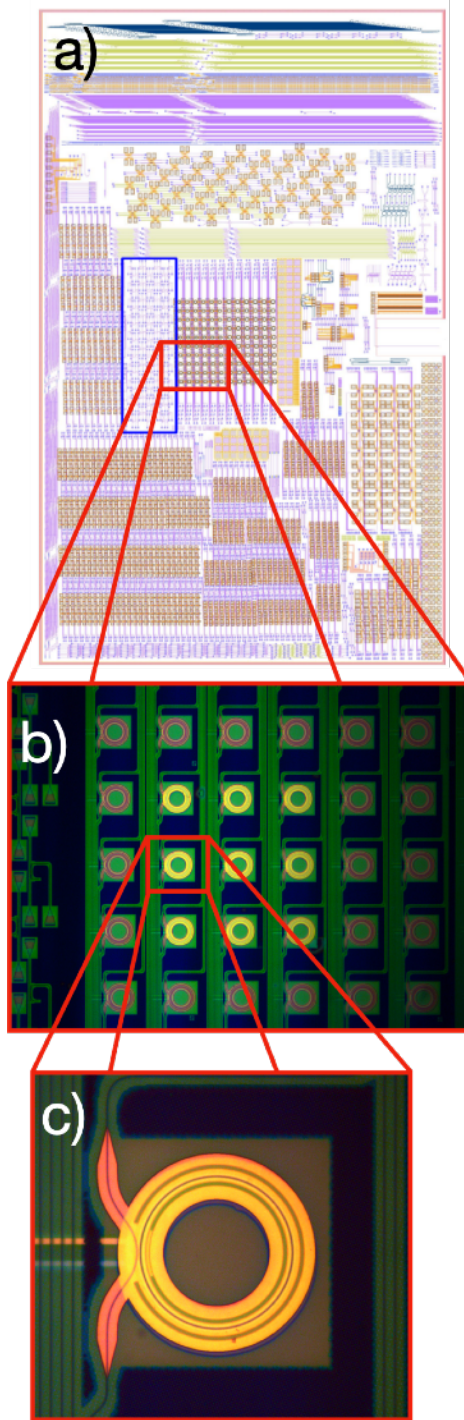
Figure 3.8 Rings used to measure oxide etching.
(a) Layout of chip with red square around the location of the exposed ring resonators.
(b) Optical micrograph of etched rings, which appear much brighter than the un-
etched rings. (c) Zoomed in image of an etched ring.
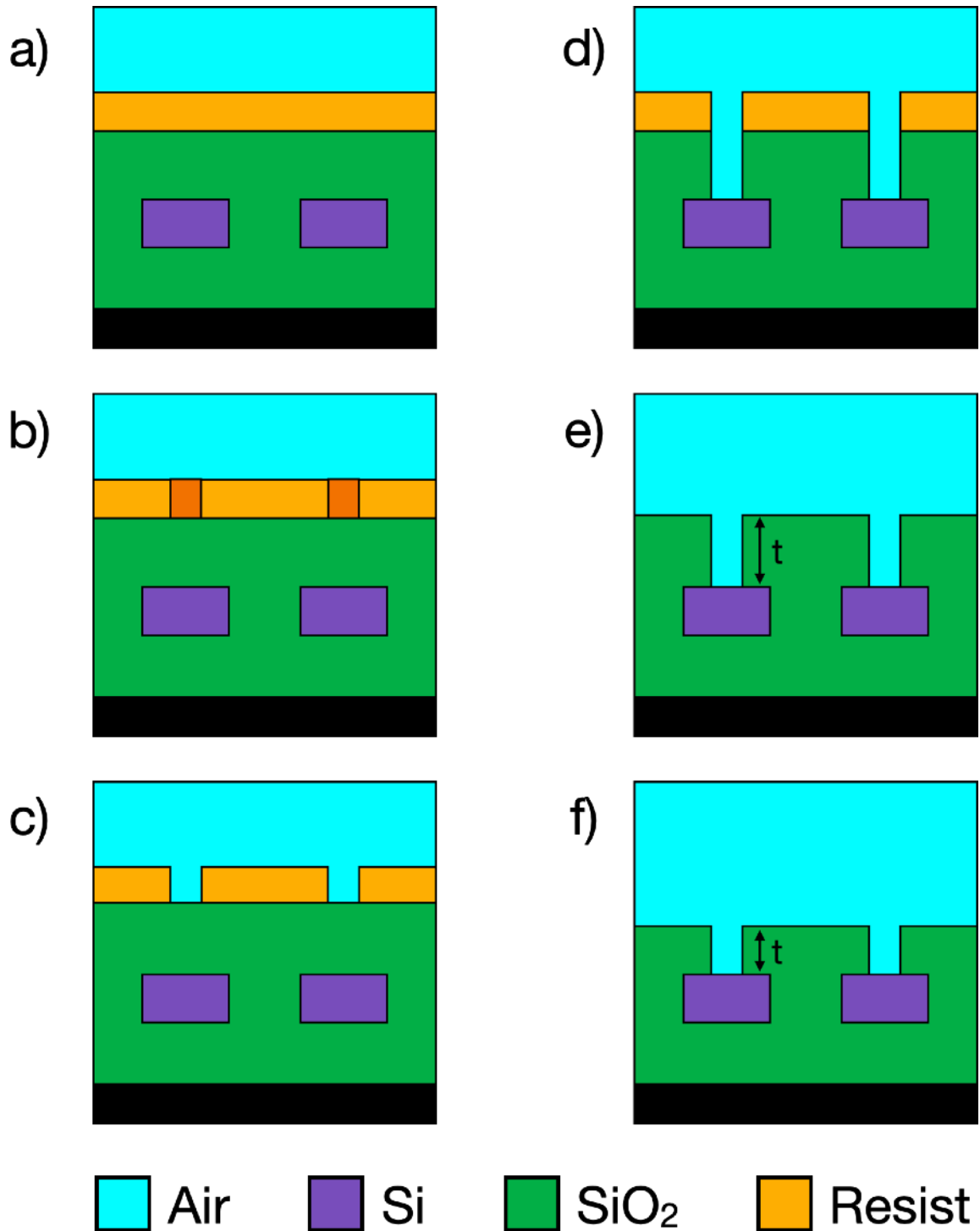
Figure 3.9 Cartoon of the ring exposing and BOX etching procedure.
(a-f) Cross-sectional cartoon of procedure with oxide thickness above waveguide *t* labeled.

over the entire BOX layer. Next, the sample is exposed with UV light to create ring windows in the resist above the Si rings. With the windows opened, buffered oxide etch (BOE) is used to etch the SiO_2. Since the BOE etch rate of Si is near zero, over-etching is not a concern with this step [21]. The process is complete once the BOX has been completely etched so that the top of the Si is exposed. With the resist layer removed, a profilometric measurement can be conducted to determine t.

Now that the windows have been opened and t can be measured, all subsequent etching steps to decrease t are straightforward. For reasons that will become more clear later in this Thesis, we want to have a small tip-sample separation of somewhere between 50 nm and 500 nm. The planarized BOX layer t is the perfect way to ensure that this tip sample separation is precisely controlled. To control this t, the entire chip will be etched so that t is the same at all locations. The chip is simply dipped in buffered oxide etch 7:1 (BOE) and removed after a certain period of time determined by the known BOE etch rate. Some agitation with a magnetic stirrer is used to assure a stable etch rate. Once the etching is complete, the previously opened windows are used to measure t. We can be confident that the t is roughly constant across the chip because there is consistent color of the BOX layer. Dramatic changes in color reliably occur for roughly every 25 nm change in SiO_2 thickness [22]. As can be seen in panels (d) and (e) of Figure 3.10, the color change is easily visible in an optical microscope. When comparing panel (d) of Figure 3.7 and panel (a) of Figure 3.10, which were both taken after the same etching step, the color is consistent across the entire
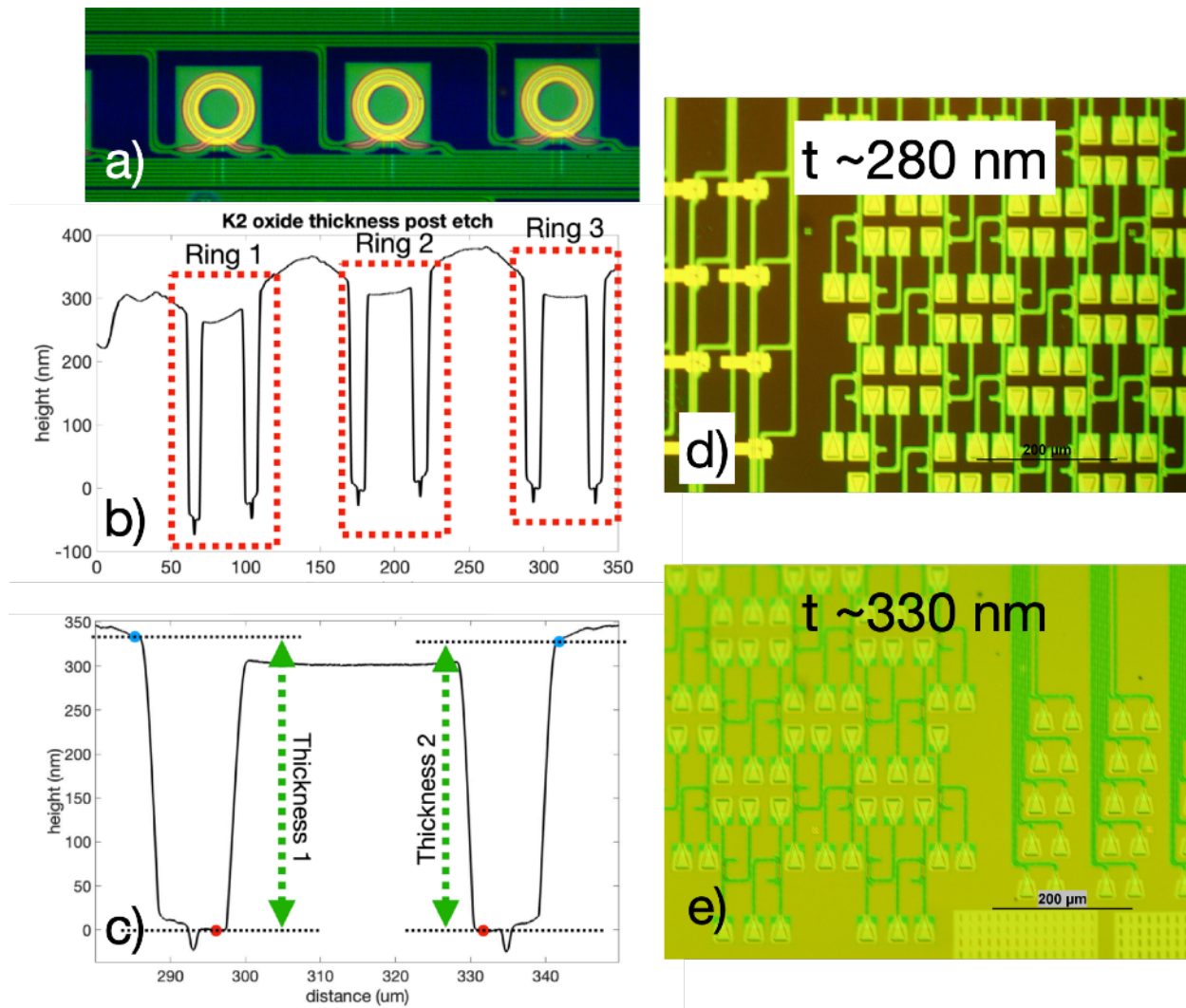
Figure 3.10 Depiction of oxide etching procedure.
(a) Optical micrograph of etched rings which were used in profilometry scan. (b) Raw data from profilometric scan. (c) Leveleed data from one ring. (d) optical micrograph of chip with $t \sim 280$ nm. (e) optical micrograph of chip with $t \sim 330$ nm.

chip, providing confidence that the measured t will remain the same for all PICs on the chip.

To understand how t is measured, let's first look back to panel (b) of Figure 3.8, which shows a 3 x 3 array of exposed rings. It is easy to determine which rings are exposed because of their brighter appearance. We then scan the profilometer across three of the rings, making sure that the tip travels straight through the center axis of the rings. In panel (a) of Figure 3.10, we can see an example of the three rings and results from scanning across them are shown in panel (b). The data are not completely smooth across the entire 350 μm scan, so the plot is leveled numerically for each individual ring, with the result after leveling one of the rings shown in panel (c). Once the ring has been leveled, two measurements of t can be made by subtracting the height shown at the right red dot from the right blue dot, and the same for the left side. Note that the center of the ring is slightly less thick than the exterior edges. Because of this, only points on the exterior of the ring are used to determine t. With one scan, six measurements for t can be made to generate an average and standard deviation. With measuring complete, we can either continue to a measurement, or complete another etching step and re-measure.

3.8 Tip-Sample interaction measurement

To understand how the tip interacts with a resonant photonic device, and how t changes that interaction, frequency sweep measurements are conducted with an apertureless traNSOM tip both on the surface of the ring (as labeled in Figure 3.12 (a)) and without the tip present, at several different oxide
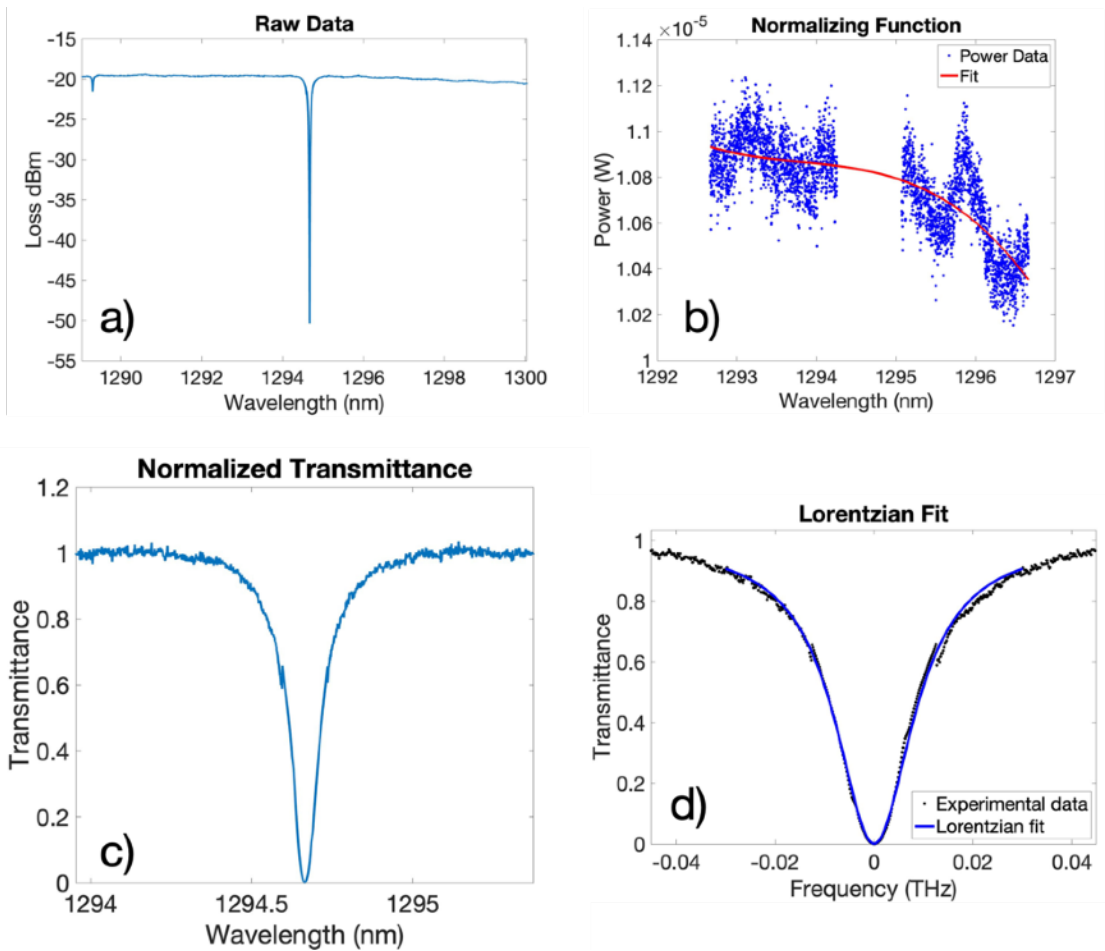
Figure 3.11 Plots from MATLAB curve fitting process.
(a) Raw data as it is imported into MATLAB. (b) Depiction of fit, used to normalize curve (c) Data after being divided by the normalizing function. (d) Depiction of calculated fit plotted alongside experimental data. Data is with t = 145 nm and the tip away from the surface.

thicknesses. A MATLAB program was written to extract λ', r_e, and FWHM by fitting a Lorentzian-shaped curve to the experimental data.

Figure 3.11 explains how this MATLAB program extracted those values. As collected by the Agilent software, insertion loss (dBm) is plotted vs. wavelength. However, with any photonics set-up, the loss is wavelength-dependent. To account for this, a normalizing function approximates the shape of the curve near the desired resonance as shown in panel (b). We can then divide the initial power data by the normalizing function to get the plot shown in panel (c). The inverse of the minimum transmission value on this plot is the calculated extinction ratio with the x value being λ'. Next, we fit the expression

$$T = \frac{x * T_{min} + \omega^2}{x + \omega^2},$$

(3.1)

to the experimental data using lsqcurvefit which is a least-squares curve fitting algorithm in MATLAB that solves for x [23]. $\sqrt{x}$ is the FWHM. Therefore,

$$Q = \frac{\lambda'}{2\sqrt{x}} = \frac{\lambda'\tau}{2}.$$

(3.2)

This software is used to compute r_e, λ', and Q with a 50 nm diameter apertureless traNSOM tip both on the x of Figure 3.12 and far away from the surface for $t = 210$, 171, 146, 126, and 106 nm. Uncertainty in thickness is determined by taking several measurements of t from multiple scans as described in the previous Section. Uncertainty for r_e, λ', and Q are determined from multiple measurements with the tip both on and off. To understand this
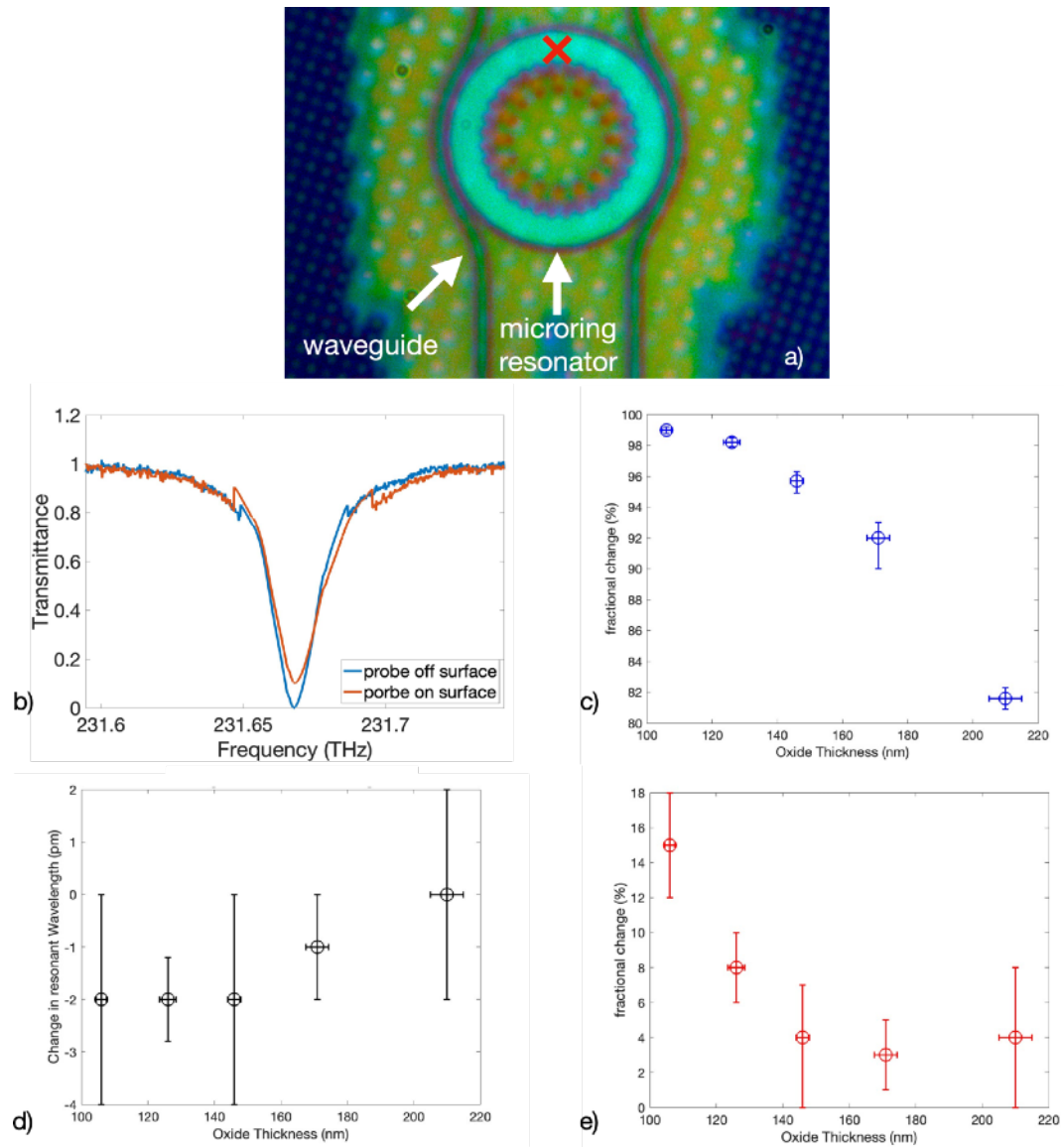
Figure 3.12 Frequency sweep comparison of NSOM probe on and off resonator.
(a) Micrograph of resonator with "x" denoting the location of the NSOM probe. (b)
Comparison of sweeps with probes both on the x and far away from the chip. (c)
Fractional change of the extinction ratio, (d) change in resonant wavelength, (e)
fractional change in the quality factor as a function of *t*

data, lets first look to panel (b) of Figure 3.12 which compares a frequency sweep with no perturbation ("off") to a sweep with one at position x ("on"). The "off" scan has a strong resonance with T appearing to go to zero. However, the "on" scan does not have as dramatic a resonance, with the minimum T only appearing to be about 0.1. From this plot, it is hard to determine if there would be a change in Q or λ'. Looking at panel (c), it is clear that the presence of the NSOM tip dramatically decreases r_e. Even at an oxide thickness of 210 nm, the fractional change is greater than 80%. As the oxide is thinned, this fractional change gets even greater. The same is not the case, however, for λ', shown in panel (d). For all but one oxide thickness, a change of 0 pm fell within the error bars. The same was also true for Q at thicknesses above 146 nm. However, as the oxide is thinned, dramatic changes in Q are measured.

To summarize, the presence of an NSOM tip above the resonator decreases the r_e dramatically with increasing effect as the tip gets closer to the resonator. With perturbation-induced scattering decreasing r_e, Q also decreases. However, Q is not quite as sensitive as r_e, and at further tip-sample separations, a change in Q is not detected. While induced losses caused notable changes in Q and r_e, the same cannot be said for λ', which experienced statistically insignificant changes as a result of the perturbation. This agrees well with the results from the simulations conducted in Chapter II, which predict that the perturbation will induce losses and decrease Q, but will have no noticeable affect on λ'.

3.9 Combined traNSOM and cNSOM measurement

Before continuing to our major results, it is worth describing two more studies exploring on how PICs are affected by NSOM measurements. To do so we conduct simultaneous cNSOM and traNSOM scans of a waveguide and a PhCnB to demonstrate how different types of devices are more or less suited to each type of NSOM.

First, let's take a look at the results from the waveguide scan in Figure 3.13. As the apertured NSOM scans directly above the waveguide, light is coupled through the probe and detected by the FEMTO, as seen in panel (b). Looking at panel (c) however, we can see that as the apertured tip scans over the waveguide, it collects, scatters and absorbs light, causing the output as measured by the DET10D to decrease. As expected, a cNSOM scan cannot be conducted without decreasing the light transmitted through the waveguide. In this case, the scattering is not detrimental to the experiment and information can still be gleaned from the cNSOM measurement. For the next example, we will see that this no longer holds true.

To test the affect of a cNSOM probe on a high Q, low V resonator a, 150 nm diameter aperture tip is scanned above the C-Band PhCnB shown in panels (a) and (e) of Figure 3.14, with the input wavelength being that of the fundamental mode $\lambda_0' = 1570.412$ nm and the first order mode $\lambda_1' = 1586.172$ nm. Both minima were determined first by frequency sweeps, then by wavelength tuning near resonance to minimize output intensity. Looking first at the fundamental cNSOM scan in panel (c) as the tip scans across the waveguide
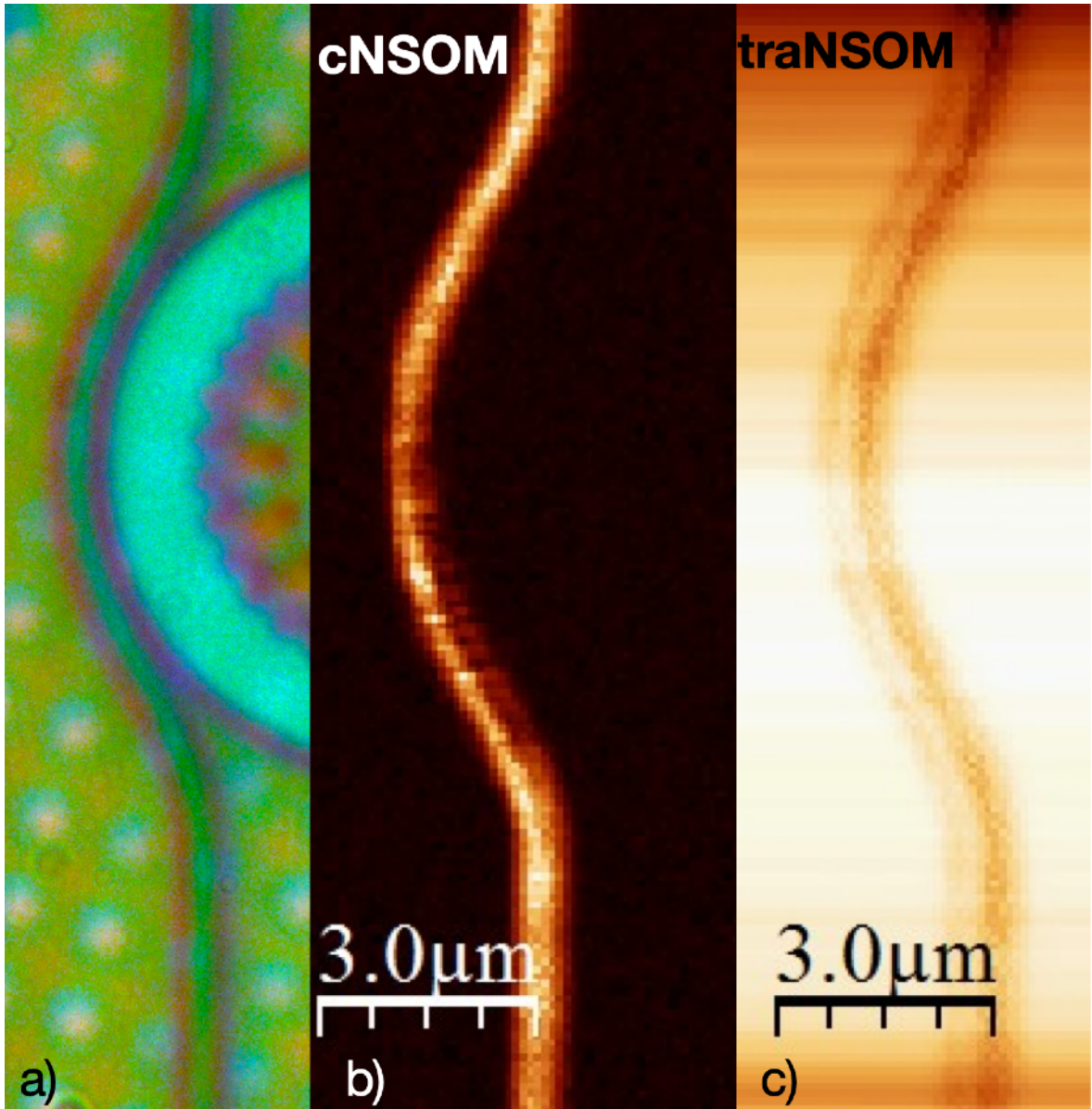
**Figure 3.13 Combined cNSOM and traNSOM measurement of Si waveguide.**
(a) Micrograph of waveguide. (b) cNSOM (c) traNSOM
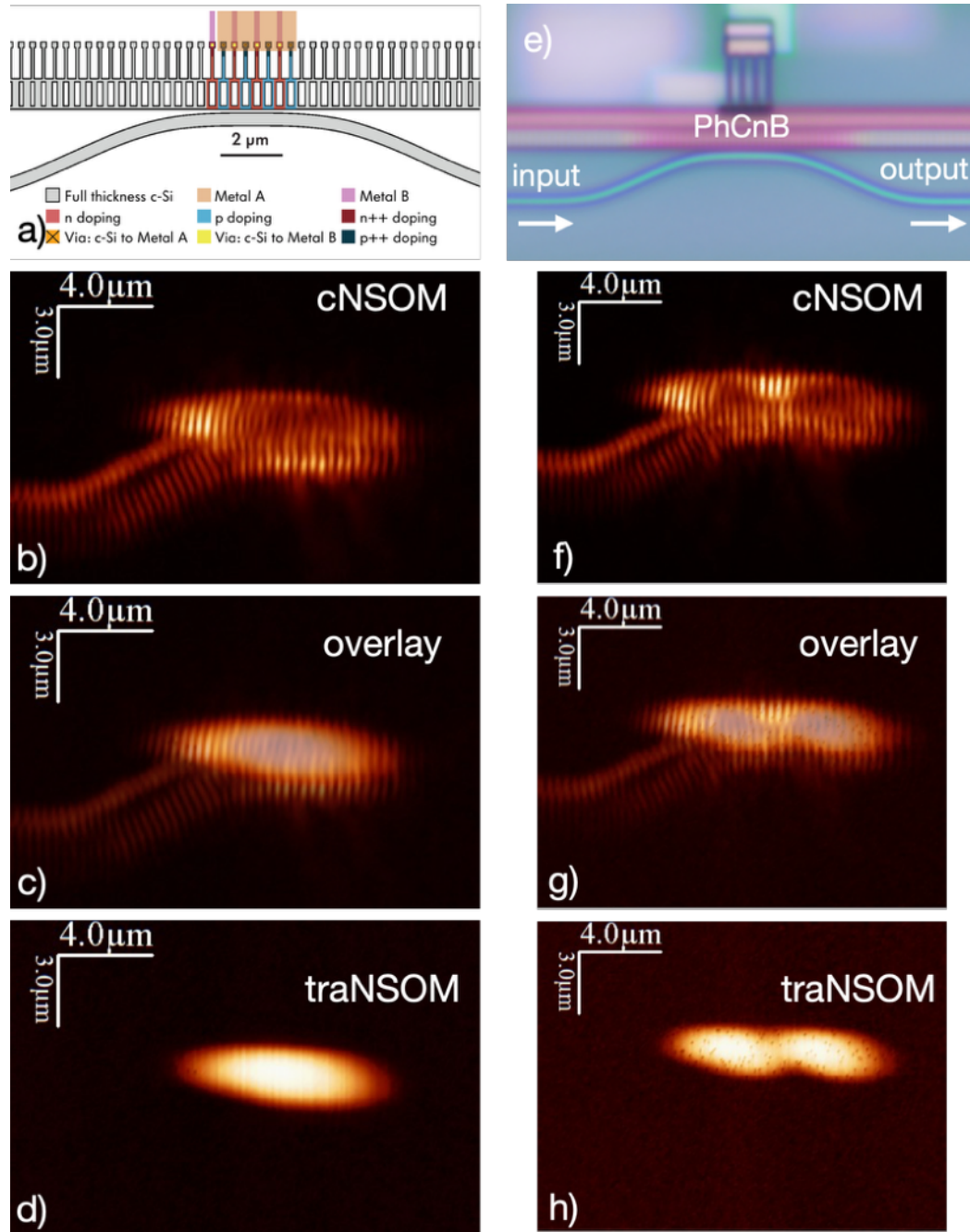
Figure 3.14 Combined cNSOM and traNSOM measurement of PhCnB.
(a) Schematic of PhC design. Scans of the fundamental mode (b) cNSOM (c) Overlay of cNSOM and traNSOM. (d) traNSOM. (e) optical micrograph of PhCnB. Scans of the first order mode. (f) cNSOM (g) Overlay of cNSOM and traNSOM. (h) traNSOM.

on the input (left) side of the PhCnB, light is collected with a relatively constant intensity and characteristic fringes are visible. As the tip scans from left to right over the PcHnB, intensity begins to increase dramatically. However, with the tip still several microns away from the PhCnB center, intensity decreases. An intensity minimum appears near the center of the PhCnB, with intensity increasing slightly as the tip moves towards the right of the cavity. As the tip scans to the right of the cavity, no light is detected in the output waveguide. Looking now to the traNSOM signal in panel (d) of Figure 3.14, since transmitted intensity is so low in the on resonance state, there is no detected change when the tip scans above the input waveguide. When the tip scans above the PhCnB, output intensity increases dramatically. A maximum appears to be located at the center of the PhCnB. When these two signals are overlayed in panel (c), there is clearly a direct correlation between the decrease of cNSOM signal and the increase of traNSOM signal at the center of the PhCnB.

Looking to the scans of the first excited state where we would expect to see a minimum in intensity at the center of the PhCnB and two maxima on either side, we actually see the exact opposite in the cNSOM signal, with the expected intensity profile of a minimum at the center and two maxima on either side in the traNSOM signal. Once again, when overlaying these signals in panel (g), the intensity peaks in the traNSOM signal correspond to the minima in the cNSOM signal.

In this experiment, the intensity profiles of the traNSOM scans for both the fundamental and first excited modes follow the expected profiles; with a

maximum at the center of the fundamental mode and a minimum at the center

that is flanked by maxima on either side for the first order mode. With the

cNSOM scans, in locations where maxima are expected, minima are detected.

However, when the traNSOM scan is overlayed above the corresponding

cNSOM scan, these minima correspond to traNSOM maxima. We can conclude

that as the tip scans above the PhCnB, light is scattered, which decouples the

resonator from the bus waveguide, increasing the output intensity and

decreasing the amount of energy stored within the cavity. As was shown in the

simulations in Chapter II, the amount of light that is scattered depends on the

local field intensity. So, as the tip scans across locations of higher field intensity

the decoupling increases. This has a knock-on effect with the cNSOM signal.

When the tip is located at the edge of the PhCnB in an area with a relatively

weaker near-field, there is a strong cNSOM signal, and as the tip moves over

areas of high field, less energy is stored within the cavity resulting in significantly

less signal for the probe to collect.

In this case, the act of measuring is detrimental to the cNSOM scan

above the PhCnB. It is impossible to obtain an accurate representation of the

near-field signal only by looking at collected light through the probe. The

traNSOM signal _must_ be used to study the near-field profile of this device. This

is the reason that the experimental measurements described in Section 3.3

failed. For far-field measurements or ones of non-resonant devices, cNSOM is a

viable option, however, as soon as the PIC becomes more sensitive to near-field

perturbations, a smaller, less perturbing apertureless tip and traNSOM scan is

required.

[1] M. Knoll. "Aufladepotentiel und Sekundäremission elektronenbestrahlter Körper," *Zeitschrift für Tech. Phys*. **16** 467–475 (1935)

[2] G. Binnig and H. Rohrer. "SCANNING TUNNELING MICROSCOPY," *Surface. Sci*. **126** 236–244 (1983)

[3] G. Binnig, C.F. Quate and C. Gerber "Atomic Force Microscope," *Phys. Rev. Lett*. **56** (9) 930–933 (1986)

[4] H. Edwards, L. Taylor, W. Duncan and A.J. Melmed. "Fast, high-resolution atomic force microscopy using a quartz tuning fork as actuator and sensor," *J. App. Phys*. **82** 980–984 (1997) doi: 10.1063/1.365936

[5] Y.M. Calm, L. D'Imperio, N.T. Nesbitt, J.M. Merlo, A.H. Rose, C. Yang, K. Kempa, M.J. Burns, and M.J. Naughton. "Optical confinement in the nanocoax: coupling to the fundamental TEM-like mode," *Opt. Exp.* **21** (12) 32152 (2020) doi: 10.1364/OE.402723

[6] M. Abashin, U. Levy, K. Ikeda and Y. Fainman, "Effects produced by metal-coated near-field probes on the performance of silicon waveguides and resonators," *Opt. Lett.* **32** (17) 2602-2604 (2007) doi: 10.1364/OL.32.002602

[7] S. Mujumdar, A.F. Koenderink, T. Sünner, B.C. Buchler, M. Kamp, A. Forchel, and V. Sandoghdar. "Near-field imaging and frequency tuning of a high-*Q* photonic crystal membrane microcavity," *Opt. Exp.* **15** (25) 17214-17220 (2007) doi: 10.1364/OE.15.017214

[8] I. Cestier, D. Gready, U. Ben-Ami, G. Einstein, S. Combrie, Q. Tran and A. de Rossi. "Near Field Imaging of a GaAs Photonic Crystal Cavity and Waveguide Using a Metal Coated Fiber Tip," *Opt. Exp.* **17** (17) 15274-15279 (2009) doi: 10.1364/OE.17.015274

[9] P. Achmari, A.M Siddiquee, G. Si, J. Lin, B. Abbey, and S. Kou. "Investigating the probe-tip influence on imaging using scanning near-field optical microscopy," *OSA Cont.* **4** (4) 1143-1154 (2021) doi: 10.1364/OSAC.415810

[10] P. Achmari, A.M Siddiquee, G. Si, J. Lin, B. Abbey, and S. Kou. "Cloaked near-field probe for non-invasive near-field optical microscopy," *Optica* **9** (7) 1143-1154 (2021) doi: 10.1364/OPTICA.449216

[11] B. le Feber, J.E. Sipe, M. Wulf, L. Kuipers, and N. Rotenberg. "A full vectorial mapping of nanophotonic light fields," *Light Sci. Appl.* **8** (28) (2019) doi: 10.1038/s41377-019-0124-3

[12] M. Tzur, B. Desiatov, I. Goykhman, M. Grajower, and U. Levy. "High resolution direct measurement of temperature distribution in silicon nanophotonics devices," *Opt. Exp.* **21** (24) 29195-29204 (2013) doi: 10.1364/OE.21.029195

[13] M. Grajower, B. Desiatov, I. Goykhman, L. Stern, N. Mazurski and U. Levy. "Direct observation of optical near field in nanophotonics devices at the nanoscale using Scanning Thermal Microscopy," *Opt. Exp.* **23** (21) 27763-27775 (2015) doi: 10.1364/OE.23.027763

[14] K. Fritz and H. Rainer "Near-field microscopy by elastic light scattering from a tip," *Phil. Trans. R. Soc. A.* **362** 787-805 (2004) doi: 10.1098/rsta.2003.1347

[15] J.T. Robinson, S.F. Preble and M. Lipson "Imaging highly confined modes in sub-micron scale silicon waveguides using Transmission- based Near-field Scanning Optical Microscopy," *Opt. Exp.* **14** (22) 10588-10595 (2006) doi: 10.1364/OE.14.010588

[16] J.T. Robinson, S.F. Preble and M. Lipson "Imaging highly confined modes in sub-micron scale silicon waveguides using Transmission- based Near-field Scanning Optical Microscopy," *Opt. Exp.* **14** (22) 10588-10595 (2006) doi: 10.1364/OE.14.010588

[17] https://www.sutter.com/MICROMANIPULATION/mp225a.html

[18] Marketing Team "Why Do Tuning Fork Crystals Always Have A Frequency of 32.768 kHz?" jauch.com accessed 3/27/24 www.jauch.com/blog/en/tuning-fork-crystal-frequency-32768-khz/

[19] www.digikey.com

[20] "GlobalFoundries" europractice-ic.com accessed 3/27/24 europractice-ic.com/technologies/photonics/globalfoundries/

[21] K.R. Williams and R.S. Muller. "Etch Rates for Micromachining Processing," *J. Microelectromechanical Sys.* **5** (4) 256-269 (1996) doi: 10.1109/84.546406

[22] Addison Engineering, inc. "Silicon Dioxide - Thermally Grown TOX," *www.addisonengineering.com* Mar 28 2024 irp-cdn.multiscreensite.com/934e04a5/files/uploaded/ColorChart_SiliconDioxide.pdf

[23] MathWorks. "lsqcurvefit" www.mathworks.com Mar 28 2024 www.mathworks.com/
help/optim/ug/lsqcurvefit.html

Chapter IV

3D cNSOM scan of a polarization-insensitive 1D grating coupler based on a zero birefringence sub-wavelength "corelet" waveguide

4.1 Introduction

This Chapter describes work conducted in conjunction with the Popovič group in the Electrical Engineering Department at Boston University. This work, led by Dr. Bohan Zhang, was published in Optics Letters in 2022 [1], presented at CLEO in 2022 [2], and discussed in his thesis [3]. In this Chapter, we will describe the 3D NSOM scan used to characterize the beam profile of a polarization-insensitive 1D grating coupler (GC) (PIGC) based on a zero-birefringence sub-wavelength "corelet" waveguide. The purpose of these scans is to demonstrate that similar beam angles and profiles are emitted from the GC for both TM and TE polarizations.

Optical fiber-to-chip coupling is critical for proper implementation and characterization of PIC devices. I/O for data links requires some from fiber-to-chip coupling, while design and fabrication can be dramatically simplified and costs reduced if macroscale sources and detectors are fiber-coupled off-chip rather than included in a monolithic PIC chip. The two most common types of coupling devices are edge couplers and vertical GCs. Edge couplers, as the name suggests, are located on the edge of the chip, in-plane with PIC devices. Edge couplers are typically efficient over a wide-bandwidth (~ a few dB over 100 nm wavelength) and relatively polarization-insensitive [4]. However, they are

intrinsically limited due to their location on a CMOS chip. With edge couplers being on the side of the chip, some form of post-processing is required to access them, meaning spot checking in a foundry for quality control purposes would be challenging. Additionally, packaging of the chip within a larger architecture would always be limited by the location of the edge coupler and would dramatically limit the possible number of inputs and outputs compared to a vertical GC. The typical size of an edge coupler is much larger than a GC as well, taking up valuable real estate on the chip. For these main reasons, GCs are often preferable to edge couplers for optical I/O. GCs can also used in other applications, such as the manipulation of ion qubits [5] and mode shaping for orbital momentum generation [6,7].

4.2 Design and fabrication

With these benefits come inherent limitations due to fabrication and design constraints. The most basic model of a GC is to treat each Si piece as an antenna that is a point-like scatterer. Controlling the size and pitch of these antennas determines the intensity, direction, and shape of the emitted beam. To understand this further, let's look to Figure 4.1, which depicts a side view of a GC. Light guided by the waveguide scatters off each antenna, which acts as a point-like scatterer. Constructive interference from the radiated light off of the antennas forms a new wavefront at an angle θ relative to the surface normal. With the simplest form of lithography only allowing 1d arrays in the *x-z* or *y-z* planes and 2d arrays in the *x-y* plane, there is vertical symmetry and, therefore, bi-directional emission from the GC, which can be coupled to an optical fiber
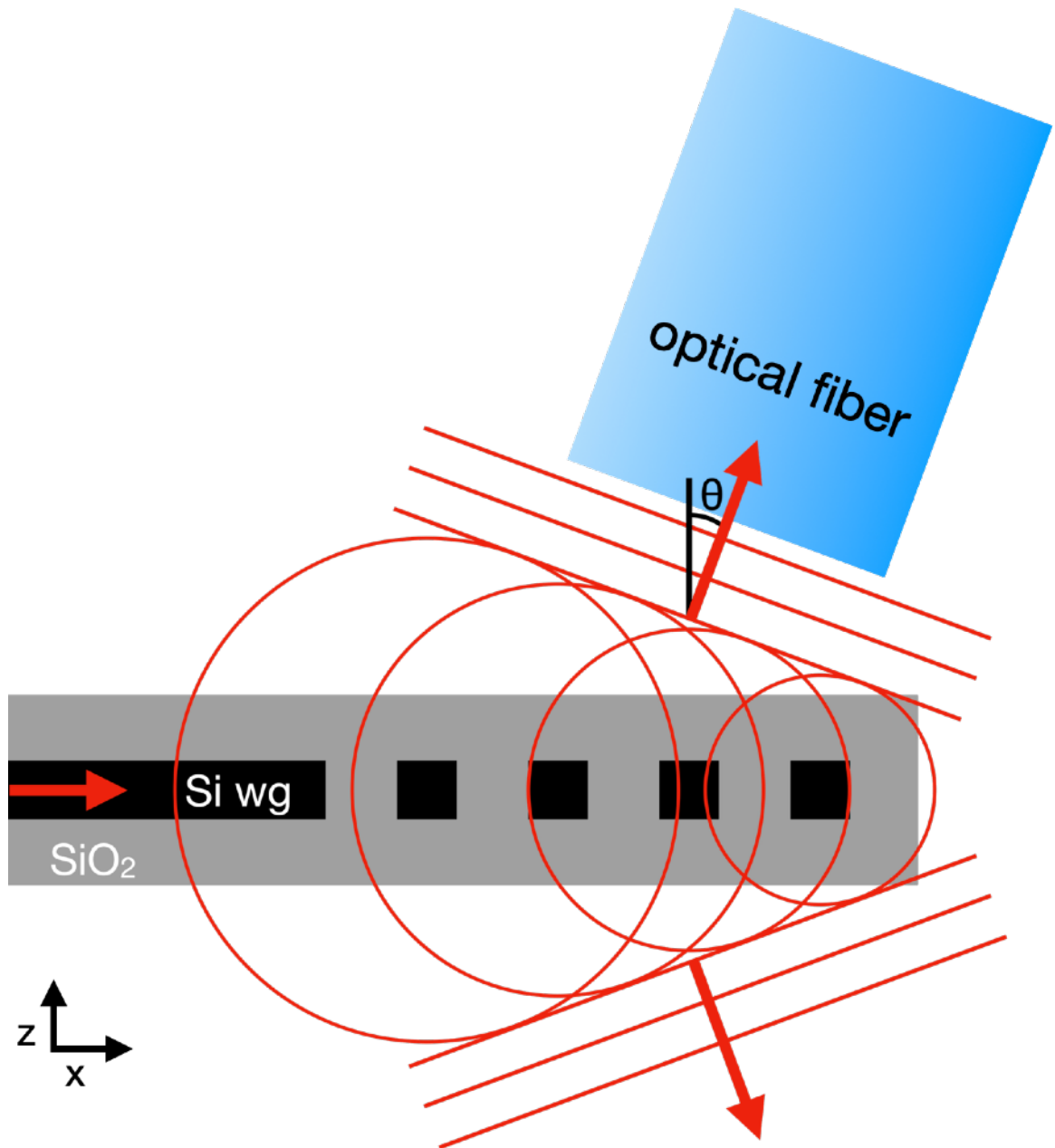
Figure 4.1 Cartoon of GC function.
Red arrows depict direction of light propagation. Red lines demonstrate the radiated light from each individual antenna and the wavefronts generated from their constructive interfaces. Here θ is the angle of emission relative to the surface normal.
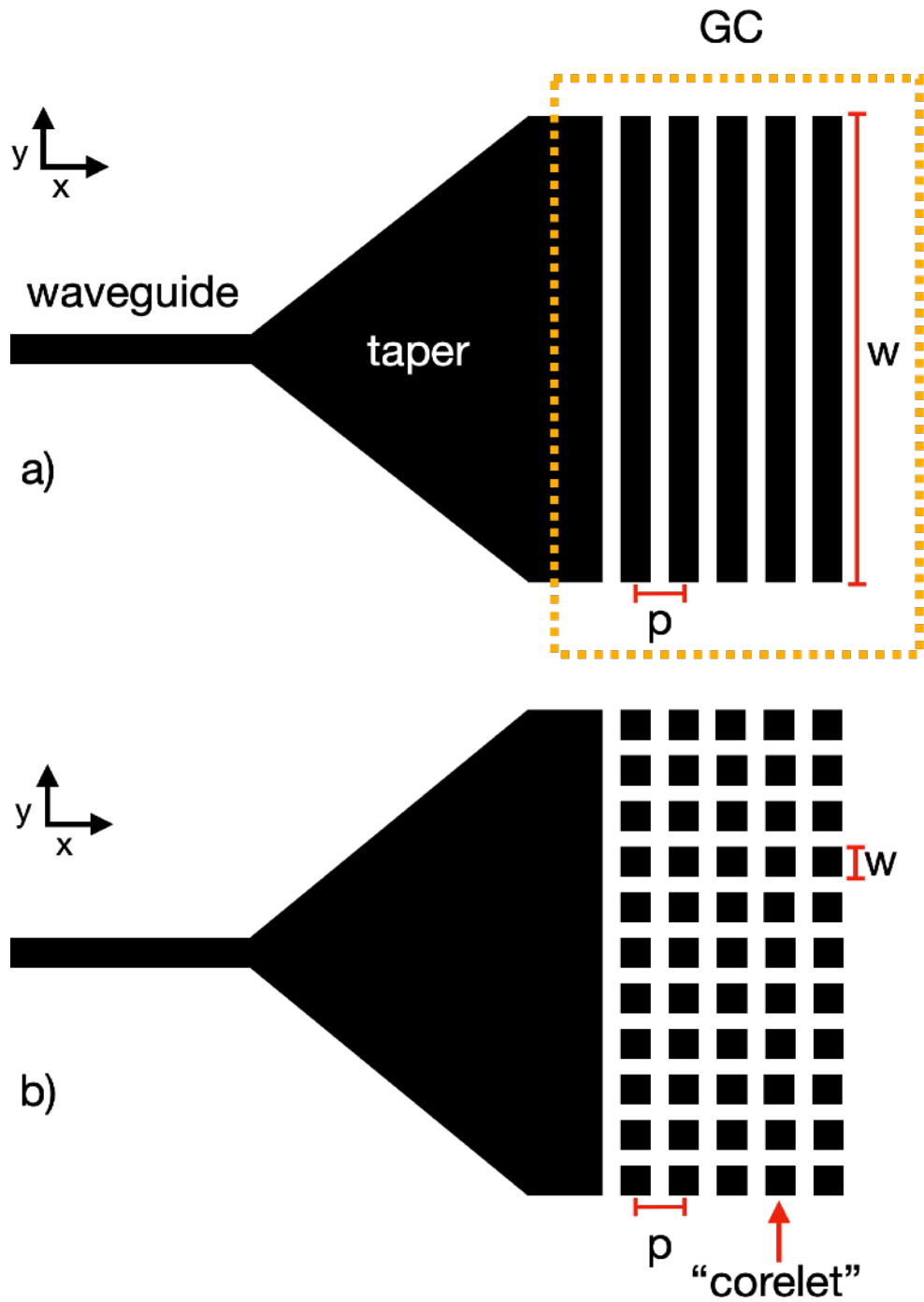
Figure 4.2 Comparison of "traditional" GC and zero-birefringence "corelet."
(a) cartoon of "traditional" 2d grating coupler with width w >> h (out of plane height).
(b) Polarization insensitive "corelet"waveguide with w ~ h.

either above or below the GC. This vertical symmetry can be broken with a dual layer approach, a reflective layer below the the GC or changing the shape of the individual Si "antennas".

Another limitation of the standard grating coupler design its polarization dependent characteristics. Figure 4.2 (a) depicts a standard waveguide design in which the waveguide width w is much greater than the height (coming out of the page). This situation leads to a modal birefringence where $n_{eff,TE} > n_{eff,TM}$. This can cause issues when using GCs as data interconnects in which polarization state is often unknown due to polarization wander in fibers. To rectify this, researchers have designed multi-layer GCs [8], non-uniform GCs [9] and an adaptive genetic algorithm-based GC [10]. This work is based on a much more simple concept.

Rather than utilizing one large slab-style waveguide as in Figure 4.2 (a), the horizontal slabs are broken up into sub-wavelength "corelets". The idea is that since $n_{eff,TE} < n_{eff,TM}$ for $w << h$, which is the opposite of the w>> h case, there should be an intermediate w:h ratio for which $n_{eff,TE} \approx n_{eff,TM}$. Using this theory, a GC is designed with "corelets" such that w = 235 nm, h = 240 nm with a gap of 105 nm between them, which should yield near zero birefringence in the O-Band. The GC has a uniform pitch "p" of 850 nm with a 60% duty cycle. The total width of the GC is chosen to be 6 μm to maximize the field overlap with the larger beam size of a 5-μm mode-field-diameter fiber. The chip is

fabricated using the GlobalFoundries 45 nm CLO process and flip chip/ substrate removal post processing is used to gain optical access to the PICs.

4.3 3D cNSOM scan

A 3D cNSOM scan is used to help characterize the angle and profile of the emitted TE and TM beams at 1300 and 1315 nm wavelengths. A 150 nm diameter aperture, metal-coated, pulled-fiber NSOM probe and FEMTO OE-200-NE detector are used to conduct the scans. To assure that either TE or TM polarization are being injected into the circuit, another either TM or TE polarization-dependent PIC is used to optimize coupling parameters before moving to a back-to-back PIGC circuit. All scans are 30 x 30 µm with 100 nm resolution in *x-y,* with the first being completed on the BOX surface. Since the BOX was *not* etched, there were still several µm separating the probe from the GC. Therefore, all light that is collected by the cNSOM aperture is propagating far-field light and we don't have to be concerned that the presence of the cNSOM probe is distorting the near-field. Once the initial scan on the chip surface is completed, the tip is retracted 476 steps in the *z* direction and another scan is made. This sequence is completed two more times with the results for both TE and TM polarizations of 1300 nm wavelength shown in Figure 4.3 and 1315 nm wavelength in Figure 4.4.

Looking first at the 1300 nm scans, as the tip retracts from the surface, the intensity profile of the beam spreads out. The profile is more circularly shaped for the TE polarization, while the TM profile is more of an ellipse. In the comparison, we can see that as z increases, the beams follow roughly the same
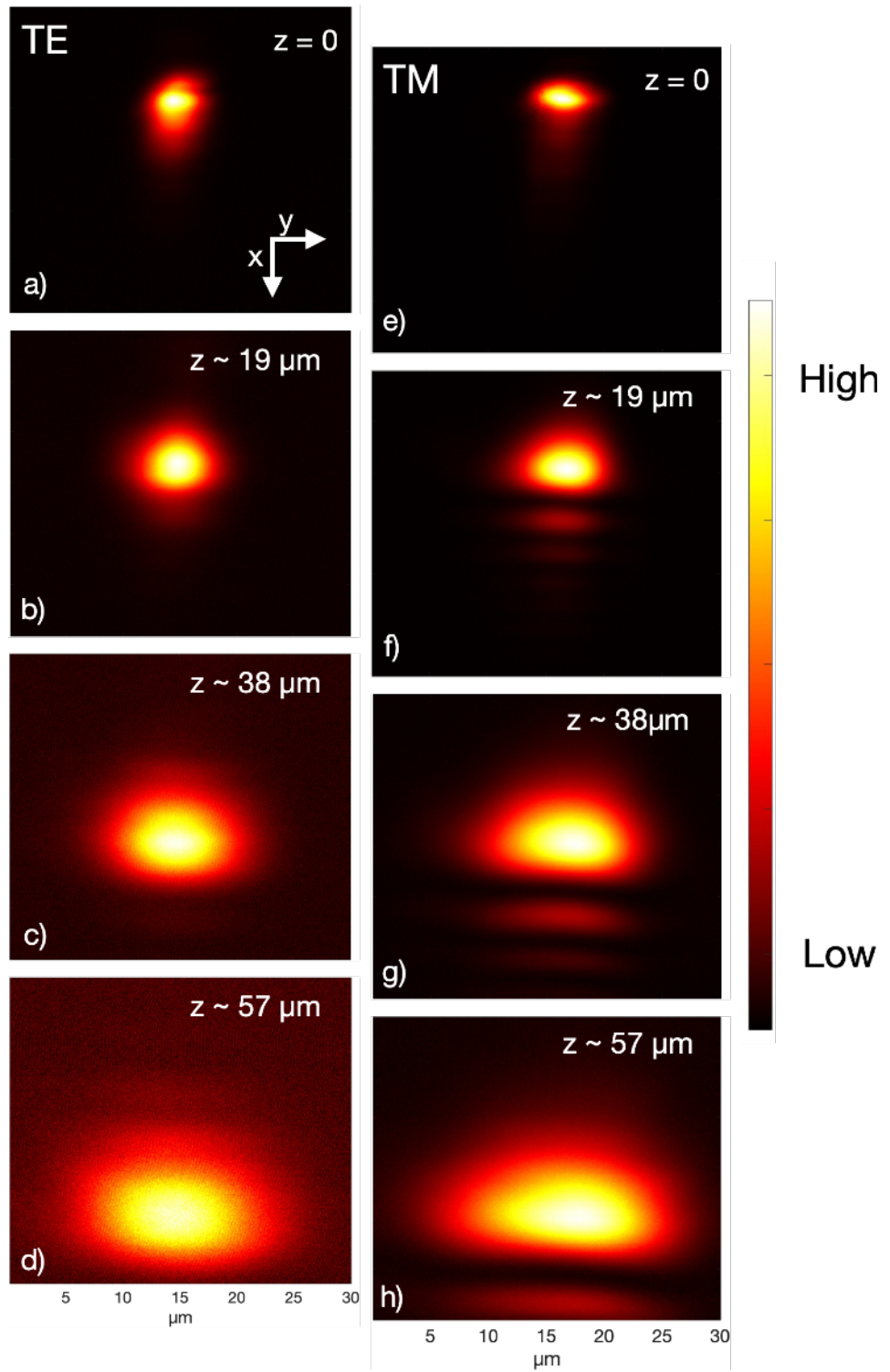
Figure 4.3 3D cNSOM scans of TE and TM beam profiles at 1300 nm.
(a-d) TE polarization and (e-h) TM polarization at 0 μm, 19 μm, 38 and 57 μm above
the chip surface. Color corresponds to optical intensity, with high and low intensities
labeled on the scale.
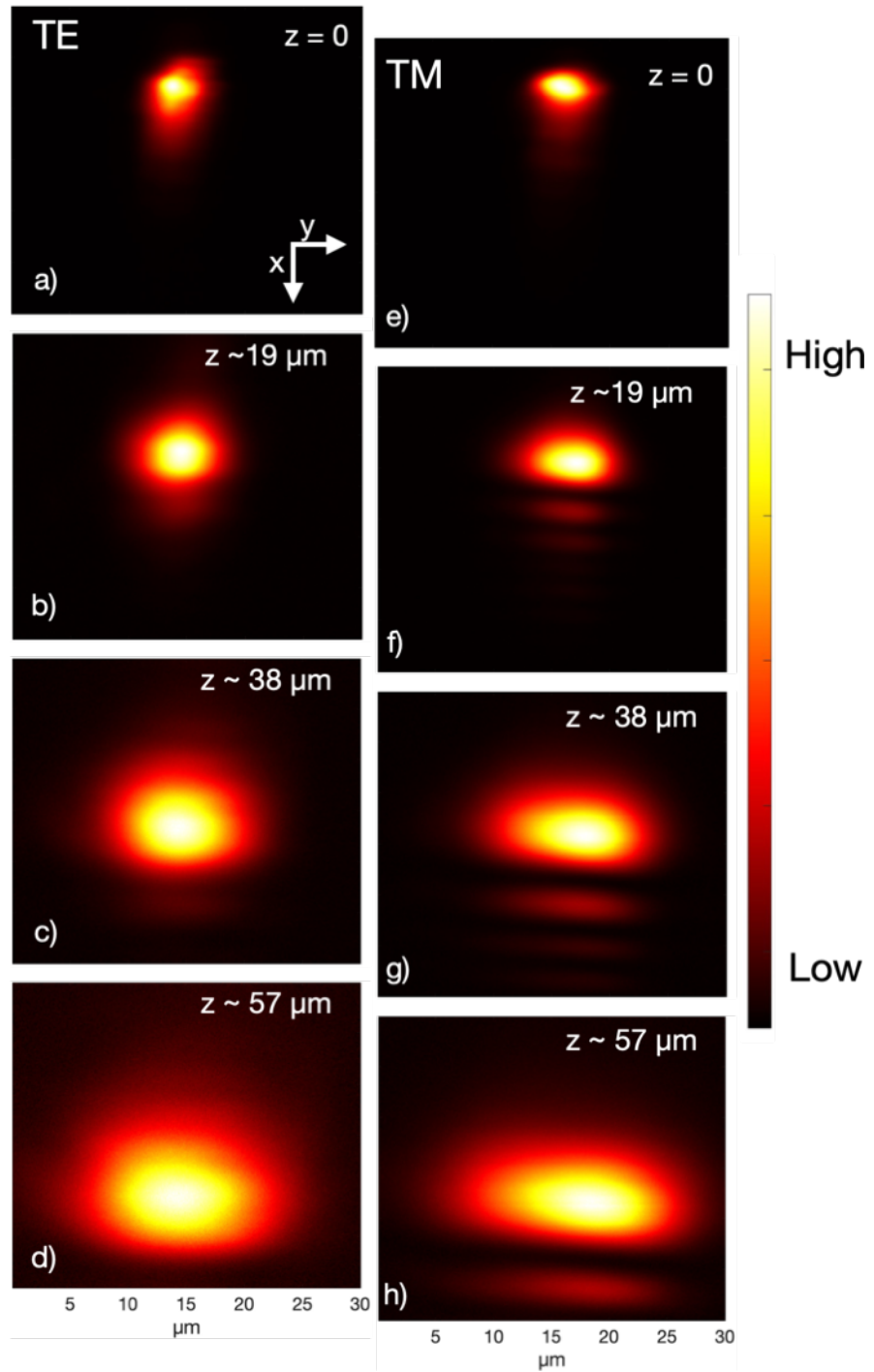
Figure 4.4 3D cNSOM scans of TE and TM beam profiles at 1315 nm.
(a-d) Intensity of TE polarization and (e-h) TM polarization at 0 μm, 19 μm, 38 μm and 57 μm above the chip surface. Color corresponds to optical intensity, with high and low intensities labeled on the scale.

119

trajectory. The same analysis holds true for the 1315 beams.

4.4 Conclusion

A PIGC design based on "corelet" waveguides that creates a zero-birefringence condition in the O-band is fabricated, with the beam profile and angle measured using a 3D cNSOM. The cNSOM scans confirmed with other data collected in Ref. [1] that angles and profiles for the two polarizations were similar; resulting in an impressive 73 nm bandwidth across the O-band for the $\pm$ 1dB polarization dependent loss. Though more iterations can be made to improve the overlap between the two beam profiles, these results are promising for this relatively simple technique of sub-wavelength "corelets". Since the probe was more than a few μm from the sample and not perturbing the near-filed, cNSOM measurements can be used for super-resolution imaging, far beyond the capacities of a traditional optical microscope.

[1] B. Zhang, M. Schiller, K. Al Qubaisi, D. Onural, A. Khilo, M.J. Naughton and M.A. Popović "Polarization-insensitive 1D grating coupler based on a zero-birefringence subwavelength corelet waveguide," *Opt. Lett.* **47** (13) 3167-3170 (2022) doi: 10.1364/OL.459306

[2] B. Zhang, M. Schiller, K. Al Qubaisi, D. Onural, A. Khilo, M.J. Naughton, and M.A. Popović, "Polarization-Insensitive One-Dimensional Grating Coupler Demonstrated in a CMOS-Photonics Foundry Platform," *Conference on Lasers and Electro-Optics, Technical Digest Series* paper JTh3A.46 (2022)

[3] B. Zhang, "Design of high performance radiative and resonant silicon photonic devices by efficient control of light propagation and radiation," (Doctoral dissertation, Boston University, 2023) Permanent Link: https://hdl.handle.net/2144/45485

[4] T. Barwicz, B. Peng, R. Leidy, A. Janta-Polczynski, T. Houghton, M. Khater, S. Kamlapurkar, S. Engelmann, P. Fortier, N. Boyer, and W.M.J. Green, "Integrated Metamaterial Interfaces for Self-Aligned Fiber-to-Chip Coupling in Volume Manufacturing," *IEEE J. Selected Topics Quant. Elec.*, **25** (3) 1-13 (2019) doi: 10.1109/JSTQE.2018.2879018

[5] R. J. Niffenegger, J. Stuart, C. Sorace-Agaskar, D. Kharas, S. Bramhavar, C. D. Bruzewicz, W. Loh, R. T. Maxson, R. McConnell, D. Reens, G. N. West, J. M. Sage, and J. Chiaverini, "Integrated multi-wavelength control of an ion qubit," *Nature*, **586** (7830) 538-542 (2020) doi: 10.1038/s41586-020-2811-x

[6] D. Zhang, X. Feng, and Y. Huang, "Encoding and decoding of orbital angular momentum for wireless optical interconnects on chip," *Opt. Express,* **20**(24) 26986-26995 (2012) doi: 10.1364/OE.20.026986

[7] N. Zhou, S. Zheng, X. Cao, Y. Zhao, S. Gao, Y. Zhu, M. He, X. Cai, and J. Wang, "Ultra-compact broadband polarization diversity orbital angular momentum generator with 3.6 x 3.6 μm^2 footprint," *Sci. Adv.,* **5** eaau9593 (2019) doi: 10.1126/sciadv.aau9593

[8] J.C.C. Mak, W.D. Sacher, H. Ying, X. Luo, P. Guo-Qiang Lo, and J.K.S. Poon, "Multi-layer silicon nitride-on-silicon polarization-independent grating couplers," *Opt. Exp.,* **26**(23) 30623-30633 (2018) doi: 10.1364/OE.26.030623

[9] J.H. Song, F.E. Doany, A.K. Medhin, N. Dupuis, B.G. Lee, and F.R. Libsch, "Polarization-independent nonuniform grating couplers on silicon-on-insulator," *Opt. Lett.,* **40**(17) 3941-3944 (2015) doi: 10.1364/OL.40.003941

[10] X. Wang, H. Yu, Q. Huang, Z. Zhang, Z. Zhou, Z. Fu, P. Xia, Y. Wang, X. Jiang, and J. Yang, "Polarization-independent fiber-chip grating couplers optimized by the adaptive genetic algorithm," *Opt. Lett.,* **46**(2) 314-317 (2021) doi: 10.1364/OL.413307

Chapter V

High resolution NSOMs of optical microring resonators

5.1 Introduction

This Chapter describes work conducted in conjunction with the Popovič group in the Electrical Engineering Department at Boston University. This work is planned to be submitted in 2024 [1] with similar research having been presented by Dr. Kenaish Al Qubaisi at CLEO in 2022 [2]. In this Chapter, we will present both cNSOM and traNSOM scans used to achieve first of their kind, high resolution near-field scans of a photonic ring resonator on a monolithic integrated photonics-electronics chip. The resolution of the the traNSOM scan is high enough that the fringes resulting from constructive interference within the resonant ring can be resolved. This work serves as a proof of concept for combining traNSOM procedure and novel BOX etching that allows for precise control of the tip induced perturbation, resulting in minimally invasive and high resolution near-field maps.

Microring resonators are an essential building block for PICs. For example, wavelength division multiplexed (WDM) optical interconnects which rely on microring modulators have shown great promise and have already begun to supersede their electronic counterparts. Despite their ubiquity in PICs, near-field characterization of microring resonators has remained a challenge to researchers. As discussed in Section 3.3, the central issue is that traditional cNSOM measurements generate a large perturbation that is detrimental to the operation of the resonator that is being measured. Proper near-field scanning

requires a decrease in the magnitude of the tip-induced perturbation. This can be done in two ways; increasing the tip-device separation or reducing the volume of the tip. In this Chapter, we will explore both of those avenues in the quest for reliable, high resolution near-field imaging of microring resonators.

5.2 Design and fabrication

The particular ring we are measuring is a passive "spoked ring" modulator, as seen in Figure 5.1. Following previous work from the Popović group [3], the ring is specifically designed to be fabricated in a standard complementary metal-oxide-semiconductor (CMOS) process without any modifications. Although we will be NSOM imaging a passive version of the modulator, the active version operates via index modulation with spoke-like, lateral p-n junctions controlled with electrical contacts. The width of the ring is greater than that of fundamental mode so that the electrical contacts, located at the center of the ring, don't interfere with the resonant field. "Pulley-style" evanescent couplers between the bus waveguide and microring increase the interaction length, in an attempt to suppress the higher order modes [4]. However, we can see that they are diminished but still present in Figure 5.3 (a). The ring has an outer radius of 4.5 μm. This PIC is fabricated using the GlobalFoundries 45 CLO process. As it arrives, the PIC device layer is at the bottom of the chip just above the Si wafer, so a flip-chip procedure and subsequent substrate removal with Xe_2F etching are employed to gain optical access to the PICs (as described in section 3.7). To gain access to the near-field and control the tip-sample interaction, an additional oxide etching step with
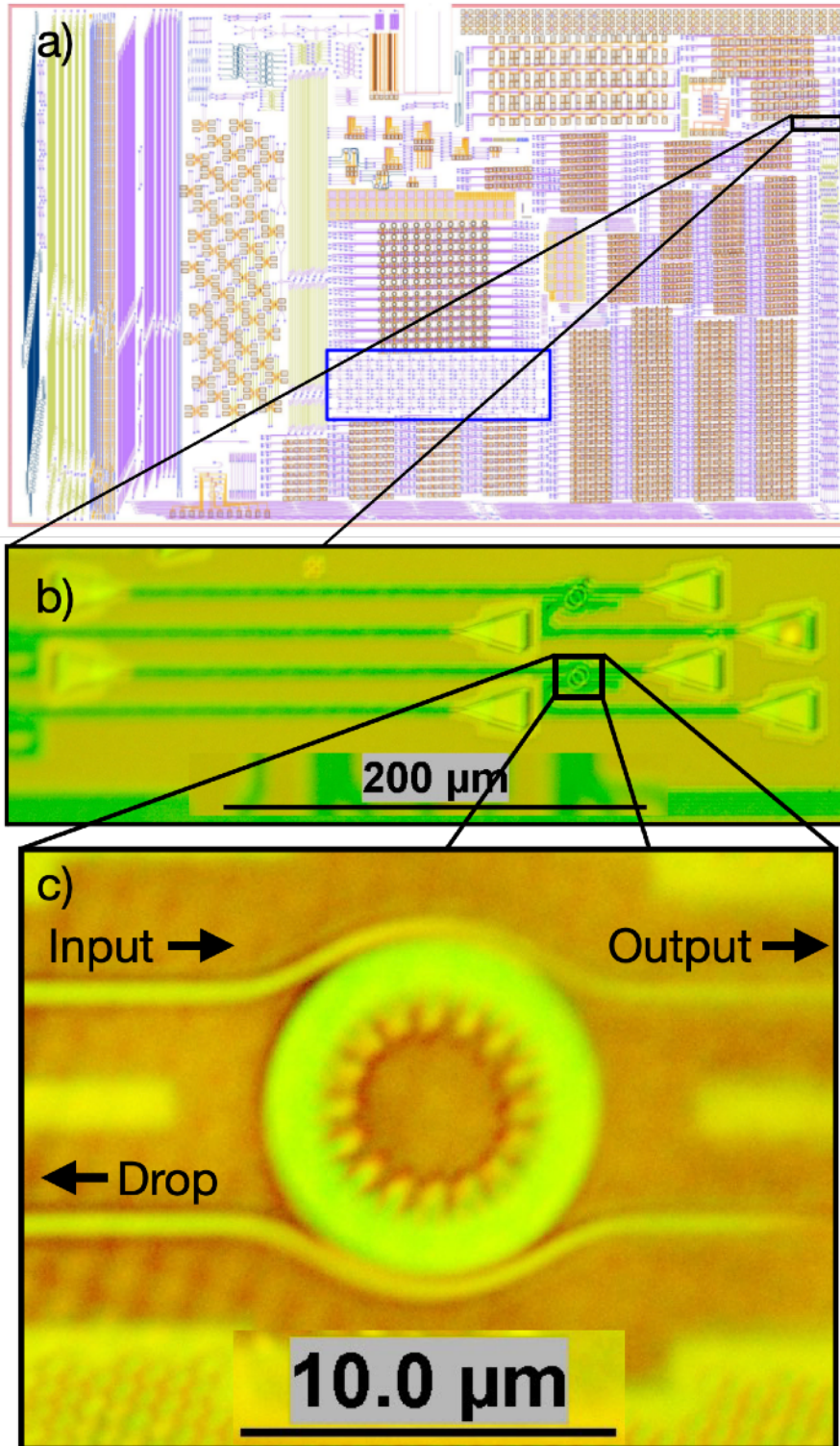
Figure 5.1 Location and optical micrographs of spoked ring resonator.
(a) Layout of PIC chip. (b) Optical micrograph of entire circuit. (c) Optical micrograph of ring with labels for input output and drip port.

BOE is completed, with subsequent profilometry measurements to determine BOX thickness (also described in section 3.7).

5.3 cNSOM measurement of microring with an apertured probe

The purpose of this section is to describe why measurements using apertured probes was not pursued further and traNSOM measurements with apertureless probes were adopted. Measuring these sensitive photonic devices creates many issues. Certain steps, which compromised the integrity of the experimental design, had to be taken to compensate for these issues. As such, the purpose of the data displayed in Figure 5.2 is *not* to draw conclusions about the device itself, but instead, to explain the issues with conducting this measurement, and why an alternate approach with a more reliable experimental design was chosen.

I believe, at this point, it will be beneficial to tell a quick story about the inception of this project and early work to understand why this study was conducted and what we had hoped it would demonstrate. Originally, the Popović group reached out to Dr. Naughton in the hopes of conducting near-field measurements of resonant photonic devices. Our first attempts were of silicon on insulator (SOI) devices, with all but the bottom of Si waveguides exposed to air. We ran into several major issues when conducting cNSOM measurements of these devices. Most notably, the probes would often "bulldoze" the waveguides, there was a large disconnect between simulated and actual performance of the devices (likely caused by tolerance issues in fabrication), and, most worrying of all, touching the surface of the device with

the cNSOM probe would completely destroy device performance, only for it to be restored when the probe was removed from the surface. As discussed in section 3.8, the issue was that the tip-sample interaction was too large. We knew we needed to create some sort of tip-sample separation to rectify this issue. At first, we attempted to "levitate" the probe above the sample, but that proved challenging due to the lack of feedback that controls the z positioning of the NSOM tip and was dropped (although it could certainly be pursued in the future). Instead, a first of its kind BOX etching procedure, as described extensively in this thesis, was pursued. We had hoped that there would be a "Goldilocks" thickness t at which the probe would minimally interact with the sample, but still collect a significant amount of light. The experiment that we will discuss in this section proved to us that the "Goldilocks" t does not exist, and that an alternate approach (as described in section 5.4) would need to be explored.

For this cNSOM measurement, a 150 nm aperture is used with an oxide thickness t = 83 nm. The results are displayed in Figure 5.2. The presence of the probe greatly diminishes the r_e of the modulator, and increases the minimum transmittance to about 20%, however changes to the resonant frequency and Q appear to be minimal, although no larger study was conducted. In panel b we can see that, when scanned off resonance, the probe collects light from the bus waveguide (the top waveguide in 5.1 (c)) but does not collect light from either the ring or the drop port waveguide.
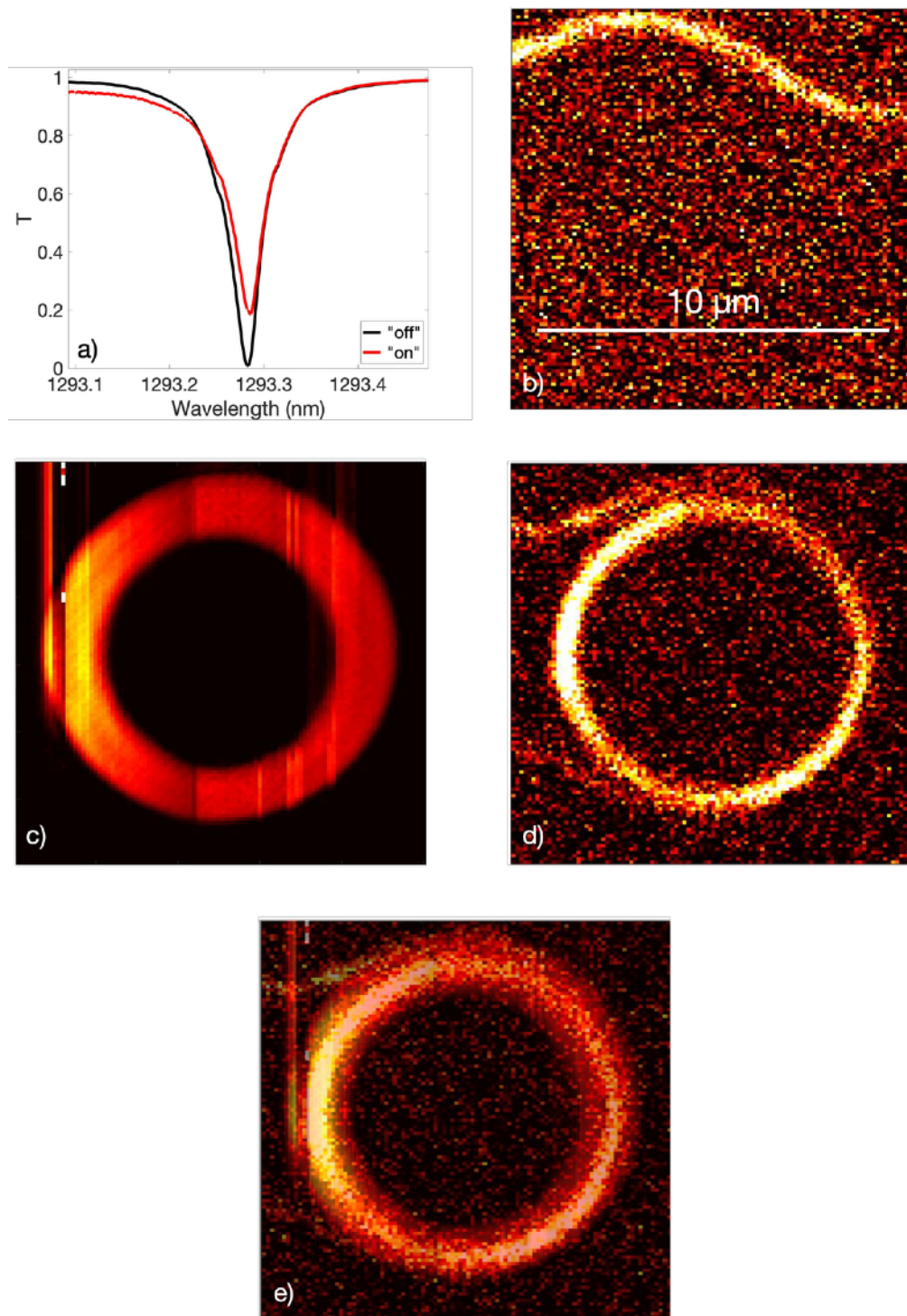
Figure 5.2 Combined cNSOM and traNSOM scan of microring resonator with 150 nm aperture probe.
(a) Spectral sweep of resonant mode with probe both on resonator "on" and far away from resonator "off" (b) cNSOM off resonance, (c) traNSOM and (d) cNSOM on resonance. (e) Overlay of traNSOM and cNSOM scans.

While the off-resonance scan is relatively straightforward, measuring on resonance is extremely challenging. The biggest issue is measurement-induced sample heating. Back in Section 3.4, we discussed how the strong field generated by ring resonators can heat near-field probes. The stronger the tip-filed interaction (either due to tip size or field intensity), the greater the heating. With the tip being heated by the field, the tip can then heat the sample, which would slightly increase the index of the Si [5] and the resonant wavelength of the modulator. If this heating is large enough, the tip will effectively modulate the resonance of the ring as it scans. Though the change is very slight, it is detrimental to a traNSOM or a cNSOM scan which depend on a constant amount of energy being stored in the ring at a pre-selected wavelength over the course of the scan. To compensate for this, rather than a constant wavelength being injected into the circuit, the input wavelength is slowly increased over the course of the scan to ensure that the resonant wavelength is always being used, and that a constant amount of energy is stored in the ring. I will re-iterate that this is not proper experimental design, but, nevertheless is necessary to conduct NSOM scans when the sample is being heated by the probe.

traNSOM and cNSOM results of the on-resonance scan can be seen in panels (c) and (d). When in the on-resonance state, the probe collects light from the ring as well as the input and drop port waveguides waveguides. As expected, no light is collected when scanning above the output. Looking at the traNSOM scan, the probe increases the output intensity when scanning above the ring, but no effect is seen when above the input, output or drop waveguides.

Overlaying the two scans in panel (e) reveals that the probe collects cNSOM light from the ring at the center of the perturbed area.

All of the NSOM scans have relatively low resolution, with little light being collected for the cNSOM scans and a large amount of perturbation in the traNSOM scan. Increasing the resolution of the cNSOM scan would require a smaller probe with a much stronger field or thinner t. These solutions, however, would increase the tip-sample interactions, which would be detrimental to device performance in the presence of a near-field probe and generate more unwanted heating effects. Given the issues outlined with this experiment, the decision was made to abandon the cNSOM scans and focus fully on increasing the quality of the traNSOM measurement by limiting the tip-sample interaction and probe induced heating.

5.4 traNSOM of PIC microring resonator

To increase the resolution of the near-field scan, a much smaller, apertureless 50 nm diameter metal-coated probe and another chip with a thicker 170 nm oxide layer is used. Spectral sweeps are plotted in Figure 5.3. There are four clearly visible fundamental mode resonances with much lower r_e higher order resonances also present. When the probe is on the surface, there is a very slight decrease in r_e but no detectible change in Q or λ'. Overall, the "on" and "off" curves look nearly identical, which is exactly what we would hope for. If the presence of the probe noticeably altered the resonance, this would throw the results of the scan into question. Since this is not the case, we can be confident that the field that is mapped looks nearly identical to the field without the probe.
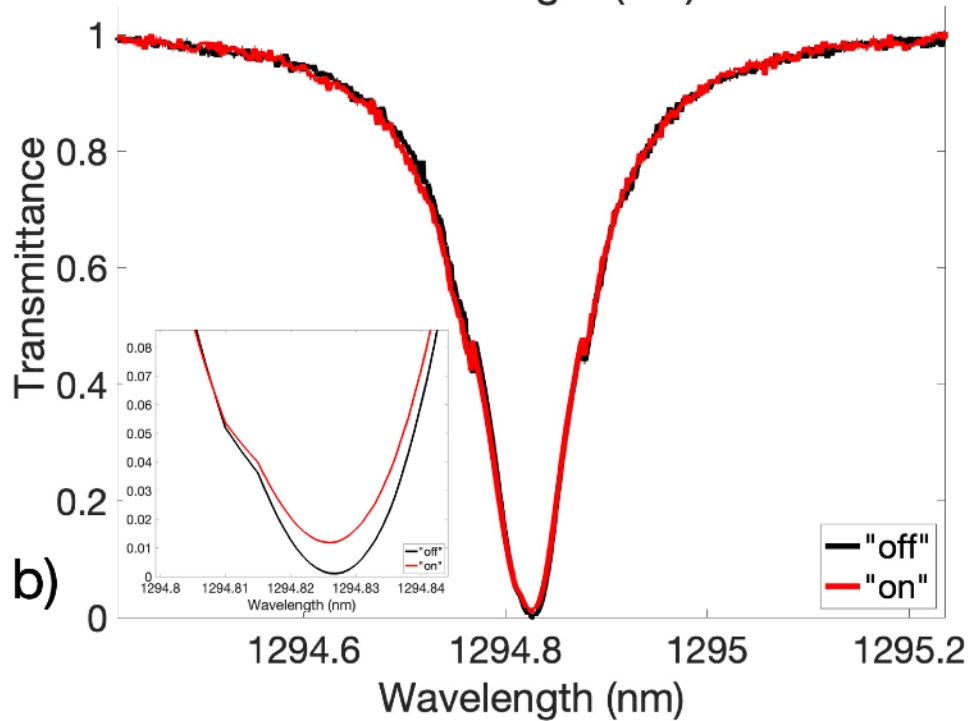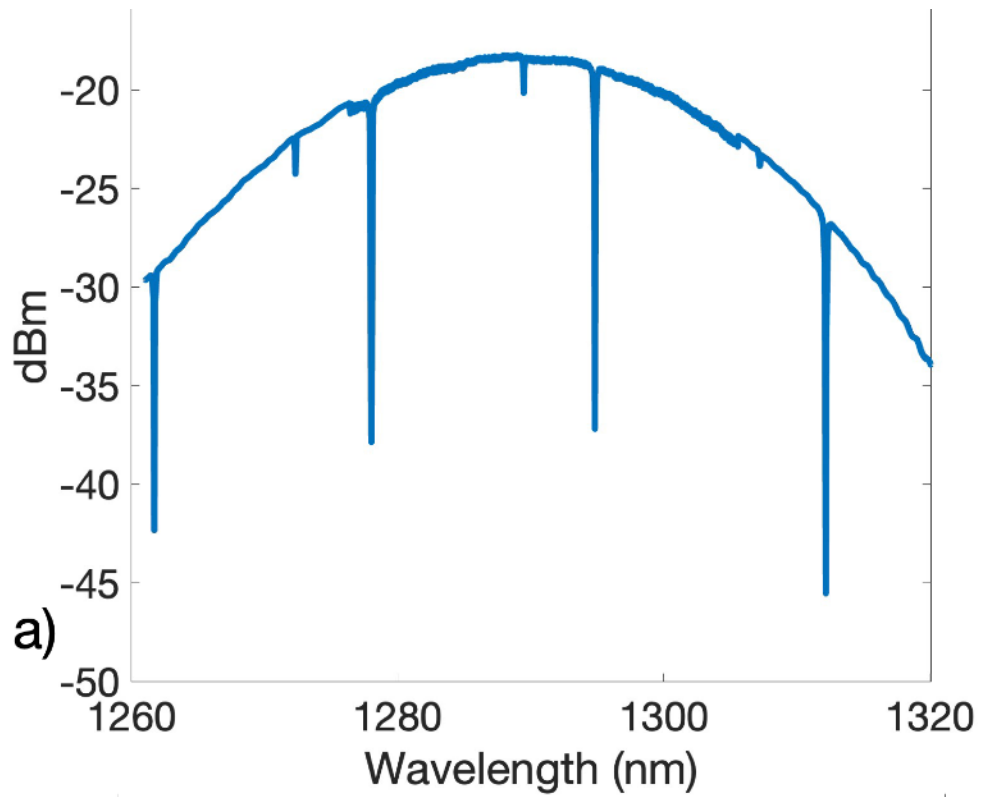
Figure 5.3 Spectral sweep of microring with and without apertureless probe.
(a) Spectral sweep without NSOM probe (b) Spectral sweep without the tip present
(black) and with the tip on the ring (red) with the inset being a zoomed in view of the
resonance.

131
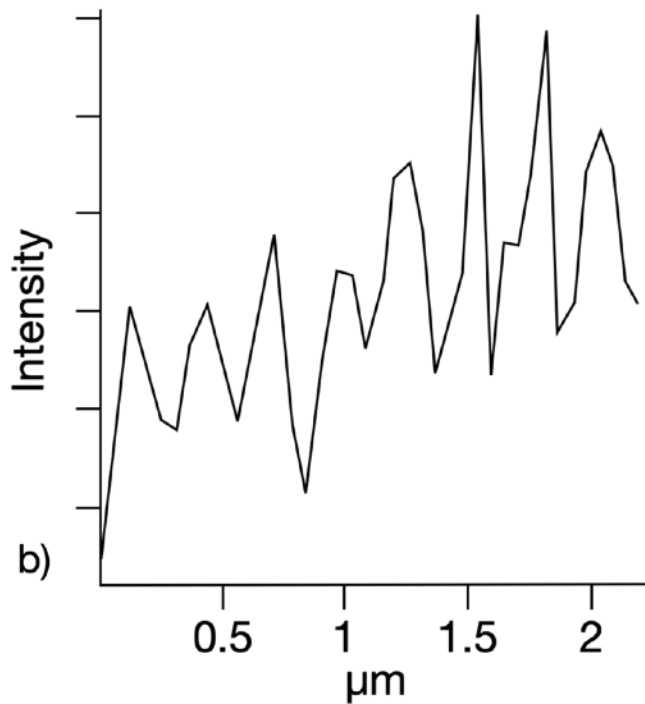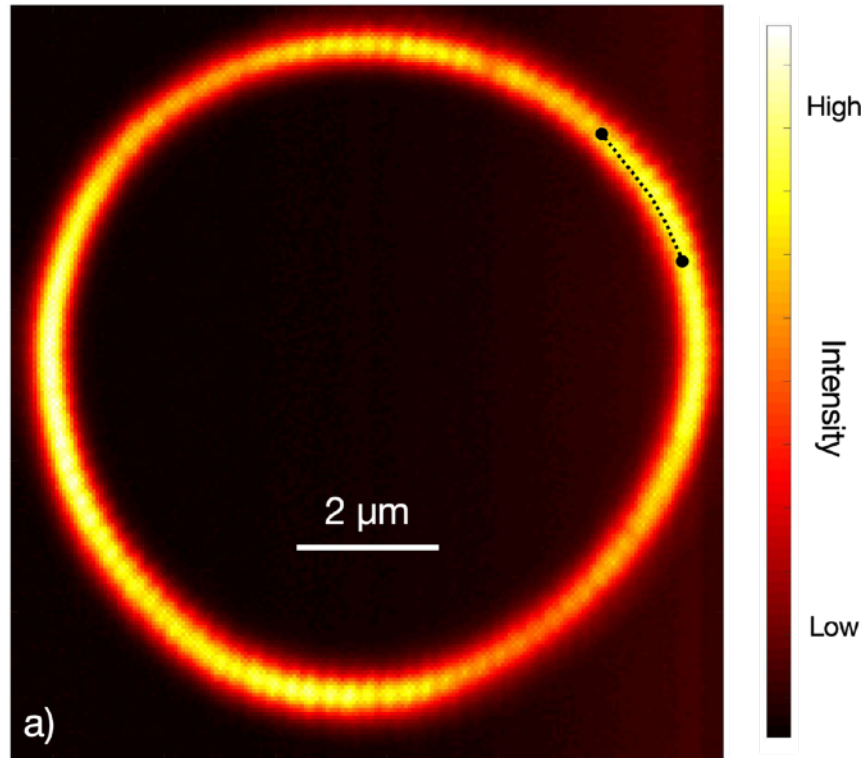
Figure 5.4 High resolution traNSOM scan of spoked ring with apertureless probe.
(a) traNSOM scan with 50 nm metal coated tip and t = 170 nm. (b) Intensity profile
from dotted line on (a).

Comparing with Figure 5.2 (a), the increase in r_e is dramatically reduced, further indicating a drastic reduction in the tip induced perturbation.

For the $\lambda' = 1294.831$ nm resonance, Q is $11.1 \times 10^4 \pm 100$. Results of the traNSOM scan at this wavelength are shown in Figure 5.4. As the probe scans above the surface of the ring, light is scattered and constructive interference within the ring decreases, which slightly decouples the ring and bus waveguide causing a reduction in r_e (i.e. an increase in output intensity). With such little light being transmitted to the output when on resonance, there is no detectible change in intensity when the probe is above the input or output waveguides. With the much smaller tip, the constructive interference fringes within the ring can now be seen. A profile taken through the dashed line in panel a is plotted in panel b. There is a clear periodic pattern to this data with a peak to peak distance of roughly 280 nm, which implies a wavelength of roughly 560 nm within the ring.

5.5 Conclusion

In this Chapter, we have described a simple yet effective method for high resolution near-field imaging of a passive spoked ring resonator with Q > 10k. We described why the technique implemented by others using cNSOM is not practical and yields comparatively low resolution images. We then demonstrated an alternative procedure with a thicker oxide and smaller probe, which yielded much higher resolution images with significantly less tip induced perturbations. As will be shown in Chapter VI this same procedure can be used for high resolution imaging of other resonant structures. The only modifications required

for high resolution imaging of other PIC devices is a tailoring of the tip-sample

separation t and selecting the correct probe diameter so that the desired tip-

sample interaction is achieved.

[1] M. Schiller, K. Al Qubaisi, B. Zhang, D. Onural, M.A. Popović, and M.J. Naughton, "High resolution near-field imaging of Q>10k Microring Resonators," *in preparation*

[2] K. Al Qubaisi, M. Schiller, B. Zhang, D. Onural, A. Khilo, M.J. Naughton, and M.A. Popović, "In-situ photonic circuit field characterization in electronics-photonics CMOS platform via backside flip-chip near-field scanning optical microscopy," *Conference on Lasers and Electro-Optics, Technical Digest Series* paper SM3N.1 (2022)

[3] J.M. Shainline, J.S. Orcutt, M.T. Wade, K. Nammari, B. Moss, M. Georgas, C. Sun, R. J. Ram, V. Stojanović, and M.A. Popović, "Depletion-mode carrier-plasma optical modulator in zero-change advanced CMOS," *Opt. Lett.* **38**(15), 2657-2659 (2013) doi: 10.1364/OL.38.002657

[4] E.S. Hosseini, S. Yegnanarayanan, A.H. Atabaki, M. Soltani, and A. Adibi, "Systematic design and fabrication of high-*Q* single-mode pulley-coupled planar silicon nitride microdisk resonators at visible wavelengths," *Opt. Exp.* **18**(3), 2127-2136 (2010) doi: 10.1364/OE.18.002127

[5] B.J. Frey, D.B. Leviton, and T.J. Madison, "Temperature-dependent refractive index of silicon and germanium," *Proc. SPIE 6273, Optomech. Tech. Astro.* 62732J (2006) doi: 10.1364/OE.18.002127 10.1117/12.672850

Chapter VI

traNSOM scans of a cubic-wavelength mode volume photonic crystal nanobeam cavity in a monolithic CMOS platform

6.1 Introduction

This Chapter describes work conducted in conjunction with the Popovič group in the electrical engineering department at Boston University. This work, lead by Dr. Kenaish Al-Qubaisi, was published in Optics Letters in 2023 [1] and discussed in his thesis [2]. In this Chapter, we will describe traNSOM scans used to characterize the mode profile of a cubic-wavelength mode volume photonic crystal nanobeam cavity (PhCnB) in a monolithic CMOS platform. These scans show strong agreement with the simulated E-field and confirms that the PhCnB does indeed confine this strong E-field to a small cubic wavelength V.

PhCs are a widely used because of their high Qs and small Vs, which are on the order of a cubic wavelength

$$V \sim \left(\frac{\lambda_m'}{n(\lambda_m')} \right)^3. \tag{6.1}$$

Though the first PhCs were of the 2D variety, more recently, 1D photonic nanobeam cavities (PhCnB) have grown in popularity. The ability to replace current microring based modulators with PhCnB modulators is a particularly appealing application. High performance optical interconnects currently utilize efficient, high speed, optical microring modulators which take up a relatively small footprint $\sim$ (5 μm^2) [3,4]. However, PhCnB based modulators are primed to replace microring modulators, because of their even smaller footprint, which will

allow for tighter packaging, and larger FSR. In this Chapter, we will describe the design and first of its kind, traNSOM characterization of PhCnBs intended for use as optical modulators.

6.2 Design and fabrication

A key limitation that had previously hindered PhCnBs and prevented wide-scale adoption of PhCnB modulators, was large reflections generated by the standing-wave based modulator. However, researchers have overcome this obstacle by using two PhCnBs with opposite mode symmetry [5]. When they are both evanescently coupled to a waveguide on opposing sides, symmetry-induced destructive interference will eliminate the reflection and render the transmission equivalent to that of an evanescently-coupled microring resonator. In Figure 6.1, cartoons of a pair of PhCnBs are shown with opposing symmetric (panel (a)) and anti-symmetric (panel (b)) architectures. Although these PhCnBs are intended to be used in tandem as one "reflectionless resonator unit," in this Chapter, we will characterize a lone antisymmetric PhCnB evanescently coupled to a bus waveguide, as shown in Figure 6.2.

The anti-symmetric PhCnB has a width "w" of 700 nm and a constant period "a" of 304 nm. Periodic gaps are formed by etching the entire width of the waveguide and filling the holes with a low index oxide. The mirroring strength of each hole depends on the duty cycle (percentage of "a" taken up by the hole width). By varying the duty cycle throughout the PhCnB distinct regions are created, the central cavity region and two mirror regions on either side. At the center of a symmetric PhCnB there are N_{cav} holes (and one fewer in the anti-
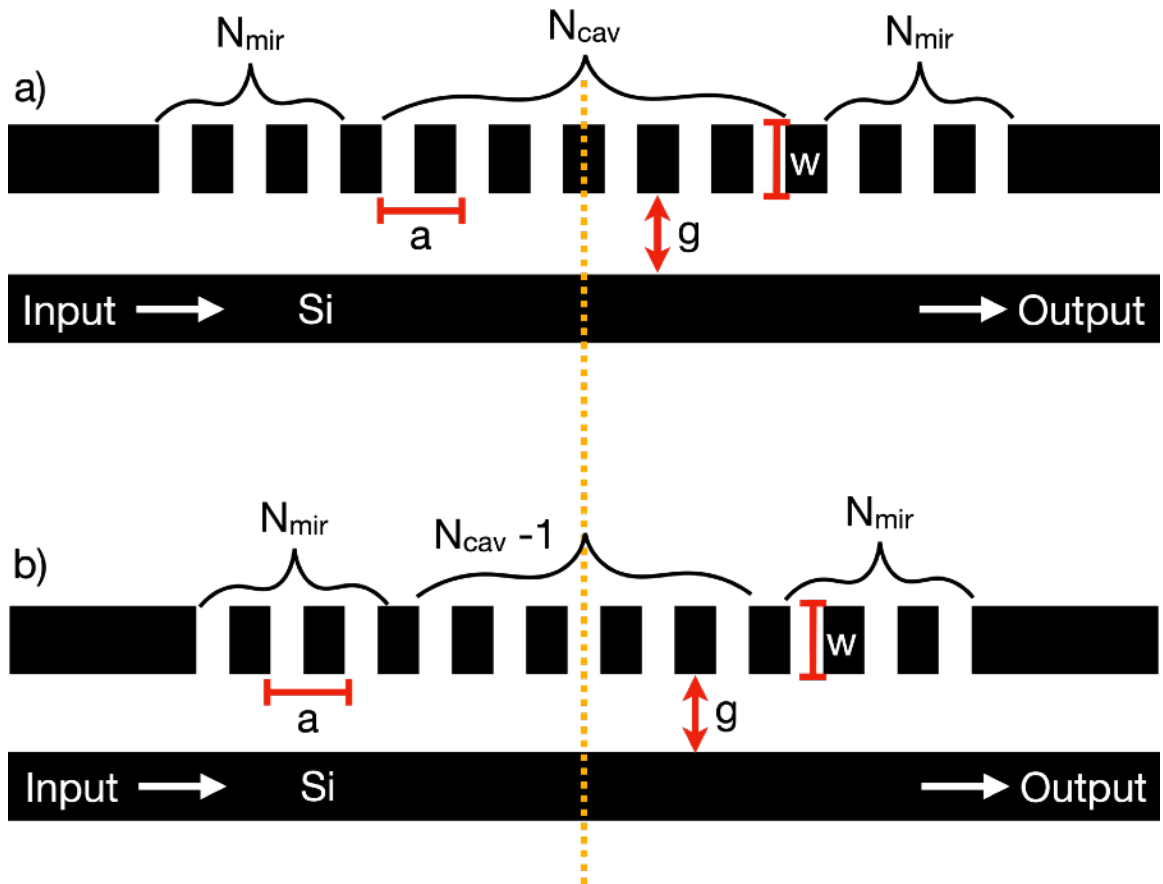
Figure 6.1 Cartoon of PhCnB design.
(a) Symmetric and (b) anti-symmetric cavities with periodic spacing *a*, gap *g*, and width *w* labeled. Light is input from the left and transmitted signal is output on the right.
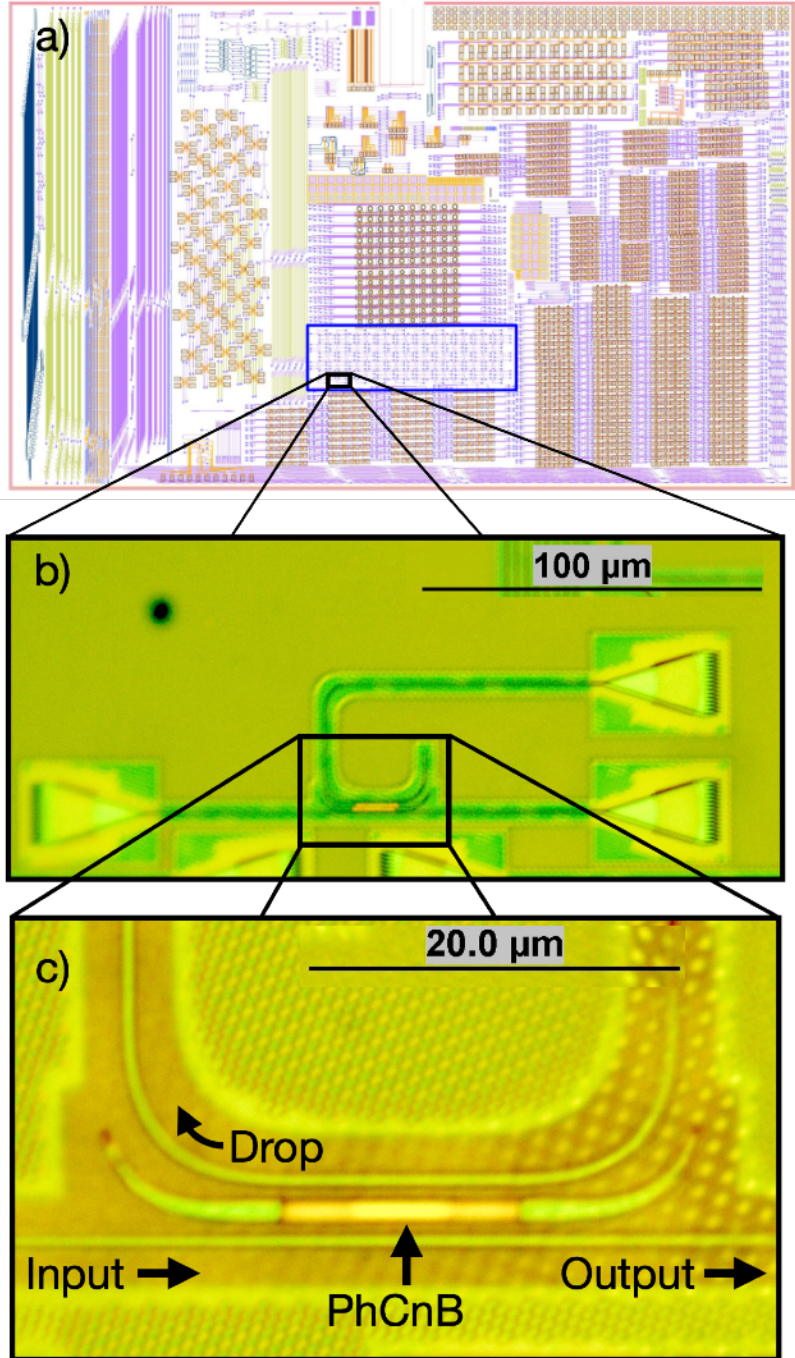
Figure 6.2 Location and optical micrographs of anti-symmetric PhCnB.
(a) Layout of PIC chip. (b) Optical micrograph of entire circuit. (c) Optical micrograph of PhCnB with labels for input output and drop port.

symmetric case). N_{mir} mirror holes with a constant duty cycle flank the cavity holes. The duty cycle of the N_{cav} holes are varied such that the reflection is weakest at the center, and increases until matching the strength of the mirror cavities, similar to other work [6, 7]. This varying of duty cycles is done to decrease both the cavity losses and V.

The Dr. Al Qubaisi-designed PhCnBs are fabricated using the GlobalFoundries 45CLO process. The samples are then flip-chipped and their Si substrates are removed. At this point, spectral sweeps reveal a $Q > 10^6$ for both anti-symmetric and symmetric cavities [1]. Once optical experiments are complete, the sample is prepared for near-filed investigation and the oxide is etched following the procedure outlined in Chapter 3 of this thesis. Predictably, due to the BOX thinning, small but measurable changes to Q, FSR and resonant wavelengths occurred.

6.3 traNSOM measurements

To help further understand the profile and confinement of the mode, traNSOM scans are conducted of the fundamental and first order resonances. Though groups have shown good agreement between theory and NSOM scans for 2D PhCs, these scans are, to the best of our knowledge, the first NSOM scans of PhCnBs which show strong agreement with simulations. The subject of our scans will be an anti-symmetric cavity with a 200 nm gap "g." For this scan, the BOX was etched to have a thickness t of 335 nm. Spectral sweeps taken just before the traNSOM scans are shown in Figure 6.3. The fundamental mode is roughly 1283.3 nm and the 1st order mode is near 1306.9 nm. As temperature
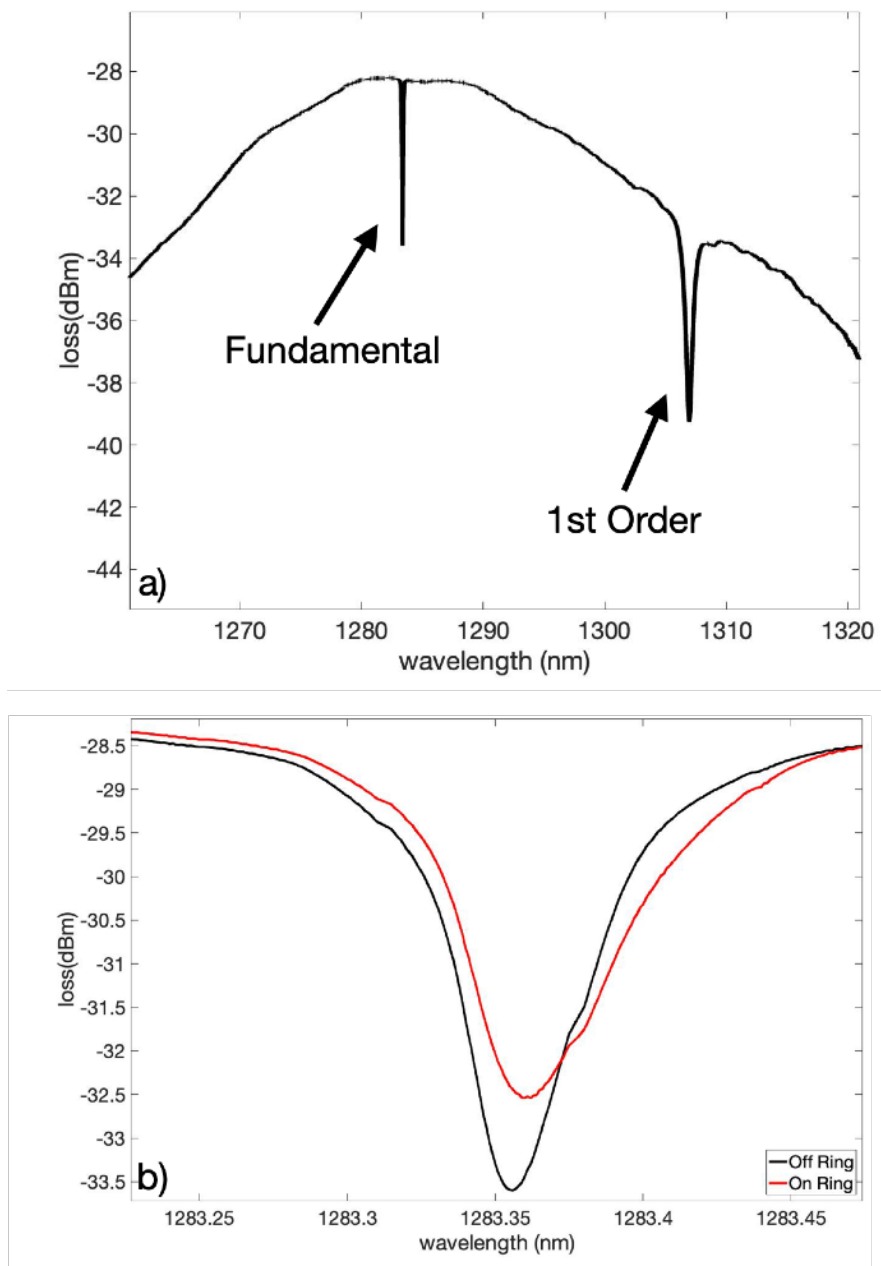
Figure 6.3 Spectral sweeps of anti-symmetric PhCnB.
(a) Spectral sweep without the traNSOM tip present. (b) Comparison of sweeps of the fundamental mode with no tip (black) and tip located at the center of the PhCnB (red).

fluctuates throughout the day, these values can shift roughly 0.1 nm, which is

why I'm not reporting values with any higher precision. We can, however,

compare sweeps taken in quick succession to a much higher precision, as is

shown in panel (b). To understand how the presence of a 50nm diameter

uncoated dielectric traNSOM probe affects the fundamental mode resonance,

spectral sweeps are conducted with the tip both on the center of the PhCnB (on)

and several microns away from the surface (off). With the tip on the surface the

PhCnB is slightly decoupled from the waveguide and the r_e decreases. With this

decrease in r_e, more light is transmitted to the output. There also appears to be a

slight decrease in Q (broadening of fwhm) as well as a potential <10 pm redshift

(although, these tip-induced changes were not studied further). With both the

redshift and the change in Q being so slight, we can be confident that, unlike the

work discussed in Section 3.3, the presence of our traNSOM tip does not

dramatically alter the mode itself (e.g. switching the device between the on-

resonant and off-resonant states during the scan). Thus, we can be confident

that any near-field scan that is conducted with this tip will be an accurate

representation of the mode profile of the PhCnB.

Figure 6.4 compares two traNSOM scans of the fundamental mode with

FDTD simulations of Ey (tangential to the waveguide) and $|\mathbf{E}|^2$. Good

agreement is shown between the mode profiles of the traNSOM signal and the

simulated $|\mathbf{E}|^2$. Two bright fringes can be seen at the center of the traNSOM

scans with decreasing intensity but constant period fringes on either side of

them. The 50 nm resolution scan in panel (c) shows that the volume occupied by
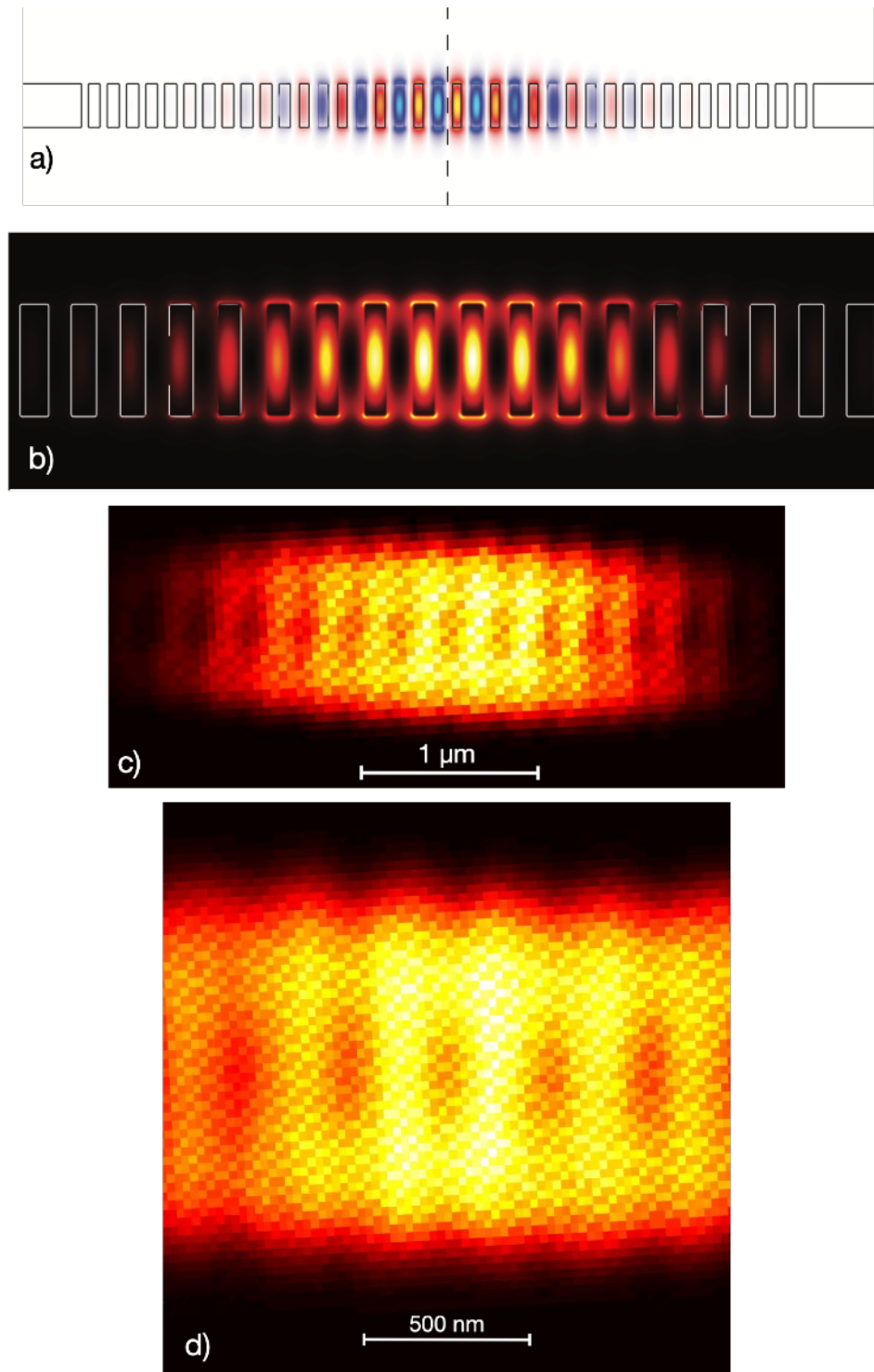
Figure 6.4 Comparison of simulated fundamental mode with experimental traNSOM scans.

(a) Simulated Ey (transverse) and (b) $|\mathbf{E}|^2$ of anti-symmetric PhCnB. (c) Measured traNSOM of entire cavity and (d) higher resolution scan with 50nm dielectric tip.
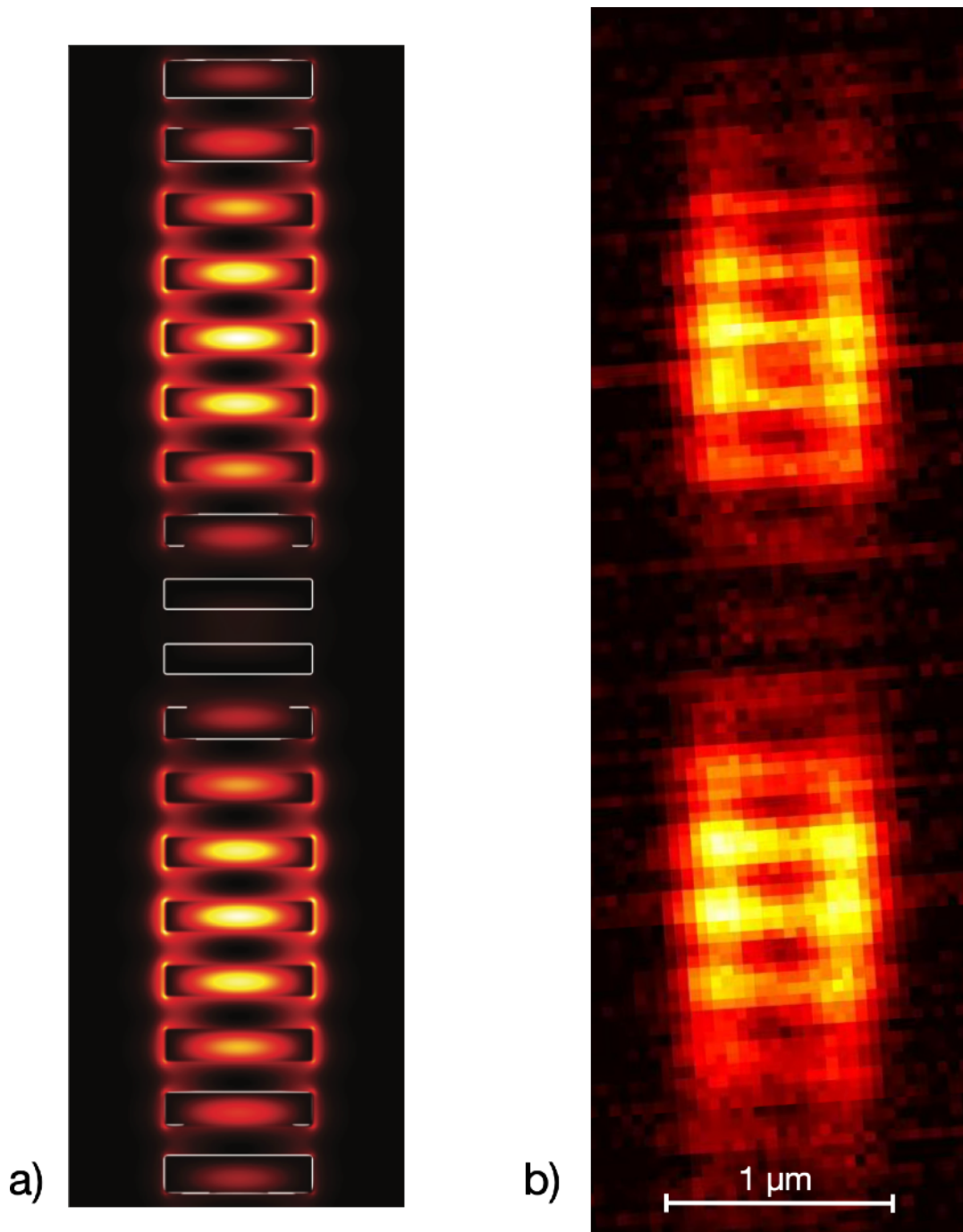
Figure 6.5 Comparison of simulated 1st order mode with experimental traNSOM scan.
(a) Simulated $|\mathbf{E}|$ of anti-symmetric PhCnB. (b) Measured traNSOM of entire cavity with 50nm dielectric tip.

the fundamental mode is nearly identical to what was simulated, and confirms that the cubic wavelength V ~ $(\lambda/n)^3$. The 25 nm resolution scan in Figure (d) further confirms the main features of the larger scan. Looking closely at this scan, however, we can see a distinction between it and the simulated $|\mathbf{E}|^2$. Minima above the PhCnB do not go to zero. This issue was already addressed when comparing simulated norm E to simulated $\Delta\lambda''$ back in Section 2.13. In that Section we came to the same conclusion that we will come to now. This discrepancy is caused by the finite size of the probe, which "smears" the field and reduces the resolution of the scan. This means that the probe still interacts with strong local fields, even when the center is directly above a location with zero field intensity. With a smaller probe diameter, we should see the signal approach the unperturbed value.

A traNSOM scan was also conducted on the first order mode as seen in Figure 6.5. Once again, there is very good agreement with the FDTD simulated $|\mathbf{E}|^2$. No field is seen at the center of the cavity, but two maxima with periodic oscillations are clearly seen on either side, in exactly the locations that we would expect.

Although there is a second order mode present, due to the oxide thickness, it could not be detected using this t and probe. In other instances, when the oxide was thinner, we could clearly see the 2nd (and sometimes 3rd) order modes. However, with these chips the tip-sample interaction was too large to properly image the fundamental mode.

6.4 Conclusion

In this Chapter, we demonstrated first of their kind traNSOM measurements of an anti-symmetric PhCnB. Both the fundamental and first order modes were scanned. The scans showed strong agreement with the simulated $|\mathbf{E}|^2$ and confirmed that these cavities confine a large amount of energy to a small, cubic wavelength V. These scans can serve as a proof of concept to other researchers that a quick and relatively simple technique can be used to map the near-field of high Q PhCs in a monolithic CMOS platform.

[1] K. Al Qubaisi, M. Schiller, B. Zhang, D. Onural, A. Khilo, M.J. Naughton and M.A. Popović "Cubic-wavelength mode volume photonic crystal nanobeam cavities in a monolithic CMOS platform," *Opt. Lett.* **48**(4) 1024-1027 (2023) doi: 10.1364/OL.481483

[2] K. Al Qubaisi, "TOWARD AN ACTIVE CMOS ELECTRONICS-PHOTONICS PLATFORM BASED ON SUBWAVELENGTH STRUCTURED DEVICES," (Doctoral dissertation, Boston University, 2023) Permanent Link: https://hdl.handle.net/2144/46257

[3] P. Dong, R. Shafiiha, S. Liao, H. Liang, N.N. Feng, D. Feng, G. Li, X. Zheng, A.V. Kirshnamoorthy, and M. Asghari, "Wavelength-tunable silicon microring modulator," *Opt. Exp.* **18**(11) 10941-10946 (2010) doi: 10.1364/OE.18.010941

[4] A.V. Krishnamoorthy, R. Ho, X. Zheng, H. Schwetman, J. Lexau, P. Koka, G. Li, I. Shubin, and J.E. Cunningham, "Computer Systems Based on Silicon Photonic Interconnects," *Proceedings of the IEEE* **97**(7) 1337-1361 (2009) doi: 10.1109/JPROC.2009.2020712

[5] K. Al Qubaisi and M.A. Popovič, "Reflectionless dual standing-wave microcavity resonator units for photonic integrated circuits," *Opt. Exp.* **28**(24) 35986-35995 (2020) doi: 10.1364/OE.403486

[6] Q. Quan and M. Loncar, "Deterministic design of wavelength scale, ultra-high Q photonic crystal nanobeam cavities," *Opt. Exp.* **19**(19) 18529-18542 (2011) doi: 10.1364/OE.19.018529

[7] B.H Ahn, J.H. Kang, M.K. Kim, J.H. Song, B. Min, K.S. Kim, and Y.H. Lee, "One-dimensional parabolic-beam photonic crystal laser," *Opt. Exp.* **18**(6) 5654-5660 (2010) doi: 10.1364/OE.18.005654

Chapter VII

Light transmission through wavelength-sized cylindrical waveguides

7.1 Introduction

In this Chapter, we will discuss theoretical and experimental optical transmission (T) through wavelength-sized cylindrical waveguides made of Cr and Au. Novel, metal-dependent, transmission characteristics are observed, as the wavelength becomes larger than the diameter of the waveguides. The behavior of the Cr waveguides follows with classical aperture theory, whereas their Au counterparts exhibit addition spectral features resulting from photonic wave interference. This work was initiated by former Naughton Lab graduate student Dr. Jeff Naughton, with fabrication and experiments of the Cr and Au structures. His work is covered in depth in his doctoral thesis [1]. In the last year, these experiments were re-visited and data re-analyzed. Through this re-evaluation, we find the results are in strong agreement with the work of García de Abajo, who studied T through opaque PEC films with near and sub-wavelength circular apertures [2]. The re-visited work was submitted for publication in March of 2024 and is currently awaiting review [3].

Describing the properties of light transmission through a hole in an opaque film has fascinated physicists for the past 4 centuries. In 1665, Grimaldi revolutionized the field of optics when he used the theory of diffraction to describe the conical shape that sunlight formed after passing through a circular aperture [4]. From the 1700s to the early 1800s, the prevailing wisdom was that

light behaves as a purely classical wave [5]. Bethe expanded on this classical

theory in 1944 by solving Maxwell's equations for an aperture of radius *a* in a

PEC with added fictitious magnetic moments and charge to satisfy the boundary

conditions within the aperture. From this, as mentioned in Chapter I, he

calculated that the light transmitted through a deeply sub-wavelength aperture

should go as:

$$T \propto \left(\frac{a}{\lambda}\right)^4. \tag{7.1}$$

Thus, *T* should vanish rapidly as the wavelength is increased beyond the size of

the aperture. In 1998 Ebeson, *et al.* turned this classical view of light

transmission on its head, by demonstrating that incident light can be converted

into surface plasmons that propagate through the aperture, and re-emit on the

other side [6]. As a result, he produced *T*s far beyond what was classically

expected. He referred to this increase in *T* as extraordinary optical transmission

(EOT). Plasmonic-based EOT can exist in non plasmonic materials as well [7]

and is enabled by a process which "spoofs" the plasmatic characteristics of real

metals [8].

In the past few decades, high powered computing has allowed

researches to find numerical solutions in situations where analytic solutions are

not possible. Two areas of particular interest are the near-wavelength regime, in

which approximations with $\lambda \ll a$ or $\lambda \gg a$ cannot be made, and in films with

finite thickness (rather than infinitely thin). With this in mind García de Abajo, *et*

al. numerically explored T for near and sub-wavelength PEC apertures with finite

thickness (t ~ 0.1a) and found a surprising EOT peak when $\frac{a}{\lambda} \sim 0.5$ [2, 9] as

shown later in this Chapter, with the dashed curve in Figure 7.4. This peak

results from oscillations in T vs. $\frac{a}{\lambda}$ and can be understood by looking at the work

of Astilean, *et al.* [10] who reported that incident light will couple to certain

modes of circular apertures in films of finite thickness. Although many modes

are excited, only one will dominate propagation along its length. As is the case

with many resonant devices, when the wavelength times the effective index (n_{eff})

(which increases as a decreases) is an integer multiple of t, constructive

interference will allow light to transmit through the cavity and scatter on the

other end, resulting in a transmittance maximum. However, if this condition is

not met, the waveguide becomes inefficient and T is suppressed. As a

increases, T oscillates with decaying amplitude around the scaled transmittance

of 1. Importantly, this example of EOT is purely photonic, rather than plasmonic.

In this Chapter, we will report on T through real metal structures similar in

size and shape the PEC structures studied by García de Abajo [2].

7.2 Materials and methods

The fabrication and experimental data collection were preformed by Dr.

Jeff Naughton. A cartoon of the device fabrication is depicted in Figure 7.1. The

waveguide structures are first etched onto Si substrates to create a master

stamp from which all subsequent samples will be replicated. The master stamp

contains 18 arrays of 1μm tall pillars. Waveguide diameters within in each of
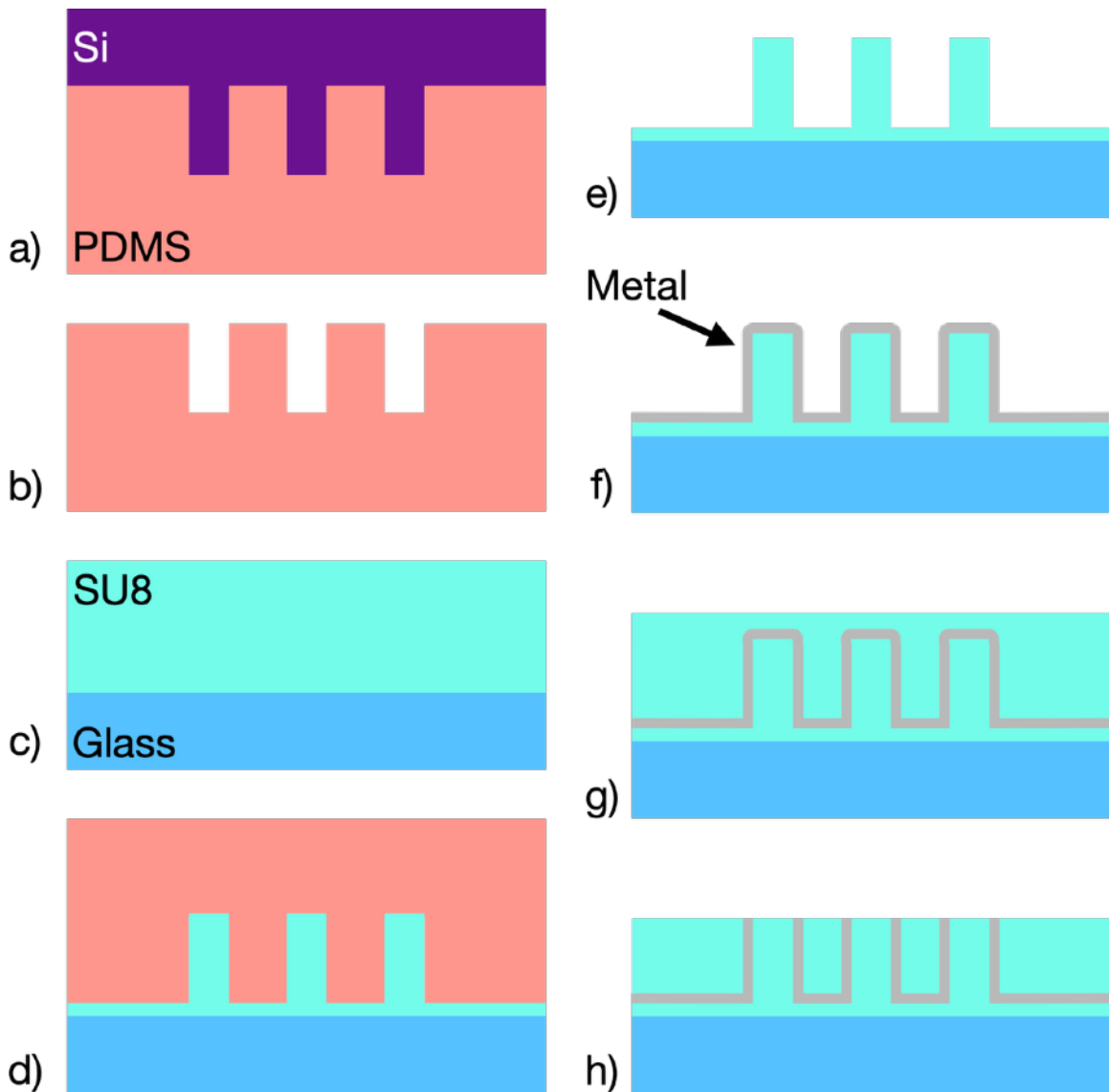
Figure 7.1 Cartoon of NIL process for waveguide aperture fabrication.
(a) Si mold is used to create PDMS negative of desired waveguide structure. (b) Borosilicate glass substrate is prepared with layer of SU8. (c) PDMS mold is pressed into SU8 layer. (d) Removal of SU8 negative followed by UV curing forms the waveguide core. (f) Metal is deposited and the sample is now optically opaque. The waveguides are "decapitated" by (g) first coating the sample in SU8 (h) then mechanical polishing which removes the top metal on the waveguide. Now entire sample is optically opaque, aside from the thin waveguide channels.

these 18 regions are constant and range from 0.17 μm in the smallest region to 3 μm in the largest. This master Si sample is used to create a polydimethylsiloxane (PDMS) mold of anti-pillars. To transfer this pattern onto the 0.5 mm thick borosilicate glass substrates (which will serve as the samples for our experiments), the PDMS molds are stamped into a thin layer of SU8, which is then UV cured to form pillars, in a process known as nano-imprint lithography (NIL). 220 nm of either Au or Cr is then sputter-deposited (after a 5 nm Ti adhesion layer) to coat the pillar samples and glass substrate. The 220 nm thickness assures that the films are opaque at visible wavelengths. A final "decapitation" step is completed to allow optical transmission through the waveguides. The sample is coated in SU8 and a mechanical polisher removes the SU8 along with the metallic 'cap' that covers the waveguide.

The resulting samples and structures can be seen in Figure 7.2. FIB milling across one of the waveguides followed by SEM imaging (depicted in panel a) reveals the structure of the completed device. In this case, the waveguide is 1 μm tall and roughly 3 μm in diameter. The overall layout of one sample can be seen in panel b. Arrays of these cylindrical waveguides allow light to pass through from the bottom and be collected on top.

With fabrication complete, experiments can now begin. The bottom side of the sample is illuminated with a Leica DM6000 optical microscope [11], which focuses unpolarized light from a 100 W halogen source onto the sample. Critically, the spot size produced by the focused light has a 180 μm diameter, which is smaller than the area of one of the cylindrical arrays. On the top side of
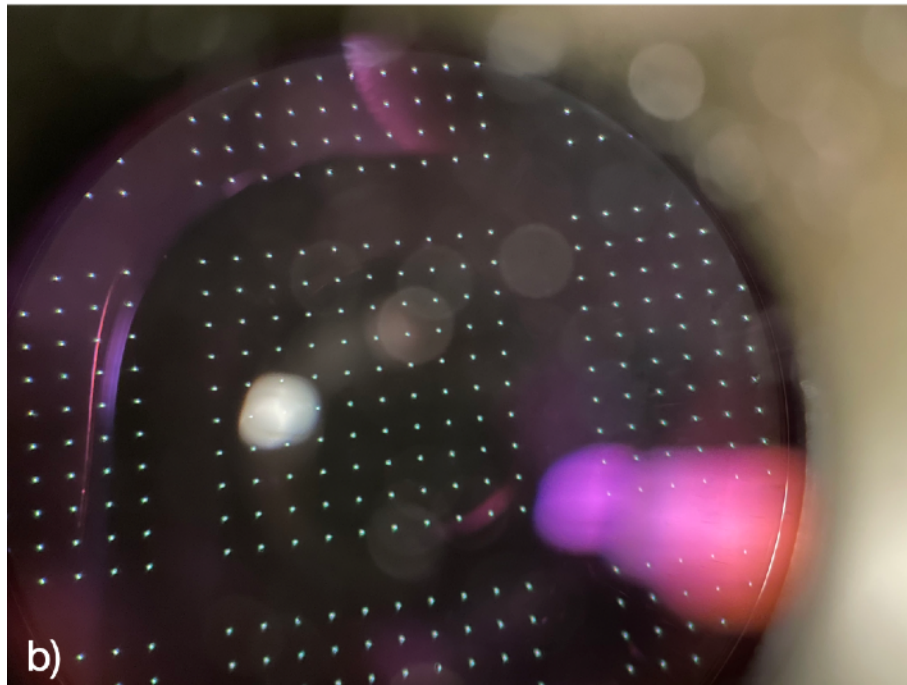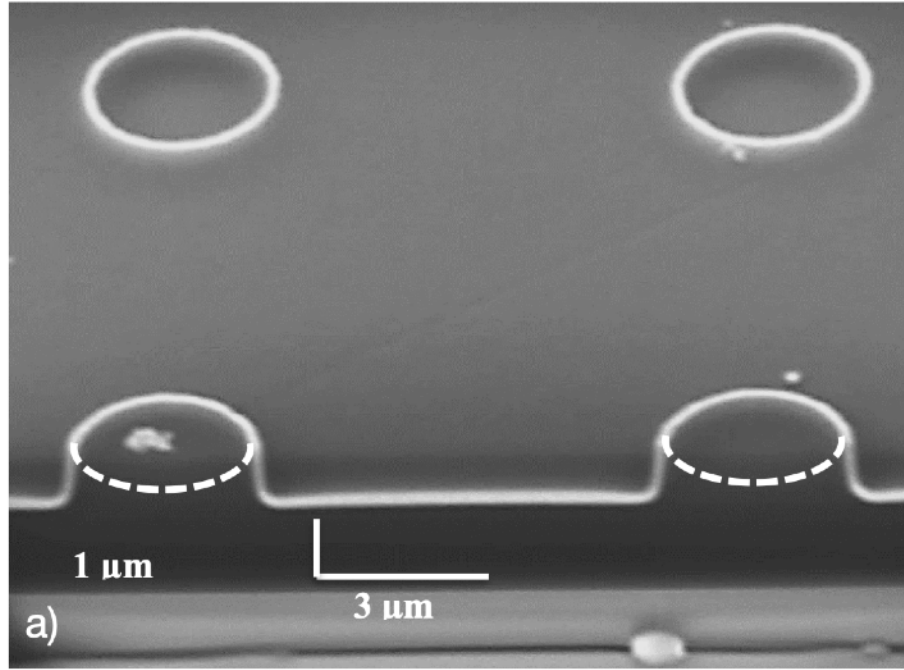
Figure 7.2 Images of completed cylindrical waveguide structure.
(a) FIB milling enabled cross sectional SEM of microwaveguides. (b) Optical image of cylindrical waveguide arrays on glass substrate.

the sample, light is collected with a 50x objective and coupled to an optical fiber

which is connected to an Ocean Optics Maya2000 Pro spectrometer [12]. In an

attempt to suppress Fabry-Perot type reflections between the sample and the

stage, the chips are placed on black tape rather than the stage itself. A solely

glass and SU8 sample is used as the reference I_{ref} and a an opaque region of

the sample is used to collect dark counts I_{dark}. T is calculated as shown below:

$$T(\lambda) = \frac{I_s(\lambda) - I_{dark}(\lambda)}{I_{ref}(\lambda) - I_{dark}(\lambda)} \tag{7.1}$$

Where I_S is the measured of the sample. In the final post processing step, the

data is divided by the square of the radius to yield T_{rel} which scales T based on

aperture area relative to the other samples. Since T_{rel} is calculated differently

from T, the two should not be conflated.

7.3 Results

Spectroscopic results are plotted in Figure 7.3. In panel (a), $T_{rel}(\lambda)$ is

plotted for Cr cylinders. The behavior roughly follows what classical aperture

theory would predict. When looking at a constant waveguide radius, T_{rel}

decreases as wavelength increases. When comparing T_{rel} for different radii, we

see that for a fixed λ, a larger aperture has a greater T_{rel} comped to a smaller

aperture. As the radii become deeply subwavelength, T_{rel} approaches zero.

However, the behavior for the Au sample is quite different. For nearly all radii,
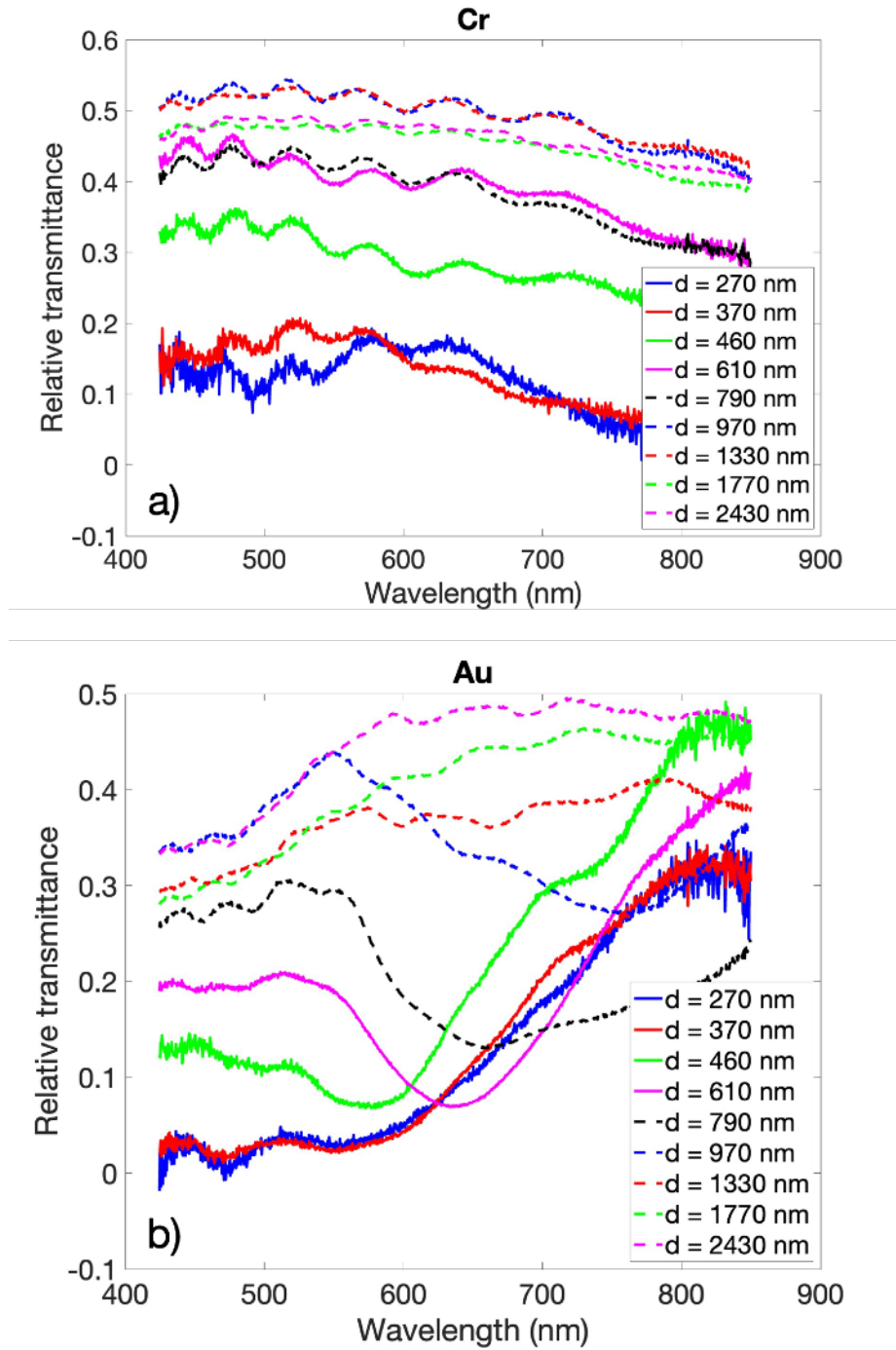
Figure 7.3 T_{rel} vs wavelength for cylindrical waveguides with diameters from 270 nm to 2430 nm.
(a) Cr and (b) Au samples.
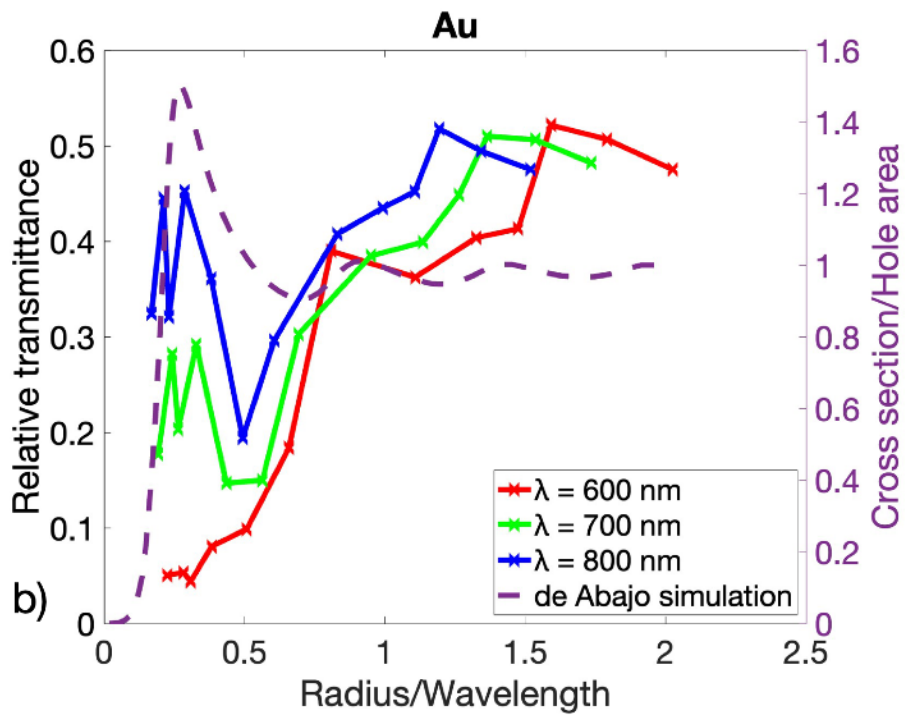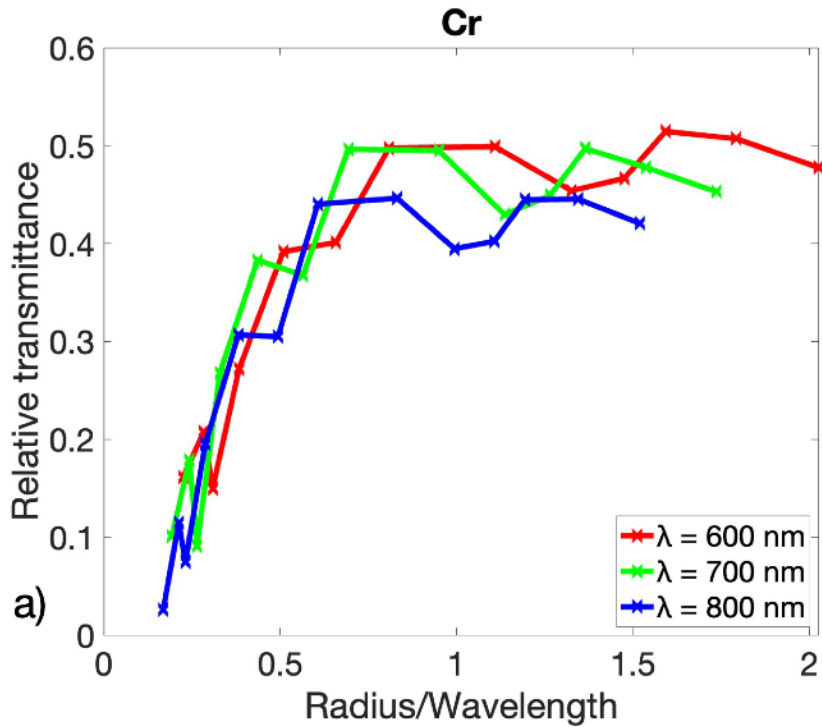
Figure 7.4 T_{rel} vs radius/wavelength for cylindrical waveguides with diameters from 270 nm to 2430 nm.
(a) Cr and (b) Au sample with data from García de Abajo ref [2] depicted with a dashed line.

T_{rel} *increases* as wavelength increases. Exactly opposite of what is expected by classical aperture theory. This effect becomes particularly pronounced as the radii of the apertures decrease.

To understand this further, lets look at Figure 7.4, which is simply a re-plotting of the data from Figure 7.3 with T_{rel} at a constant wavelength plotted vs. a/λ. We can see in panel a that T_{rel} for the Cr sample once again follows a predictable trajectory with almost no variation between the fixed wavelength curves. T_{rel} trends to zero as $a/\lambda \rightarrow 0$ and T_{rel} appears to level off to a constant value once $a/\lambda \geq 1$. However, we see dramatically different behavior for the Au sample in panel (b). We can also see strong agreement between Garía de Abajo's simulations from Ref. [2], which are plotted with the dashed line and our experimental data. When a/λ dips below 0.5, transmittance begins to increase and a peak is seen near $a/\lambda = 0.3$. This implies that the dramatic increase in transmission for subwavelength apertures in the Au sample is due to photonic resonances within the cylindrical structure, as Astilean and García de Abajo previously reported.

In addition to the peak near 0.3, there is a very pronounced dip at around 0.5. Astilean, e*t al*. explain the effect that causes this dip in Ref. [10]. Plasmonic resonances within subwavelength cavities made of real metal films generate significantly more losses than their PEC counterparts. So, with off resonant destructive photonic interference and plasmonic resonances dominating at these wavelengths, T_{rel} is suppressed. We see this effect in the Au sample and
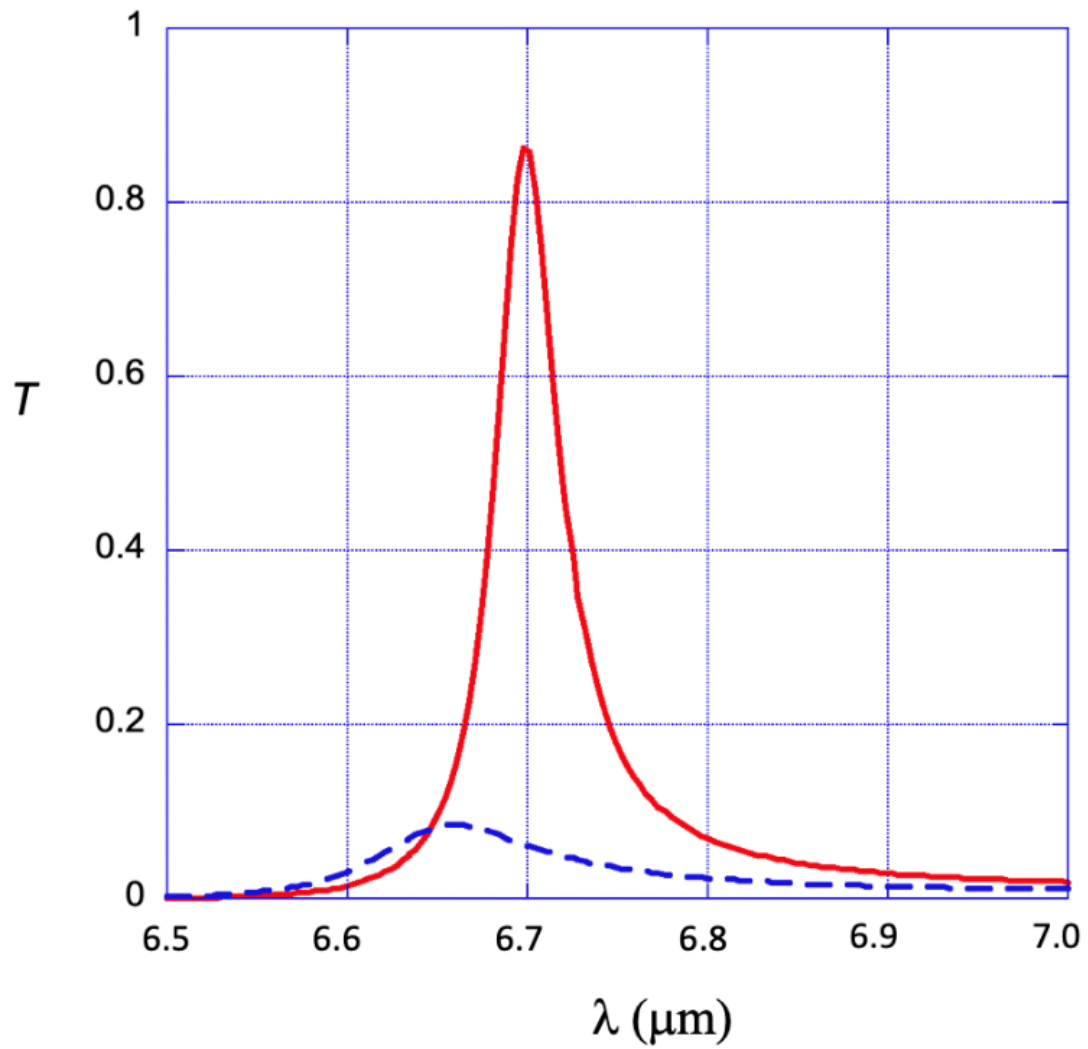
Figure 7.5 CST simulations of T vs wavelength for 2µm apertures in Au and Cr films.
Au plotted in red and Cr in dashed blue.

not the Cr sample, because the plasmon propagation length is much greater in Au than in Cr at this wavelength, so, the plasmonic resonance will be much stronger [13].

To understand the lack of peak in the Cr sample, we employ CST electromagnetic simulations of a 2 µm diameter hole in both a Cr and Au films (Figure 7.5). Both films feature a peak in T near 6.7 µm, which is very close to the $a/\lambda = 0.3$ peak seen in both the experimental and García de Abajo, *et al.* data. However, the Cr peak is greatly diminished compared to the Au peak. This dramatically reduced T is consistent with Cr being a lossy metal and having a smaller electrical conductivity when compared to Au. Additional propagation losses due to the lossy nature of Cr will further suppress this transmission maximum.

7.4 Conclusion

Optical transmission through wavelength-sized, cylindrical waveguide structures made from Au and Cr was studied both experimentally and numerically with particular interest in the near to subwavelength regime. T_{rel} for the Au sample featured novel transmittance properties that are not predicted with classical aperture theory. In agreement with the work from Ref. [2], a strong resonant peak in T_{rel} occurs near $a/\lambda = 0.3$. This peak is a result of photonic wave interference occurring within the waveguide. In addition to this peak, a plasmonic resonance-based minimum in T_{rel} is seen at $a/\lambda = 0.5$. The lossy

nature of Cr surpasses these effects in the other sample bringing T_{rel} in line with

what would be expected based on classical aperture theory.

[1] J.R. Naughton, "Neuroelectronic and Nanophotonic Devices Based on Nanocoaxial Arrays," (Doctoral dissertation, Boston College, 2017) Permanent Link: http://hdl.handle.net/2345/bc-ir:108037

[2] F.J. García de Abajo, "Light transmission through a single cylindrical hole in a metallic film," Optics Express **10**, 1475-1484 (2002). doi: 10.1364/OE.10.001475

[3] J.R. Naughton*, M. Schiller*, J.M. Merlo, A.H. Rose, Y.M. Clam, T. Dodge, S. Shepard, K. Kempa, M.J. Burns, and M.J. Naughton, "Light transmission through wavelength-sized cylindrical waveguides," *(in submission 2024)*

[4] F.M. Grimaldi, in *Physico-mathesis de Lumine, Coloribus, et Iride, Aliisque Sequenti Pagina Indicatis* 9 (Bologna, 1665).

[5] C. Huygens, in *Traité De La Lumière* (Leiden, 1690).

[6] W. Ebbesen, H.J. Lezec, H.F. Ghaemi, T. Thio, P.A. Woff, "Extraordinary optical transmission through sub-wavelength hole arrays," Nature **391**, 667-660 (1998). doi: 10.1038/35570

[7] L. Martin-Moreno, F.J. García-Vidal, H.J. Lezec, K.M. Pellerin, T. Thio, J. B. Pendry, T.W. Ebbesen, "Theory of extraordinary optical transmission through subwavelength hole arrays," Phys. Rev. Lett. **86**, 1114-1117 (2001). doi: 10.1103/PhysRevLett.86.1114

[8] J.B. Pendry, L. Martin-Moreno, F.J. Garcia-Vidal, "Mimicking surface plasmons with structured surfaces," Science **305**, 847-848 (2004). doi: 10.1126/science.1098999

[9] F.J. García de Abajo, R. Gómez-Medina, J.J. Sáenz, "Full transmission through perfect-conductor subwavelength hole arrays," Phys. Rev. E **72**, 016608 (2005). doi: 10.1103/PhysRevE.72.016608

[10] S. Astilean, P. Lalanne, M. Palamaru, "Light transmission through metallic channels much smaller than the wavelength," Optics Comm. **175**, 265–273 (2000). doi: 10.1016/S0030-4018(00)00462-4

[11] https://www.leica-microsystems.com/products/light-microscopes/p/leica-dm6000-m/

[12] https://www.oceaninsight.com/globalassets/catalog-blocks-and-images/pdfs/maya2000pro_product-sheet.pdf

[13] P.B. Johnson, R.W. Christy, "Optical constants of the noble metals," Phys. Rev. B **6**, 4370-4379 (1972). doi: 10.1103/PhysRevB.6.4370

Chapter VIII

Conclusion

8.1 Concluding thoughts

The first six Chapters of this thesis were dedicated to exploring near-field imaging of photonic integrated circuit (PIC) elements. In these Chapters, we sought to evaluate and improve not only the scans of PIC devices, but also the theory of how a probe perturbs the near-field of a device and generates an NSOM map. In Chapter II, we looked at the theory of quasi-normal mode (QNM) resonances for leaky electromagnetic resonators. We applied this theory with simulations that utilized the **MAN** software in conjunction with COMSOL. By implementing an eigenmode solver alongside weak form PDEs, we were able to properly simulate the perturbation caused by an Au NSOM probe as it scans over a high Q ring resonator. We found that the tip induces a loss that is proportional to the strength of the local electric field, but there is no systematic modification to the resonant wavelength of the cavity. Although this result went directly against previously-reported experiments on electromagnetic resonators, which were approximated to be lossless, it demonstrated strong agreement with our own experiments. Assuming the system to be lossy proved to be critical in understanding the interaction between a NSOM probe and a PIC device.

In Chapter III, we sought to implement our findings from Chapter II with real NSOM scans of PICs that avoid certain pitfalls that had plagued previously reported work. After describing the experimental set-up and post processing steps that allowed us to access the near-field, we explored how the presence of

an apertured probe during a cNSOM scans affects the performance of a PIC waveguide and resonator. traNSOM maps revealed that there was a small tip induced loss when cNSOM scanning the waveguide. However, when scanning a PhCnB, the tip-induced losses became not only large, but detrimental to the cNSOM scan and device performance. Clearly, an apertured NSOM probe causes too much of a disturbance when scanning the PhCnB. The effect of an apertureless probe on a microring resonator was then studied. We showed that the presence of a 50 nm diameter Au-coated tip induces a loss but does not shift the resonance, exactly as predicted by the simulations from the previous Chapter. We thus concluded that apertureless traNSOM scans can be conducted on PIC devices without fear of dramatically altering their performance or near-fields.

For Chapter IV, we demonstrated the power of super-resolution cNSOM imaging of non-resonant PIC elements. A polarization-insensitive GC based on a zero birefringence "corelet" waveguide was cNSOM-scanned at several heights using a 150 nm-diameter aperture probe. Scans for both transverse electric (TE) and transverse magnetic (TM) polarizations demonstrated that the profile and angle of the beam was relatively similar for both. This result confirmed that, as desired, the "corelet" waveguide decreased the birefringence and therefore polarization sensitivity of the GC.

While the apertured probe worked so well for the GC application, in Chapter V we found that, when scanning a spoked microring resonator, the quality of a cNSOM is very low. This is because, the oxide thickness required to

reduce the tip-sample interaction meant that the 150 nm aperture probe collected very little light. Increasing the scan quality and resolution would require further oxide thinning, which would be detrimental to resonator performance. In order to properly image the near-field, an apertureless 50 nm diameter Au-coated tip was used to generate a traNOSM scan. Since a smaller probe was used, the BOX could be further thinned without fear of affecting device performance during the scan. With these adjustments, a high resolution traNSOM scan of the microring near-field was produced. This scan had ~ 50 nm resolution, which was high enough for the wavelength of the light within the ring to be measured.

In an effort to demonstrate the power of this technique on not only microring resonators, but also other highly Q photonic devices, in Chapter VI the fundamental and first order modes of a PhCnB were measured. Using an apertureless 50 nm dielectric probe, the fundamental and first order modes were measured. The resulting traNSOM data matched very well with the simulated $|\mathbf{E}|^2$ for both of these modes. This scan was the first of its kind to show strong correlation between the measured and simulated near-fields of a high Q, low V PhCnB. These scans further proved that the mode is indeed contained within the small V of the cavity.

The procedures outlined in Chapters III-VI, provide a roadmap for generating high resolution near- and far-field images of any arbitrary PIC device on a monolithic integrated electronics-photonics chip. Moreover, the theoretical and numerical methods in Chapter II demonstrate proper accounting for the

perturbation generated by a near-field scan on a resonant device. With the field of PIC growing at an ever accelerating rate, these scans and simulations could prove vital as they provide relatively rapid, inexpensive, and nondestructive verification of the performance of any PIC device on a CMOS chip.

In Chapter VII ,we departed from the field of PICs and instead, looked at small cylindrical waveguide apertures in metallic films that generate novel transmittance properties. Devices made of both Au and Cr were simulated and studied experimentally. We found that subwavelength apertures in Au sample exhibited enhanced *T* at $a/\lambda \sim 0.3$ due to photonic wave interference and *T* suppression near $a/\lambda \sim 0.5$ due to plasmonic resonances within the waveguide. Both of these features were absent from the Cr sample, whose *T* followed much more closely to classical aperture theory, due to the lossy nature and reduced plasmon propagation length of Cr.

8.2 Suggested further experiments

The NSOM-on-PIC procedures outlined in the first six Chapters of this thesis are primed to characterize other circuit elements and measure new devices. New GC designs can easily be measured with the cNSOM technique from Chapter III. Of particular interest would be GCs designed to manipulate single atoms for quantum computing. Other circuit elements beyond resonators, such as multiplexers or demultiplexers, are waiting to have their near-fields verified. These NSOM procedures could also perform vital debugging of devices that are not preforming properly, so that researchers can quickly diagnose performance issues and modify designs accordingly.

Aside from these applications, the system can be modified to accommodate active, rather than only passive devices. If the chip is bonded to a PCB rather than a glass slide during the flip chip procedure, the electronic devices can be controlled. Doing this relatively straightforward step would allow researchers to investigate PICs in real time to observe dynamic PIC phenomena in a non-destructive manner.

Another interesting avenue that should be explored, would involve writing new NSOM software that conducts a frequency sweep for each tip location during the scan. At each of these locations, $\Delta\lambda'_m$ and ΔQ_m could be computed and then used to map the optical local density of states (optical LDOS). Setting the system up for optical LDOS measurements would provide hugely valuable quantitative information about PIC device performance. While there is already a body of research on optical LDOS with NSOM [1, 2], the work required to re-write our NSOM software to work in conjunction with a laser, or the expense to buy a new tool, would inevitably be quite large.

[1] C. Chicanne, T. David, R. Quidant, J. C. Weeber, Y. Lacroute, E. Bourillot, and A. Dereux, "Imaging the Local Density of States of Optical Corrals," *Phys. Rev. Lett.* **88** (9), 097402-1 (2002) doi: 10.1103/PhysRevLett.88.097402

[2] D. Pellegrino, D. Balestri, N. Granchi, M. Ciardi, F. Intonti, F. Paglian, A.Y. Silov, F.W. Otten, T. Wu, K. Vynck, P. Lalanne, A. Fiore, and M. Gurioli, "Non-Lorentzian Local Density of States in Coupled Photonic Crystal Cavities Probed by Near- and Far-Field Emission," *Phys. Rev. Lett.* **124**, 123902 (2020) doi: 10.1103/PhysRevLett.124.123902